Optimization of flexible wings and vorticity transfer in a leading-edge vortex due to spanwise bending

by

Kun Jia

B.S., University of Science and Technology of China, China, 2012

M.S., University of Science and Technology of China, China, 2015

AN ABSTRACT OF A DISSERTATION

submitted in partial fulfillment of the
requirements for the degree

DOCTOR OF PHILOSOPHY

Alan Levin Department of Mechanical and Nuclear Engineering
Carl R. Ice College of Engineering

KANSAS STATE UNIVERSITY
Manhattan, Kansas

2021

Abstract

Flexible flapping-wing flight has been widely utilized in nature and applied in micro-air vehicles (MAVs) and biomimetic air vehicles (BAVs) due to its excellent aerodynamic forces generation, energy efficiency, and maneuverability. Especially, active-controlled morphing provides air vehicles more advantages in complex flight scenarios or missions. However, a comprehensive understanding of the active-controlled flexibility, which can be implemented by muscle or mechanical structures, still lacks.

Different types of deformation, such as spanwise bending and linear twisting, contribute differently to its thrust and power efficiency for a flexible wing in flapping motion. However, the study of the impact of the deformation on aerodynamic performance is very challenging when many control parameters are involved. Due to the time-varying feature of all these control parameters, it is impractical and unnecessary to conduct a complete parametric study to achieve the global optimization of flexible wings for specific objectives. The adjoint-based method, whose computational cost is independent of the size of control parameters, has a natural advantage in solving the problem with a large control parameter space. The adjoint-based approach with the implementation of non-cylindrical calculus for moving boundary problems, which was developed and validated in our earlier study for optimizing the rigid flapping wing, is utilized here to optimize the control of active morphing.

For the wing flapping with an optimized pitching-rolling motion, introducing and optimizing the spanwise bending can double the thrust power at the price of a slight reduction of efficiency. The concept of effective rolling angle, which is defined by the instantaneous position of the wingtip, reveals that the spanwise bending can enhance the amplitude of wingtip motion to improve the thrust. The effects of wing shape on the thrust are also investigated. On the other hand, the optimization of twisting can help the flexible wings maintain a large thrust with a much lower total energy consumption. The investigation of

the effective angle of attack shows that the delayed twisting can modify the pressure distribution on wing surfaces to help the flexible wing generate propulsion with less energy consumption. The related adjoint-based optimization provides us a unique opportunity to understand the flexibility mechanism with active deformation and optimal guidance to the industrial design.

At last, the effects of active bending on the formation of the leading-edge vortex (LEV) of a flat plate are studied via numerical simulation. The flat plate accelerates from rest to achieve $Re = 2400$ with a constant angle of attack of $30°$. The circulation growth computed from numerical simulation matches well with the growth from the analytical model and experiments. Our simulation results showed that the bending could modify the vorticity convection flux along the plate's bent part to reduce the shear layer velocity, which will finally delay the LEV growth.

Optimization of flexible wings and vorticity transfer in a leading-edge vortex due to spanwise bending

by

Kun Jia

B.S., University of Science and Technology of China, China, 2012

M.S., University of Science and Technology of China, China, 2015

A DISSERTATION

submitted in partial fulfillment of the
requirements for the degree

DOCTOR OF PHILOSOPHY

Alan Levin Department of Mechanical and Nuclear Engineering
Carl R. Ice College of Engineering

KANSAS STATE UNIVERSITY
Manhattan, Kansas

2021

Approved by:

Major Professor
Mingjun Wei

Copyright

Abstract

Flexible flapping-wing flight has been widely utilized in nature and applied in micro-air vehicles (MAVs) and biomimetic air vehicles (BAVs) due to its excellent aerodynamic forces generation, energy efficiency, and maneuverability. Especially, active-controlled morphing provides air vehicles more advantages in complex flight scenarios or missions. However, a comprehensive understanding of the active-controlled flexibility, which can be implemented by muscle or mechanical structures, still lacks.

Different types of deformation, such as spanwise bending and linear twisting, contribute differently to its thrust and power efficiency for a flexible wing in flapping motion. However, the study of the impact of the deformation on aerodynamic performance is very challenging when many control parameters are involved. Due to the time-varying feature of all these control parameters, it is impractical and unnecessary to conduct a complete parametric study to achieve the global optimization of flexible wings for specific objectives. The adjoint-based method, whose computational cost is independent of the size of control parameters, has a natural advantage in solving the problem with a large control parameter space. The adjoint-based approach with the implementation of non-cylindrical calculus for moving boundary problems, which was developed and validated in our earlier study for optimizing the rigid flapping wing, is utilized here to optimize the control of active morphing.

For the wing flapping with an optimized pitching-rolling motion, introducing and optimizing the spanwise bending can double the thrust power at the price of a slight reduction of efficiency. The concept of effective rolling angle, which is defined by the instantaneous position of the wingtip, reveals that the spanwise bending can enhance the amplitude of wingtip motion to improve the thrust. The effects of wing shape on the thrust are also investigated. On the other hand, the optimization of twisting can help the flexible wings maintain a large thrust with a much lower total energy consumption. The investigation of

the effective angle of attack shows that the delayed twisting can modify the pressure distribution on wing surfaces to help the flexible wing generate propulsion with less energy consumption. The related adjoint-based optimization provides us a unique opportunity to understand the flexibility mechanism with active deformation and optimal guidance to the industrial design.

At last, the effects of active bending on the formation of the leading-edge vortex (LEV) of a flat plate are studied via numerical simulation. The flat plate accelerates from rest to achieve $Re = 2400$ with a constant angle of attack of $30°$. The circulation growth computed from numerical simulation matches well with the growth from the analytical model and experiments. Our simulation results showed that the bending could modify the vorticity convection flux along the plate's bent part to reduce the shear layer velocity, which will finally delay the LEV growth.

Table of Contents

List of Figures xi

List of Tables xvi

Acknowledgements xvii

Dedication xix

1 Introduction 1

1.1 Flapping wing flight 1

1.1.1 Effects of flyers' sizes on flight characteristics 2

1.1.2 Rigid flapping wing aerodynamics 2

1.1.3 Flexible flapping wing aerodynamics 4

1.1.4 Formation and development of LEV 5

1.2 Concepts of flexible wing 7

1.2.1 Aerofoil-level morphing 7

1.2.2 Wing-level morphing 9

1.3 Optimization design 11

1.3.1 Gradient-based optimization 11

1.3.2 Gradient-free optimization 12

1.4 Present work 12

2 Numerical algorithms for simulation and optimization 15

2.1 Governing equations and cost functions 16

2.2 Immersed boundary method 18

2.3 The adjoint analysis via non-cylindrical calculus . . . 18
2.3.1 Non-cylindrical calculus . . . 19
2.3.2 Linearized perturbation equations . . . 21
2.3.3 Adjoint equations and gradient calculation . . . 22
2.4 Numerical algorithms . . . 24
2.5 Numerical configuration . . . 25
2.5.1 Kinematics setup . . . 25
2.5.2 Solid and fluid meshes . . . 27
2.5.3 Grid independence . . . 27
2.6 Optimization for thrust . . . 29
2.6.1 Effects on pressure distribution . . . 30
2.6.2 Effects on effective angle of attack . . . 31
2.6.3 Effects on wake topology . . . 32
2.7 Optimization for efficiency . . . 33
2.7.1 Effects on pressure distribution . . . 36
2.7.2 Effects on effective angle of attack . . . 36
2.7.3 Effects on wake topology . . . 36

3 Optimization of flexible wings for thrust and efficiency . . . 41
3.1 Spanwise bending modeling . . . 41
3.1.1 Euler-Bernoulli beam solutions . . . 42
3.1.2 Bending control . . . 43
3.1.3 Effective angle of attack . . . 45
3.1.4 Effective rolling angle . . . 46
3.2 Optimization for thrust . . . 47
3.2.1 Effects on effective rolling angle . . . 49
3.2.2 Effects on pressure distribution . . . 49
3.2.3 Effects on effective angle of attack . . . 52

3.2.4 Effects on wake topology . . . 53
3.2.5 Effects of wing shape on thrust . . . 55
3.3 Twisting modeling . . . 55
3.3.1 Effective angle of attack . . . 56
3.4 Optimization for efficiency . . . 58
3.4.1 Effects on pressure distribution . . . 62
3.4.2 Effects on effective angle of attack . . . 63

4 Vorticity transfer in a LEV due to controlled bending . . . 67
4.1 Vorticity transfer . . . 68
4.2 Plate model and kinematics . . . 70
4.3 Computational configuration . . . 72
4.4 Grid independence . . . 72
4.5 The growth of the LEV during bending . . . 74
4.5.1 Analytical model . . . 74
4.5.2 PIV measure . . . 77
4.5.3 Numerical simulation . . . 78
4.5.4 Comparison of LEV circulation . . . 82
4.6 Effect of bending on the convection of vorticity . . . 85
4.7 Discussion . . . 89

5 Conclusions . . . 90

Bibliography . . . 93

A The process of calculating the circulation by the analytic model . . . 103

List of Figures

1.1 Schematic of the three-dimensional flow over the top of the flapping wing at its mid-point. 6

2.1 Schematic drawing of the immersed boundary method. The fluid domain is denoted by Ω, and the boundary of solid is denoted by $\mathcal{S}$. The fluid points are represented by the interaction points of dashed lines (Eulerian points), and the boundaries are represented by the Lagrangian points. 19

2.2 Schematic of the global perspective and the two-dimensional views of the three-dimensional rigid wing[1]. 25

2.3 Definition of the angle of attack for the rigid wing[1]. 26

2.4 Schematics of a) the computational domain and Cartesian mesh employed in the current simulation and b) a typical ellipsoidal plate used in the current study. The surface of the plate is represented by unstructured meshes made of triangular elements[1]. 28

2.5 Comparison of the instantaneous thrust coefficients of the rolling-pitching wing in initial and optimal cases. 31

2.6 The pressure distribution of the Rigid_Int and Rigid_Opt cases when $t/T = 0$. 32

2.7 The pressure distribution of the Rigid_Int and Rigid_Opt cases when $t/T = 0.2$. 33

2.8 Comparison of the angles of attack of the two cases at a)50% span, and b) 70% span. 34

2.9 Comparison of the wake topology of the rolling–pitching wing with the a) initial control, b) optimal control at $t/T = 0$. 35

2.10 The comparison of the instantaneous history of a) total consumed power P_c, and b) output power P_0 of different cases. 37
2.11 The pressure distribution of three cases when $t/T = 0$. 38
2.12 Comparison of a) the angle of attack at 50% span, and b) the angle of attack at 70% span 39
2.13 Comparison of the wake topology of a) the Rigid_Opt case and b) the Rigid_Eff case at $t/T = 0$. 40

3.1 The evolution from a biological wing to a cantilevered Euler-Bernoulli beam: a) the wing of a hummingbird, b) the numerical models of the bird's wing and body in the simulation, c) the wing model is mimicked by an ellipse plate, d) the deformation of a wing can be treated as the deflection of a cantilevered beam. 42
3.2 Shapes of the first three natural modes of the cantilever beam. 44
3.3 The schematic of the flexible wing with spanwise bending[1]. 45
3.4 Effective angle of attack for the flexible wing with spanwise bending[1]. 46
3.5 Definition of effective rolling angle of the flexible wing. 47
3.6 a) The comparison of the instantaneous thrust coefficient history, b) the effects of the phase delay φ_1 on the thrust coefficient in the Flex_Opt case[1]. 50
3.7 The effective rolling angles in the Rigid_Opt case (dashed line) and in the Flex_Opt case (solid line) 51
3.8 The pressure distribution of the Flex_Int (Rigid_Opt) and Flex_Opt cases when $t/T = 0$[1]. 52
3.9 Comparison of a) the angle of attack at 50% span, and b) the angle of attack at 70% span[1]. 53
3.10 Wake topology of the plate with a) initial control and b) optimal control at $t/T = 0$. The isosurface contours are color coded by the streamwise vorticity ω_x[1]. 54

3.11 Thrust coefficient changes with different γ 56
3.12 Wing shapes with different γ when $t/T = 0.2$ 57
3.13 The pressure distribution on surfaces with different γ. 58
3.14 Schematic of the flexible wing with linear twisting[1]. 59
3.15 Effective angle of attack for the flexible wing with twisting[1]. 59
3.16 The comparison of the instantaneous history of a) total consumed power P_c, and b) output power P_0 of different cases[1]. 61
3.17 The instantaneous efficiency changes with the phase delay φ_t in the Twist_Opt case[1]. 62
3.18 The pressure distribution of the Rigid_Opt, Twist_Int and Twist_Opt cases when $t/T = 0$[1]. 63
3.19 The comparison of the instantaneous angle of attack at 70% span in Rigid_Opt, Twist_Int, and Twist_Opt cases[1]. 64
3.20 The comparison of the instantaneous angles of attack at 70% span in Rigid_Opt, Rigid_Eff, and Twist_Opt cases. 65
3.21 The schematic of the physical model about the effects of twisting on aerodynamic force projection[1]. 66

4.1 The construction of the morphing plate: a) grooves inside a 3D printed plate for holding prebent rods; b) the plate-rod assembly is connected to servos, which bend the plate along the span; c) the definition of bending angle and bending ratio. The tips are marked by AB and GH; the 50% span and the 80% span are, respectively, marked by CD and EF[2]. 70
4.2 The kinematics of the plate motion. The plate is accelerated for $t^* = 1$ and the bending is completed at $t^* = 2$. u^* is obtained by normalizing u (velocity) by U_∞ (0.05 m/s)[2]. 71

4.3 Schematics of a) the computational domain and Cartesian mesh employed in the current simulation. The mesh along the x direction is stretched and the length of the uniform part is $5.8c$; b) the dimensions of the plate used in the current study. The solid arrow stands for the moving direction of the plate, which is along the x-axis direction[2]. 73

4.4 a) The LEV on the midspan (50% span) of the plate with different grid sizes. b) The LEV on 80% span of the plate with different grid sizes. 74

4.5 The aerodynamic force histories generated by different grid sizes(black lines: Δ_2; red lines: Δ_3).a) the comparison of the lift, b) the comparison of the drag. 75

4.6 Details of the analytical model: a) The LEV is modeled as a semicylindrical blockage in Wong et al.[3], where vorticity is being supplied by a shear layer; b) the modification implemented in the analytical model in the present work, where the component of the bending velocity was subtracted from the effective velocity on the leading edge[2]. 76

4.7 Experimental setup: a 1-m-long towing tank facility equipped with Velmex traverse. The camera travels along with the plate; A skim plate is used to prevent the formation of surface waves during towing. PIV measurements were conducted at 50% and 80% span of the plate (CD and EF in Fig.4.1)[2]. 77

4.8 The development of the LEV on the midspan CD (50% span) of the plate from PIV measurements: when no bending was applied (left column) and when bending was applied (right column). The contour plots are created from normalized spanwise vorticity. The cutoffs were selected at each t^* to exclude the boundary layer[2]. 79

4.9 The development of the LEV on EF (80% span) of the plate from PIV measurements: when no bending was applied (left column) and when bending was applied (right column). The contour plots are created from normalized spanwise vorticity. When the plate was dynamically bent, the growth of the LEV at 80% span was delayed[2]. 80

4.10 The LEV development on CD (50% span) of the plate from DNS: (left column) when no bending was applied; (right column) when bending was applied[2]. . 81

4.11 The LEV development on EF (80% span) of the plate from DNS: when no bending was applied (left column) and when bending was applied (right column)[2]. 83

4.12 Comparison of the temporal growth of LEV circulation computed from the analytical model, PIV experiment, and DNS study[2]. 84

4.13 The comparison of the spanwise vorticity convection flux through the LEV cores of the flat and bending cases in a) a global view and b) a zoomed view when $t^* = 1.9$[2]. 86

4.14 The comparison of the spanwise vorticity convection flux of the flat (left) and bending (right) cases at different moments in a zoomed view from DNS[2]. . . 87

4.15 The vorticity contours and the vorticity convection flux at EF (80% span) when $t^* = 1.5$ (top) and $t^* = 1.9$ (bottom). The solid lines and dashed lines represent the LEV and the secondary vortex, respectively. The vorticity convection flux is colored[2]. 88

List of Tables

2.1 Results of grid and domain independence study with inital control. 29

2.2 The range of control variables for thrust optimization. 29

2.3 The control parameters and thrust coefficients optimization in the current study. 30

2.4 The control parameters, efficiencies, and thrust coefficients of different cases. 36

3.1 The control parameters and thrust coefficients in the intial and optimal cases. 48

3.2 The effective rolling amplitudes and thrust coefficients in different cases. . . 51

3.3 The control parameters and efficiencies in different cases. 60

4.1 Non-dimensional parameter space. 72

Acknowledgments

At the end of the dissertation, I sincerely appreciated this opportunity to express my thanks to all professors and friends who accompanied me.

First and foremost, I want to give my most thanks to my supervisor, Dr. Mingjun Wei, for all his generous support in my research and life. I benefited a lot from his practical courses, in-depth discussions, and broad knowledge. He is always enthusiastic about the new topics of science and shares his unique insights selflessly with us. He is also the most honest and intelligent person I have ever met. When I encounter differentiates of feel confused, his daily wise words and exemplary behavior help me to calm down quickly. It is my honor to follow such a patient, supportive, and knowledgeable advisor as his student.

I also want to express my appreciation to Prof. Betz, Prof. Derby, and Prof. Wu for serving as my committee members. They urged me to rethink my research and encouraged me to better understand this world based on my research. I am grateful for their beneficial comments and suggestions. My sincere thanks also to all teachers and staff of NMSU and KSU.

For my research, I would like to express my special thanks to Prof. Bhattacharya for our first collaboration. During this project, which became Chapter 4 of this dissertation, I was impressed and inspired by his unique insights, solid theoretical foundation, and proficient programming ability. Meanwhile, I would like to thank Dr. Yang and Dr. Xu for constructing the structure of numerical simulation and Adjoint-based optimization programs. My research of understanding the flexibility of wings and vorticity transfer analysis is based on their solid work. All other members of the Computation Science for Fluids and Acoustics Lab, Dr. Haotian Gao, Dr. Wei Zhang, Dr. Elnaz Rezaian, Bolun Xu, Sherif Elsayed, are also greatly appreciated.

At last, I would like to thank my family and friends. My parents raised me and offered me the best education. My sister's family also gives me their selfless supports. When I saw

the smiles of the two cute nieces, all tiredness would fly. Most of all, I want to thank my girlfriend, Meng Ding. She is always accompanying and supporting me through all the tough moments, especially in this pandemic.

Dedication

To my parents, sister,

and my girlfriend Meng

Chapter 1

Introduction

Flyers, like birds and insects, have widely utilized flexible wings to gain advantages in force generation, energy efficiency, and maneuverability to survive in nature. To better understand the roles of different deformation in flight, we introduced different types of active morphing to the rigid wing and optimized the corresponding control. The related adjoint-based optimization provides us a unique opportunity to understand the flexibility mechanism and gives optimal guidance to the industrial design. In this chapter, the development of the unsteady mechanism, the general concepts of flexibility modeling, and the features of popular optimization techniques will be reviewed in detail.

1.1 Flapping wing flight

Flyers in nature, including insects and birds, have used the flapping systems to generate thrust and lift for millions of years. Human engineers intrigued by their ability to fly have designed various air vehicles, such as micro air vehicles (MAVs), flapping-wing micro air

vehicles (FWMAVs), and bio-mimetic air vehicles (BAVs), by imitating these natural flying creatures[4]. Since the 1990s, the US Defense Advanced Research Projects Agency (DARPA) has invested a lot of energy and money to promote the research of unmanned aircraft[5]. DARPA defined that the size of the MAVs should be less than 15 cm, and the size of the nano-air vehicles (NAVs) should be less than 7.5 cm, or the weight should be less than 10 g. Unmanned vehicles are widely applied and demonstrate their advantages in many dangerous scenes, such as searching in burning buildings, sensing chemical leaks, or detecting radiation in nuclear leaks in industry[6]. However, the study of biological flight and wings remains essential for understanding the aerodynamic mechanism and designing MAVs.

1.1.1 Effects of flyers' sizes on flight characteristics

The sizes of flyers have significant effects on the characteristics of biological flapping flight, like Reynolds number Re, patterns of shape deformation, and reaction timescales. There is a general trend that when the size of a flyer decreases, the Reynolds number Re and the wing/body mass ratio will also decrease, but the flapping frequency will increase. Bats, who have a larger wing-to-body mass ratio, can control the deformation of their wings to obtain better maneuverability at the cost of larger energy consumption. Small flyers, such as insects, have a lower wing-to-body ratio and flexes their wings passively.

1.1.2 Rigid flapping wing aerodynamics

Due to the limitation of materials science, electrical equipment, and manufacturing technology, the early studies of the flapping wing aerodynamics were conducted based on the

rigid wing models. The first theoretical study about the rigid flapping-wing aerodynamic is thought to start from Birnbaum, who studied small-amplitude oscillating wings in the early 19th century[7]. The biologist Weis-Fogh[8] studied the lift and efficiency of the hovering flight of insects to explain how insects fly. He concluded that steady-state aerodynamics accounts for the hovering flight of insects. The clap-and-fling motion, observed in many insects, can reduce the power requirement and improve the lift generation[9]. The phase difference between the translation and the rotation also has significant effects on the aerodynamic force generation. Dickinson et al.[10] noticed that the lift could be enhanced by the advanced rotation or be reduced by the delayed rotation.

The leading-edge vortex (LEV) plays a critical role in the flapping-wing aerodynamics at low Reynolds numbers[11]. Ellington et al.[12] studied the effects of unsteady mechanisms on force generation and observed that the delayed stall LEV could significantly enhance the lift of wings. Birch and Dickinson[13] concluded that the wake capture could improve the force peak by increasing the effective flow velocity. But they also realized that the effects of wake capture highly depend on the wing kinematics and flow structures.

Ellington[14] proposed and developed the quasi-steady models, which took the delayed stall and other unsteady mechanisms into consideration, to predict the instantaneous aerodynamic forces of the pitching and plunging wings. Wang[15] implemented numerical studies with the quasi-steady models to explore the unsteady flapping mechanism. The blade-element models are also developed to handle the effects of mass effects, vortex generation, delayed stall, and circulation effects[11;16–18]. Besides these, the surrogate models have received more and more attention due to their advantages in computation efficiency and explaining the effects of flexibility on the generation of aerodynamic forces[19].

1.1.3 Flexible flapping wing aerodynamics

In nature, flyers often flex their wings actively or passively to modify the wing shape or area to improve their aerodynamic performance[20]. Insects' wings are made up of membrane-vein structures, whose thickness and stiffness vary over span and chord. Wootton[21] first realized that because there is no intrinsic musculature in insects' wings, the shape deformation is implemented by the interactions between the structure, the aerodynamic, and inertial forces. Combes and Daniel[22],[23] studied the structural flexibility of insects' wings through experiments. They validated that for most insect species, the stiffness along span is larger than the stiffness along the chord. Heathcote et al.[24] studied the effects of passive flexibility of a heaving plate on the thrust production and found that when Strouhal number (St) is between 0.2 and 0.4, the spanwise deformation can improve the thrust.

Young et al.[25] conducted three-dimensional simulations of modeled locusts and compared the numerical results with smoke visualizations and particle image velocimetry (PIV) on real locusts. They found that flexibility prolongs the attachment of LEV on the wing surface during the flapping cycle, which benefits the power economy for lift generation. Du and Sun[26] performed a further study and clarified the detailed roles of various deformation in insects' aerodynamic performance. They concluded the spanwise twisting contributes to the power economy, and bending enhances the lift generation.

For larger flying creatures, like birds or bats, they prefer the active-controlled flexibility during flight[27]. After all, active morphing has more advantages in adapting to different complex flight conditions than passive morphing. Tian et al.[28] added active-controlled leading and trailing segments to a rigid plate to simulate the flexible wing. They found that the

power economy of the flexible wing is largely improved compared with the rigid wing or the passively flexible wing. Silva et al.[29] investigated the effects of active and passive control for acceleration reduction of a 2D flexible wing. Liu and Bose[30] studied the propulsive performance of oscillating foils with spanwise flexibility using a time-domain panel method.

1.1.4 Formation and development of LEV

When a flapping wing travels several chord lengths, the flow separates from edges and forms large organized vortices: LEV, trailing-edge vortex (TEV), and tip vortex (TiV), as shown in Fig.1.1. Especially, the LEV, which creates a region of lower pressure above the wing surface, plays a dominant role in the force generation and rapid manoeuvring[31]. Maxworthy[32] studied the formation and maintenance of LEVs on the animal wings during the forward motion. For a two-dimensional wing, the vorticity is removed locally by unsteady vortex shedding. However, for an animal wing moved forward, which is a finite span, the flow separated from the sharp leading edge and generated vorticity, which was transported along spanwise LEVs and deposited to the TiVs.

In the early studies of insects' wings, researchers have noticed that the delayed stall vortex can significantly enhance the lift[12]. The prolonged attachment of LEV can also promote the lift to be increased[21]. But the mechanism behind the stability of LEV was still unclear. The dynamic stall vortex on an oscillating aerofoil easily breaks when the aerofoil starts to translate. The study of the formation and growth of LEV is still in the state of the art of aerodynamics.

The formation of the LEV is sustainably supplied by the separated shear layer[33]. How-

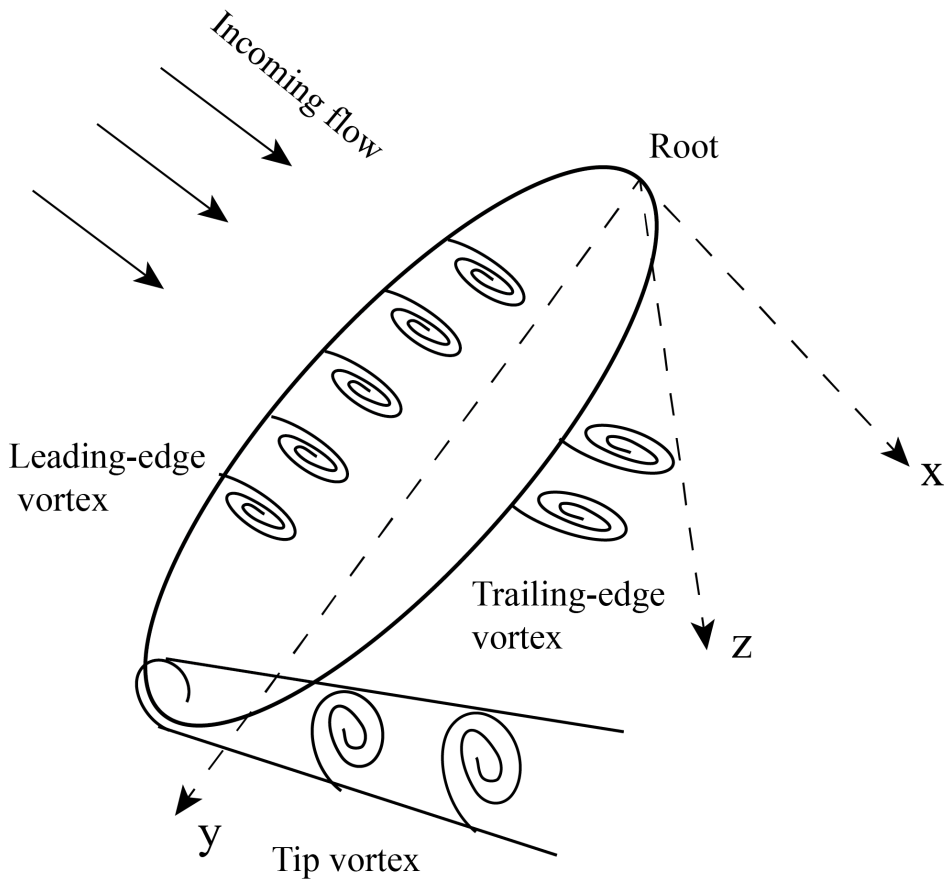

Figure 1.1: *Schematic of the three-dimensional flow over the top of the flapping wing at its mid-point.*

ever, there is a limitation of the size the LEV can grow. Dabiri[34] proposed and developed the concept of optimal formation time to mark this growth limitation. It is defined as the time that the LEV core is no longer able to sustain itself and is forced to cut off the supply of circulation from the leading edge. After the optimal formation time is reached, the vortex will pinch off and get shed in the downstream wake.

Rival et al.[35] utilized a topological argument and found that only vortices, which are smaller than the wing's chord, could stay stably attached to the wing. Ellington et al.[36] proposed that the stability of the LEV can be improved by the spanwise flow, which helps

to remove vorticity from the LEV core to the tip vortices. Wong and Rival[37] found that spanwise vorticity convection and vortex stretching have significant effects on the growth of LEV. Wong and Rival[38] found that the attachment of vortex of a 2D flapping wing can be prolonged by the spanwise vorticity convection, which drains circulation from the LEV. Their further study[39] demonstrated that the phase delay between spanwise bending and flapping motion also has an important influence on the stability of the LEV. Jia et al.[2] conducted experiments and direct numerical simulations to investigate the changes in the vortex dynamics of a flat plate undergoing a gradual spanwise bending when accelerated from rest to a Re of 2400. They found that the action of bending delays the growth of the LEV.

1.2 Concepts of flexible wing

According to whether flyers have the ability to change the wing shape, the deformation of flexible wings can be divided into passive-controlled and active-controlled. As mentioned above, most species of insects' wings are deformed passively, and birds and bats can flex their wings actively. In the wing design area, the deformation patterns can be classified into two categories: the aerofoil-level morphing (2D) and the wing-level morphing (3D)[40].

1.2.1 Aerofoil-level morphing

The aerofoil morphing is implemented by variable chamber and thickness[40]. It is designed to reduce drag and improve lateral stability during the take-off and landing phases of flight.

Morphing leading-edge

The design of the morphing leading-edge faces challenges like small design space and large curvature at the wing leading edge. Kintscher et al.[41] applied an adaptive morphing droop-nose into the wing leading edge and tested the model in the wind tunnel. The morphing leading-edge wing can suppress the noise and reduce drag by promoting the surrounding flow to be laminar[42].

Morphing trailing-edge

The concept of morphing trailing-edge is proposed to design a smooth wing surface without additional gaps to improve energy efficiency or reduce drag. A popular design of the morphing trailing-edge is to put flexible ribs in the airfoil, whose position can be changed by actuators[43].

Variable thickness

Another uncommon design to reduce drag is to change the airfoil thickness over the wing camber, which requires a more complicated mechanical structure. This design can enlarge the area of laminar regions over the wing surface by pushing the location of the laminar-to-turbulent flow transition towards the trailing-edge[44]. Popov et al.[45] designed such a morphing wing by a real-time optimization and observed such delay of transition location in a wind tunnel test.

1.2.2 Wing-level morphing

Compared with the airfoil-level morphing, the wing-level morphing changes the entire wing shape, which involves bending, twisting, sweep, and folding.

Spanwise bending

In the flapping-wing flight, the spanwise morphing mainly refers to the spanwise bending. Wings with a high aspect ratio (AR) have advantages in the energy economy but lack maneuverability. On the contrary, wings with a low AR have faster cruise speeds but cost more energy. A flexible wing with spanwise bending can balance the advantages of these two configurations. Shyy et al.[27] simulated a computational model of the anisotropic hawkmoth wing by combining different stiffness materials. Ajaj et al.[46] utilized the compliant spars to actively control the bending of wings. Tarabi et al.[47] compared several spanwise morphing wing models in a wind tunnel and demonstrated that the spanwise bending could increase flight endurance and reduce drag.

Twisting

The twisting is one of the most important and widely applied deformation patterns in nature. It can modify the lift or pressure distribution along the wing surface by inducing 'wash-in' and 'wash-out' morphing. Besides these, it can reduce maneuver loads and take the place of conventional control surfaces simultaneously. Vos et al.[48] designed an active-controlled twisting wing to help the aircraft to achieve a higher lift-to-drag ratio at lower angles of attack. Rodrigue et al.[49] designed a two-segment twisting wing, whose base segment is fixed and the tip segment is actuated. Raither et al.[50] designed a semi-passive twisting wing,

which improves thrust with smaller weight and higher energy efficiency.

Variable sweep

The variable-sweep wing concept was first proposed to help the military fighter aircraft obtain supersonic cruising speeds in the 1950s. Nowadays, it is also applied in the design of MAVs and UAVs to adapt to complex missions, like locomotion in both air and water. Laursen[51] took inspiration from swift birds and utilized discrete feather-like elements to design the variable-sweep wing, which can change its sweep angle by folding feathers backward. Xu et al.[52] studied the dynamic responses of several variable-sweep wing prototypes and concluded that the variable-sweep wings have non-negligible effects on the pitch.

Folding

The folding wing can change the wing area and, therefore, improve the performance in climb rate, stall characteristics, and lateral stability. Lentink et al.[53] noticed that pigeons and swifts in nature could utilize their folding wings to glide in flight to save energy. Ma et al.[54] studied the effects of an active folding deformation on aerodynamic forces by imitating bats' motion. Mills and Ajaj[55] conducted wind tunnel experiments to investigate the effects of folding wings on flight stability under large dynamic pressures. Wang and Dowell[56] investigated and measured the natural frequencies of folding wings through series of experiments and compared the experimental results with the analytic frequencies estimated by a structural dynamics model.

1.3 Optimization design

The wing design usually involves many control variables, such as the shape variables, structural variables, and kinematic variables. It is impossible and unnecessary to conduct a complete parametric study to achieve the optimal control of flexible wings for specific objectives. The optimization approaches have been widely applied to help wings obtain a trade-off between aerodynamic forces, energy economy, and structural weight. Generally, the optimization techniques can be classified as gradient-based methods[57;58] and gradient-free methods[59–61] according to whether it needs the gradient information to update its control.

1.3.1 Gradient-based optimization

Gradient-based optimization are efficient at finding local minimum for high-dimensional and convex problems. Tuncer and Kaya[62] utilized the gradient descent method to optimize a flapping wing for the maximum thrust and efficiency. Their optimization followed the direction of the steepest ascent of the objective function, set as the combination of thrust coefficient and propulsive efficiency. Stanford and Beran[63] performed an analytical sensitivity analysis of a flapping wing with active shape morphing by the vortex lattice method. This method can reduce the computational cost at the expense of losing certain fidelity. The adjoint-based approach has a huge advantage in the optimization with a large number of design variables compared with other gradient-based methods[57]. However, their work handled the physical moving boundary by a mapping function, which would cause a complicated formulation. Xu and Wei[64] utilized the non-cylindrical calculus to derive the continuous adjoint equations directly in a morphing domain and optimized the moving boundary in its original space

without using a mapping function.

1.3.2 Gradient-free optimization

The gradient-free methods are often used in global optimization. They are able to find multiple local optima while searching for the global optimum. Simulated annealing is a probabilistic technique for approximating the global optimum of a given function. Sonmez [65] utilized this method to find globally optimal shapes for two-dimensional structures subject to quasi-static loads and restraints. The evolutionary algorithm is a generic population-based optimization algorithm inspired by biological evolution. All the candidate solutions are determined by the loss function or the fitness function. Kai et al. used the evolutionary algorithm to optimize a set of morphing curves [66].

1.4 Present work

Flight control and wing shape control are always in the state of the art of aerodynamics. The adjoint-based optimization approach, starting from the study of jet noise control [67], has been developed with the implementation of non-cylindrical calculus for moving boundary problems, such as the optimizations for 2D flapping plates [68] and 3D flapping rigid wings [69].

I wanted to use this powerful tool to explore the aerodynamic potential of the wings in terms of thrust and efficiency by introducing flexibility. And I also want to figure out the main roles in the change based on the optimization results. Meanwhile, I would like to investigate the effects of deformation on the stability of LEV from the perspective of vortex dynamics. To achieve these goals, we need to answer following questions:

- How do we simulate the different types of wing deformations?
- Can the aerodynamic performance be improved after introducing active-controlling flexibility? What are the corresponding optimal controls?
- What are the main roles behind the aerodynamic improvement after optimization?
- How does the spanwise bending affect the stability of LEV?

I introduced different types of active-controlled deformation (spanwise bending and twisting) to the rigid wing with optimized motions to explore the potentials in aerodynamic performance (corresponding to thrust and efficiency). The powerful adjoint-based optimization tool is also applied here to obtain the optimal control of deformation, which helps researchers understand the weights of different control parameters in the improvement. I also studied the effects of deformation on pressure distribution, the effective angle of attack, and other factors to reveal the physical mechanism behind the improvement. A high-fidelity numerical simulation is implemented to investigate the effects of bending on the LEV growth at $Re = 2400$ in Chapter 4. The circulation growth computed from numerical simulation matches well with the growth from the analytical model and experiments. Simultaneously, the vorticity dynamics revealed how the bending affects the LEV growth by modifying the vorticity convection flux.

The organization of this thesis is as follows. In Chapter 2, the numerical algorithms for the simulation and optimization are introduced to help readers have a preliminary understanding of the implementation of our simulation and optimization instead of treating them as black boxes. The benchmark case, in which a rigid flapping wing is optimized for maximum

propulsion, is conducted. Finally, the optimization for the propulsion efficiency of a rigid wing is supplemented. In Chapter 3, different deformation patterns are added to the rigid wing model to explore its aerodynamic potentials in terms of thrust and efficiency. The impacts of deformation on aerodynamics are also investigated. In Chapter 4, the LEV growth on a flat plate accelerating from rest to a Reynolds number of 2400 is simulated and compared with the PIV measure. Its stability is analyzed via vorticity convection. Conclusions are presented in Chapter 5.

The bibliography for individual chapters will be listed all together in the end.

Chapter 2

Numerical algorithms for simulation and optimization

In this chapter, I implemented the numerical algorithms for the simulation and optimization used in this dissertation. The flow is described by the incompressible viscous Navier-Stokes equation, and the wing is simulated by an ellipsoidal plate discretized by unstructured triangle elements. The fluid-structure interactions are resolved by immersed boundary method along with solid force projection. The adjoint-based approach with non-cylindrical calculus is developed to handle the moving boundary or morphing domain in the optimization. At last, the thrust and efficiency of the rigid wing are optimized, respectively.

2.1 Governing equations and cost functions

The flow in this dissertation is described by the incompressible Navier–Stokes equations with solid boundary conditions,

$$\begin{aligned} \nabla \cdot \boldsymbol{u} &= 0 \\ \frac{\partial \boldsymbol{u}}{\partial t} + \boldsymbol{u} \cdot \nabla \boldsymbol{u} &= -\nabla p + \frac{1}{Re} \nabla^2 \boldsymbol{u} \quad \text{in } \Omega \end{aligned} \tag{2.1}$$

$$\begin{aligned} \boldsymbol{u} &= \boldsymbol{V} \quad \text{on } S \\ \boldsymbol{u} &= 0 \quad \text{on } \Gamma_\infty \\ \frac{\partial p}{\partial n} &= 0 \quad \text{on } \Gamma_\infty \end{aligned} \tag{2.2}$$

where Ω, $\mathcal{S}$, and Γ_∞ stands for the fluid domain, the solid boundary, and the far-field boundary, respectively. $\boldsymbol{u} = [u, v, w]$ is the flow velocity vector, $\boldsymbol{V}$ is the velocity vector at the solid boundary, and $\boldsymbol{n}$ is the normal unit vector at the Γ_∞. For convenience, the governing equations can be expressed using the Navier-Stokes operator $\mathcal{N}$ and flow varialbe $\boldsymbol{q} = [p \quad \boldsymbol{u}]^T$

$$\mathcal{N}(\boldsymbol{q}) = 0 \tag{2.3}$$

In this chapter, I mainly focus on the thrust and efficiency of wings. When I am going to pursue the optimal thrust of wings, the objective function $\mathcal{J}$ is defined as negative thrust coefficient C_T,

$$\mathcal{J} = -C_T \tag{2.4}$$

$$C_T = -\frac{\overline{F_x}}{D_0} = -\frac{1}{TD_0}\int_0^T \int_{\mathcal{S}} \boldsymbol{\sigma}_1 \cdot \boldsymbol{n} \mathrm{d}s\mathrm{d}t \tag{2.5}$$

where $\overline{F_x}$ is the average force along x direction in the flapping period T, D_0 is defined as $D_0 = U^2 A/2$ with the wing area A and the coming velocity U. The stress σ_{ij} is defined as

$$\sigma_{ij} = -\frac{p}{\rho}\delta_{ij} + \nu(\frac{\partial u_i}{\partial x_j} + \frac{\partial u_j}{\partial x_i}) \tag{2.6}$$

where δ_{ij} is Kronecker's delta, and $\boldsymbol{\sigma}_1 = \sigma_{1j}$ represents the stress contributing to the thrust force along the x direction.

Sometimes flyers pay more attention to energy efficiency than maximum thrust. By setting the cost function as $\mathcal{J} = -\eta$, the optimization of efficiency can be regarded as a minimization problem same as the optimization of thrust,

$$\eta = \frac{P_0}{P_c} \tag{2.7}$$

$$P_0 = -\frac{1}{T}\int_0^T \int_{\mathcal{S}} U(\boldsymbol{\sigma}_1 \cdot \boldsymbol{n}) \mathrm{d}s\mathrm{d}t \tag{2.8}$$

$$P_c = -\frac{1}{T}\int_0^T \int_{\mathcal{S}} (\boldsymbol{u} - \boldsymbol{U}) \cdot (\boldsymbol{\sigma} \cdot \boldsymbol{n}) \mathrm{d}s\mathrm{d}t \tag{2.9}$$

where P_0 and P_c stand for the output power of propulsion and the total consumed power over one period. $\boldsymbol{U} = (U, 0)$ is the velocity at far field.

2.2 Immersed boundary method

The immersed boundary method (IBM) proposed by Peskin[70] has proved its excellent ability to handle the complex motion or metabolic solid shape in fluid-structure interaction (FSI) problems[68;71–74]. Its innovative procedure utilizes two sets of independent grids: a fixed Eulerian grid for the fluid flow and a moving Lagrangian grid for the immersed boundary, as shown in Fig. 2.1. A simple interpolation rule transfers the information between two sets of meshes. Simultaneously, this method considers the effects of the solid on the fluid as an external force term in the fluid governing equations and solves these equations over the entire computational domain. Its most distinct advantage is avoiding the grid's requirement to conform to the complex geometrical structure of the solid[75]. In our studies, the immersed boundary method (IBM) is applied to treat the moving boundaries for both the forward and backward simulation.

In addition, the immersed boundary method can be divided into the continuous forcing approach and the discrete forcing approach based on when to discrete the forcing term. In the continuous forcing approach, the forcing term is directly added to the continuous governing equations. In the discrete forcing approach, the forcing term is discretized firstly, then added to the discretized governing equations[76]. In our dissertation, we utilized the discrete forcing approach to deal with the solid boundary.

2.3 The adjoint analysis via non-cylindrical calculus

The adjoint-based approach is efficient and powerful for the problem with a large control space because its computational cost is independent of the size of the control space[77]. And

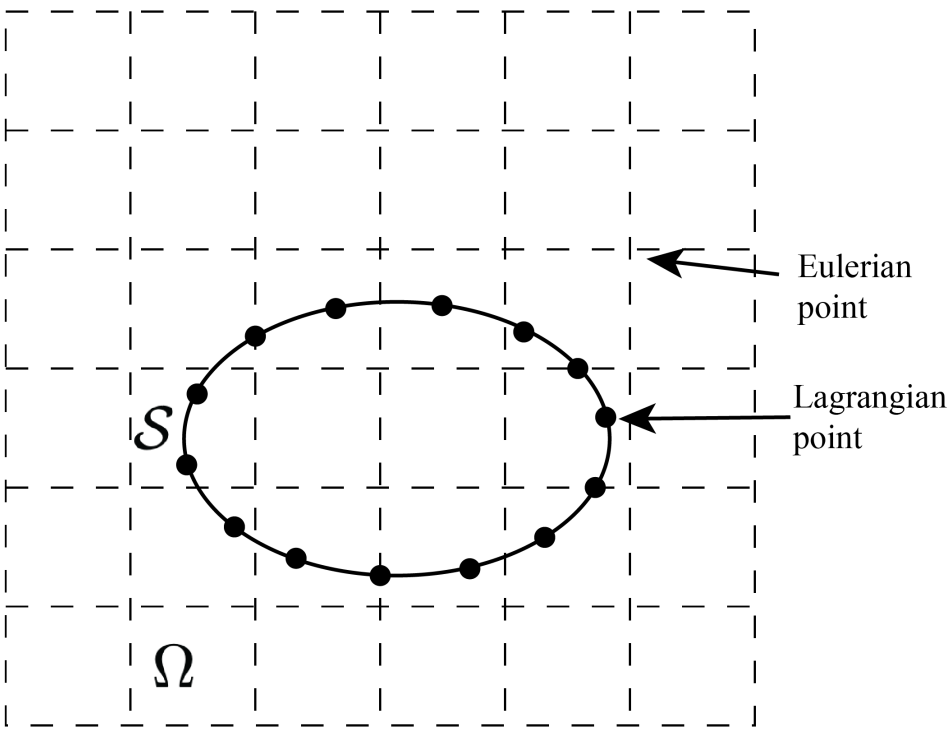

Figure 2.1: *Schematic drawing of the immersed boundary method. The fluid domain is denoted by* Ω*, and the boundary of solid is denoted by* $\mathcal{S}$*. The fluid points are represented by the interaction points of dashed lines (Eulerian points), and the boundaries are represented by the Lagrangian points.*

the non-cylindrical calculus provides an easy extension of the traditional adjoint-based approach to handle the optimization involving moving boundaries.

2.3.1 Non-cylindrical calculus

As shown in Fig.2.1, the major difficulty of the moving domain problem is that it easily causes the discontinuity on the interface between fluid and solid[78]. The traditional adjoint-based method solves the moving domain problem by an unsteady mapping function to transfer the whole domain to a fixed computational domain[79]. However, it usually results in a very complicated formulation. While the non-cylindrical calculus only focuses on the change on the domain boundary, which greatly reduced the complexity[80].

For the domain Ω and control ϕ, the time evolution and control evolution can be described by the flow map $\mathcal{T}(t,\tau,\phi)$ and the transverse map $\widetilde{\mathcal{T}}(t,\epsilon,\phi)$, respectively.

$$\mathcal{T}(t,\tau,\phi) : \Omega(t,\phi) \to \Omega(t+\tau,\phi) \tag{2.10}$$

$$\widetilde{\mathcal{T}}(t,\epsilon,\phi) : \Omega(t,\phi) \to \Omega(t,\phi+\epsilon\phi') \tag{2.11}$$

Correspondingly, the flow map velocity $\mathbb{V}$ and the transverse map velocity Z are

$$\mathbb{V}(t,\phi,x) = \frac{\partial \mathcal{T}(t,\tau,\phi,x)}{\partial \tau}|_{\tau=0} \tag{2.12}$$

$$Z(t,\phi,x) = \frac{\partial \widetilde{\mathcal{T}}(t,\epsilon,\phi,x)}{\partial \epsilon}|_{\epsilon=0} \tag{2.13}$$

Then for any function $f(t,x)$, its perturbation derivative in Lagrangian point of view or so-called non-cylindrical material derivative is

$$\dot{f}(t,x) = \lim_{\epsilon\to 0} \frac{f(t,\phi+\epsilon\phi',\widetilde{\mathcal{T}}) - f(t,\phi,x)}{\epsilon} \tag{2.14}$$

its perturbation derivative in Eulerian point of view or so-called non-cylindrical shape derivative is

$$f' = \dot{f} - Z_i \frac{\partial f}{\partial x_i} \tag{2.15}$$

The transverse velocity and flow map velocity can be related by the non-cylindrical material derivative,

$$\dot{\mathbb{V}}_i = \frac{dZ_i}{dt} \tag{2.16}$$

2.3.2 Linearized perturbation equations

The adjoint-based optimization needs the gradient information $g(\phi)$ of the old control ϕ^{old}, which is derived from the sensitivity of the cost function $\mathcal{J}$ to the control ϕ, to update the new control ϕ^{new} in each iteration.

$$\phi^{new} = \phi^{old} - \alpha g(\phi^{old}) \tag{2.17}$$

where α is the step length.

The linearized perturbation equations are derived using shape derivative:

$$\begin{aligned} \nabla \cdot \boldsymbol{u'} &= 0 \\ \frac{\partial \boldsymbol{u'}}{\partial t} + \nabla \cdot (\boldsymbol{u'u} + (\boldsymbol{u'u})^T) &= -\nabla p' + \frac{1}{Re}\nabla^2 \boldsymbol{u'} \quad \text{in } \Omega \end{aligned} \tag{2.18}$$

$$\boldsymbol{u'} = \dot{\boldsymbol{V}} - Z \cdot \nabla \boldsymbol{u} \quad \text{on } S \tag{2.19}$$

Equation 2.18 can be expressed as

$$\mathcal{N}'(\boldsymbol{q'}) = 0 \tag{2.20}$$

where $\boldsymbol{q'} = [p' \quad \boldsymbol{u'}]^T$.

2.3.3 Adjoint equations and gradient calculation

The sensitivity of the cost function $\mathcal{J}$ to the control ϕ is defined by the perturbed function $\mathcal{J}'$ resulted from arbitrary perturbation ϕ'

$$\mathcal{J}' = \lim_{\epsilon \to 0} \frac{\mathcal{J}(\phi + \epsilon\phi') - \mathcal{J}(\phi)}{\epsilon} \tag{2.21}$$

Then introducing the adjoint variables $\boldsymbol{q}^* = [p^* \quad \boldsymbol{u}^*]^T$ as the Lagrange multiplier for the constraint of governing equations and adding it to the shape derivatives of the cost function.

$$\mathcal{J}'_{new} = \mathcal{J}' + \int_0^T \int_{\mathcal{S}} \boldsymbol{q}^* [\mathcal{N}'(\boldsymbol{q}')] \mathrm{d}s\mathrm{d}t \tag{2.22}$$

After integration by part, we obtain

$$\mathcal{J}'_{new} = b - \int_0^T \int_{\mathcal{S}} \boldsymbol{q}' [\mathcal{N}^*(\boldsymbol{q}^*)] \mathrm{d}s\mathrm{d}t \tag{2.23}$$

where b is the boundary term, $\mathcal{N}^*(\boldsymbol{q}^*)$ are the adjoint equations,

$$\begin{aligned} \nabla \cdot \boldsymbol{u}^* &= 0 \\ \frac{\partial \boldsymbol{u}^*}{\partial t} + \boldsymbol{u} \cdot (\nabla \boldsymbol{u}^* + \nabla \boldsymbol{u}^{*\boldsymbol{T}}) \cdot &= -\nabla p^* - \frac{1}{Re} \nabla^2 \boldsymbol{u}^* \quad \text{in } \Omega \end{aligned} \tag{2.24}$$

However, the boundary conditions of the adjoint equations will vary with the objective

function $\mathcal{J}$. In the implementation of thrust optimization, the boundary conditions are

$$\begin{aligned} \boldsymbol{u}^* &= -\boldsymbol{\delta_1} \quad \text{on } \mathcal{S} \\ \boldsymbol{u}^* &= 0 \quad \text{on } \Gamma_\infty \\ p^* &= 0 \quad \text{on } \Gamma_\infty \end{aligned} \tag{2.25}$$

with $\boldsymbol{\delta_1} = \delta_{1j}$. And in the implementation of efficiency optimization, the boundary conditions are

$$\begin{aligned} \boldsymbol{u}^* &= -\frac{1}{P_c}\boldsymbol{\delta_1} + -\frac{P_0}{P_c^2}(\boldsymbol{u} - \boldsymbol{U}) \quad \text{on } \mathcal{S} \\ \boldsymbol{u}^* &= 0 \quad \text{on } \Gamma_\infty \\ p^* &= 0 \quad \text{on } \Gamma_\infty \end{aligned} \tag{2.26}$$

When both the flow and adjoint solutions are periodic, the gradient of cost function $\mathcal{J}$ with respect to controls ϕ for the thrust optimization is then given by

$$g_l = \frac{\partial \mathcal{J}}{\partial \phi_l} = -\frac{1}{TD_0}\int_0^T \int_{\mathcal{S}} \left[Z_{k,l}\frac{\partial \sigma_{1j}}{\partial x_j} n_k - \left(\dot{V}_{i,l} - Z_{k,l}\frac{\partial u_i}{\partial x_k} \right) Z_i^* \right] \mathrm{d}s\mathrm{d}t \tag{2.27}$$

where

$$\dot{V}_{i,l} = \frac{\partial V_i}{\partial \phi_l}, \quad Z_{i,l} = \frac{\partial S_i}{\partial \phi_l}, \quad Z_i^* = \sigma_{ij}^* n_j + u_j^* u_j n_i \tag{2.28}$$

Correspondingly, for the efficiency optimization, the gradient of cost function $\mathcal{J}$ with respect to controls ϕ is given by

$$g_l = \frac{1}{T}\int_0^T \int_{\mathcal{S}} \left[-Z_{k,l}\left(U_i^* \frac{\partial \sigma_{ij}}{\partial x_j} + \frac{P_0}{P_c^2}\frac{\partial u_i}{\partial x_j}\sigma_{ij} \right) n_k - \left(\dot{V}_{i,l} - Z_{k,l}\frac{\partial u_i}{\partial x_k} \right) Z_i^* \right] \mathrm{d}s\mathrm{d}t \tag{2.29}$$

with $Z_i^* = \sigma_{ij}^* n_j + u_j^* u_j n_i + \frac{P_0}{P_e^2}\sigma_{ij} n_j$. The control being updated by the gradient leads to the decrease of the cost function in optimization. More details are listed in our previous work.[64]

2.4 Numerical algorithms

A staggered Cartesian mesh with stretching functions as local refinement is utilized in our simulation due to its benefits of computational efficiency and numerical stability. For the spatial discretization and the time advancement, we chose the second-order central difference scheme and the second-order Adams-Bashforth/Crank-Nicolson scheme, separately. The pressure Poisson equation was solved by Fast Fourier transform (FFT) and a generalized cyclic reduction algorithm[81]. At the same time, a typical projection method for incompressible flow conditions is applied. The time step is limited by the Courant–Friedrichs–Lewy (CFL) constraint[64;69;82].

$$CFL = \Delta t \max(\frac{|u_i|}{\Delta x_i}) \leq \sqrt{3} \tag{2.30}$$

The flow velocities, which will be used in the adjoint simulation, are saved in single-precision very other time steps to reduce the data storage pressure. The gradient of the cost function with respect to all the control parameters could be calculated after both the low and adjoint equations were solved once. To reduce the running time and computational intensity in 3D simulation, parallelization is carried out via domain decomposition along one chosen direction. The communication between neighboring blocks is implemented using the MPI library.

2.5 Numerical configuration

2.5.1 Kinematics setup

As shown in Fig.2.2, its root is fixed at the origin point of the coordinate. The wing is rolling along the global x-axis and pitching around its local spanwise z' axis. The rolling

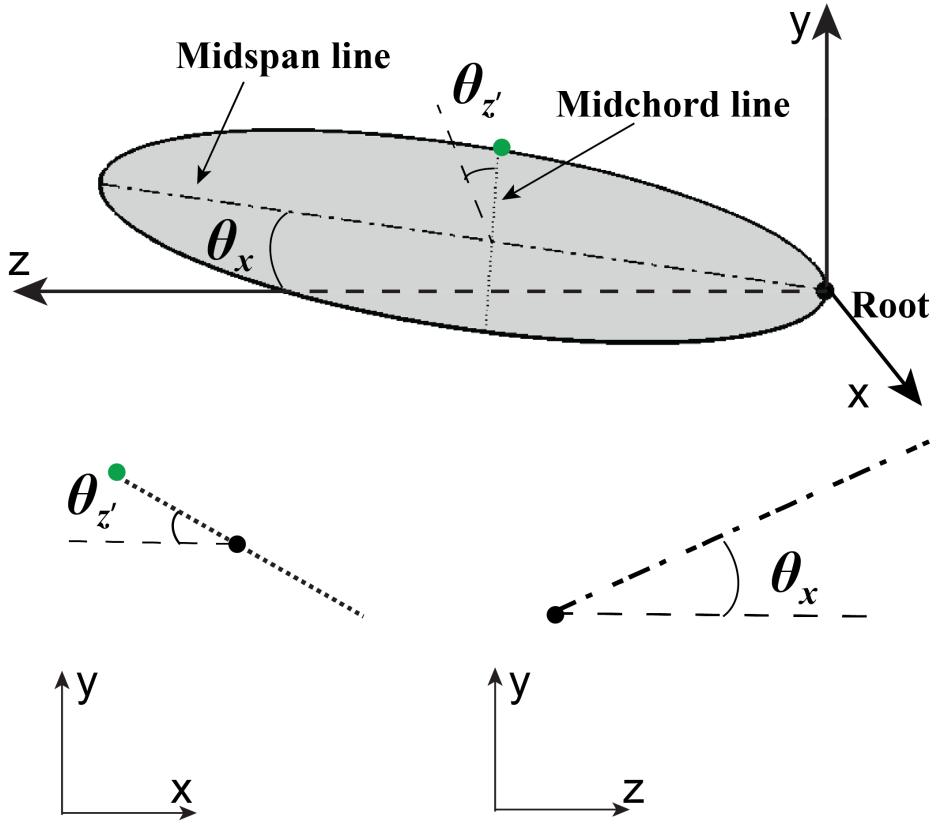

Figure 2.2: *Schematic of the global perspective and the two-dimensional views of the three-dimensional rigid wing*[1].

and pitching equations are

$$\begin{aligned} \theta_x &= -a_x \sin(2\pi f t) \\ \theta_{z'} &= -a_z \sin((2\pi f t + \varphi_z) \end{aligned} \tag{2.31}$$

where θ_x and $\theta_{z'}$ are the instantaneous rolling and pitching angles, a_x and a_z are the amplitudes of rolling and pitching motions, φ_z is the phase difference between the rolling and pitching motions, and $f = 1$ is the flapping frequency.

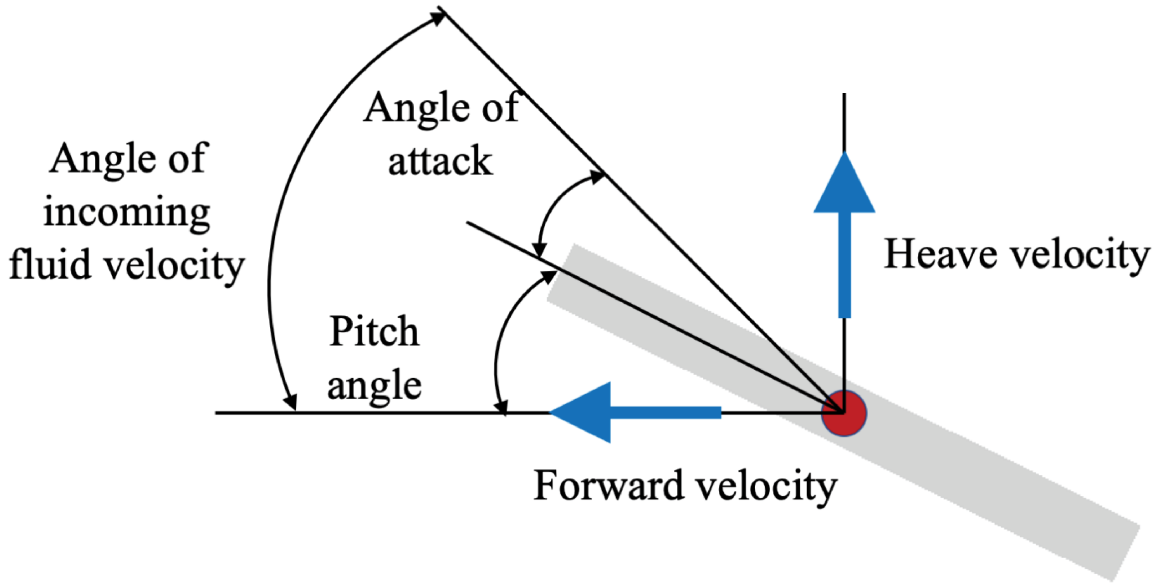

Figure 2.3: *Definition of the angle of attack for the rigid wing*[1].

The effective angle of attack α_r of the rigid wing is related to the local two-dimensional heaving and pitching motions. It varies with span location on the wing. The vector diagram of the velocity components is presented in Fig.2.3.

$$\begin{aligned} \alpha_r(t) &= \tan^{-1}\left(\frac{\dot{\theta}_x R}{U_\infty}\right) - \theta_{z'}(t) \\ &= \tan^{-1}\left(\frac{-2\pi f a_x R\cos(2\pi f t)}{U_\infty}\right) - \theta_{z'}(t) \end{aligned} \tag{2.32}$$

where R is the length from root along span.

In this dissertation, the dynamic motions of the wing are controlled by the prescribed

kinematics, which is mathematical and does not involve any forces associated with those motions. Our research focuses on how birds or MAVs utilize active control to optimize the movement or deformation of their wings to achieve optimal aerodynamic performance, rather than on internal actuation mechanisms. Therefore, we ignore the definition of the material or biological properties of the wings.

2.5.2 Solid and fluid meshes

The solid wing model and the computational mesh are presented in Fig.2.4. The wing is simulated by an ellipsoidal plate discretized by unstructured triangle elements. The non-dimensional span length of the wing is $l = 1$, the mid chord length is $c = 0.5$, and the thickness is $h = 0.05$. The Cartesian mesh is stretched in the x and y directions and uniform in the z-direction. It is refined and clustered uniformly near the solid region. The total size of this grid is $240 \times 200 \times 200$ in the domain $24c \times 16c \times 6c$, and its minimum spatial resolution is $\Delta x = \Delta y = \Delta z = 0.03c$. The reason for choosing such a grid and a domain size is listed in the next section.

2.5.3 Grid independence

Before we start the optimization, the grid and domain independence is tested in Table .2.1 by simulations with the initial control. The results of the coarse grid are not sufficient for grid independence. The results of the finer mesh and larger domain are accurate enough but require too many computation resources. The normal grid shows a good balance between computational cost and accuracy. We mostly use the normal grid configuration to provide

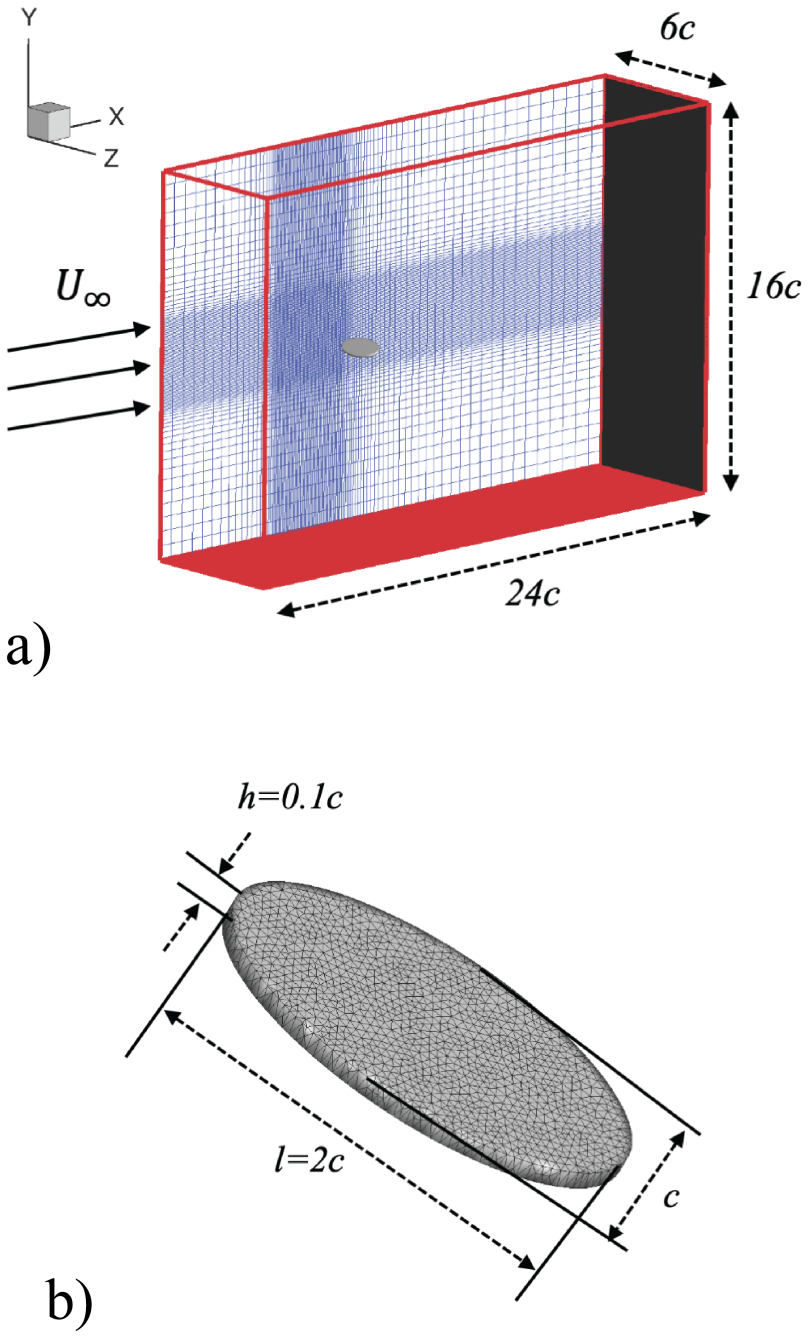

Figure 2.4: *Schematics of a) the computational domain and Cartesian mesh employed in the current simulation and b) a typical ellipsoidal plate used in the current study. The surface of the plate is represented by unstructured meshes made of triangular elements*[1].

computational results for the rest of this dissertation.

Table 2.1: *Results of grid and domain independence study with inital control.*

Grid	Grid size	Domain size	Minimum grid size	C_T
Coarse	$240 \times 140 \times 120$	$24c \times 16c \times 6c$	0.05c	0.32
Normal	$240 \times 200 \times 200$	$24c \times 16c \times 6c$	0.03c	0.29
Finer Mesh	$300 \times 260 \times 300$	$24c \times 16c \times 6c$	0.02c	0.28
Larger domain	$300 \times 240 \times 300$	$36c \times 24c \times 9c$	0.03c	0.29

2.6 Optimization for thrust

In this section, the adjoint-based optimization is applied to achieve the maximum thrust of the rigid rolling-pitching wing. The control ϕ in the optimization for thrust is defined as

$$\phi = (a_x, a_z, \varphi_z) \tag{2.33}$$

During optimization, these parameters are limited in the range listed in Table 2.2. The range

Table 2.2: *The range of control variables for thrust optimization.*

Parameters	Minimum, deg	Maximum, deg
a_x	0	45
a_z	0	45
φ_z	-180	180

of parameters is suggested by the study of the kinematics of the bluegill sunfish pectoral fin[83].

The initial control for the optimization is set as

$$\phi_{int} = (30°, 30°, 90°) \tag{2.34}$$

The optimization started from a random chosen initial control $\phi_{int} = (30°, 30°, 90°)$ and ended at the optimal control $\phi_{opt} = (45°, 35.9°, 122.6°)$. The initial control case in the optimization for thrust of rigid wings is marked as Rigid_Int, and the optimal control case is marked Rigid_Opt. Finally, the thrust coefficient C_T is improved from 0.29 to 2.39 by approximately eight times larger, as shown in Table 2.3. In the optimization, the rolling amplitude is improved to the upper bound limit.

Table 2.3: *The control parameters and thrust coefficients optimization in the current study.*

Case Name	a_x, a_z, φ_z	C_T	
Rigid_Int	$30°, 30°, 90°$	0.29	Initial control of the optimization for thrust of rigid wings
Rigid_Opt	$45°, 35.9°, 122.6°$	2.39	Optimal control of the optimization for thrust of rigid wings

The history of thrust coefficient C_T for the initial and optimal cases are compared in Fig.2.5. The peak of the thrust happens at about $t/T = 0/0.5/1.0$, when the plate is at the rolling middle position with the largest absolute rolling velocity. The small drags of the cases, which are generated when the wing is at the lowest or highest rolling position, are almost the same. The increased rolling amplitude contributes most to the improvement of thrust.

2.6.1 Effects on pressure distribution

The pressure distribution of the two cases when $t/T = 0$ is shown in Fig.2.6. After optimization, the pressure difference between the upper and lower surfaces is much higher. The regions with high pressure are at the leading edges near the wing tip.

The pressure distribution of the two cases when $t/T = 0.2$ is shown in Fig.2.7. At this

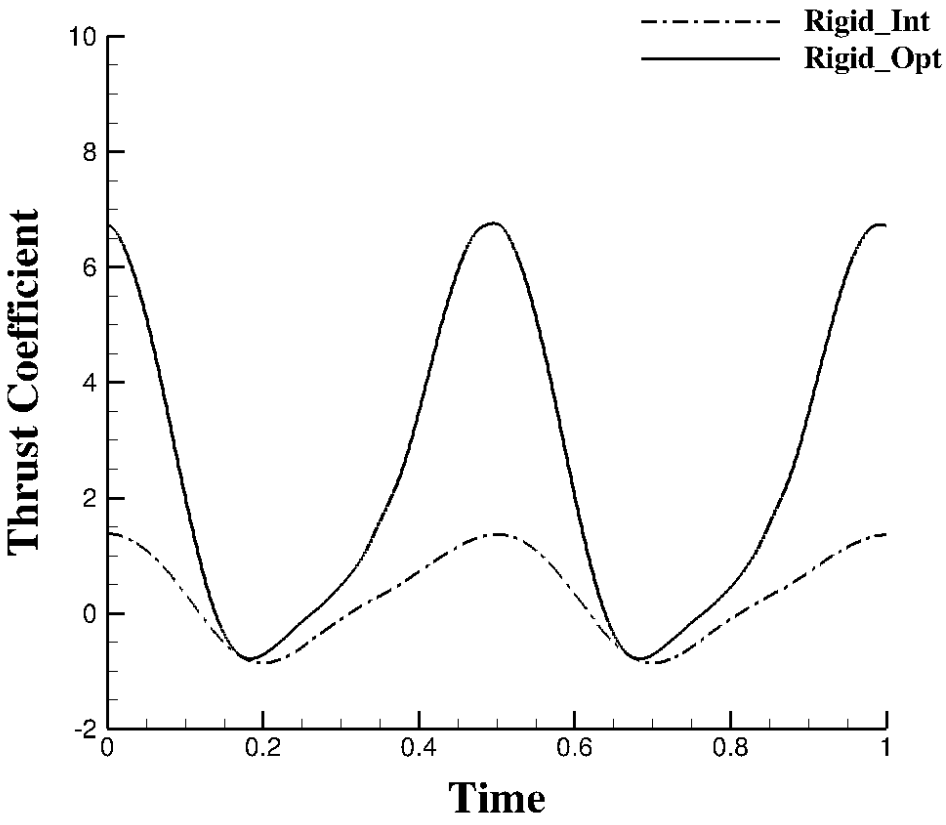

Figure 2.5: *Comparison of the instantaneous thrust coefficients of the rolling-pitching wing in initial and optimal cases.*

moment, the wing is at the end of the downstroke. In Fig.2.7 the pressure difference at the wing tips of the Rigid_Int case is larger than the pressure difference of the Rigid_Opt case, which corresponds to the larger drag in Fig.2.5.

2.6.2 Effects on effective angle of attack

The effective angles of attack at different span positions of the initial and optimal cases are compared in Fig.2.8. The percentage of the span is defined by R/l. After optimization, the magnitude of the peak angle is much improved. And for both cases, the magnitude of the angle of attack becomes larger when the position is closer to the tip.

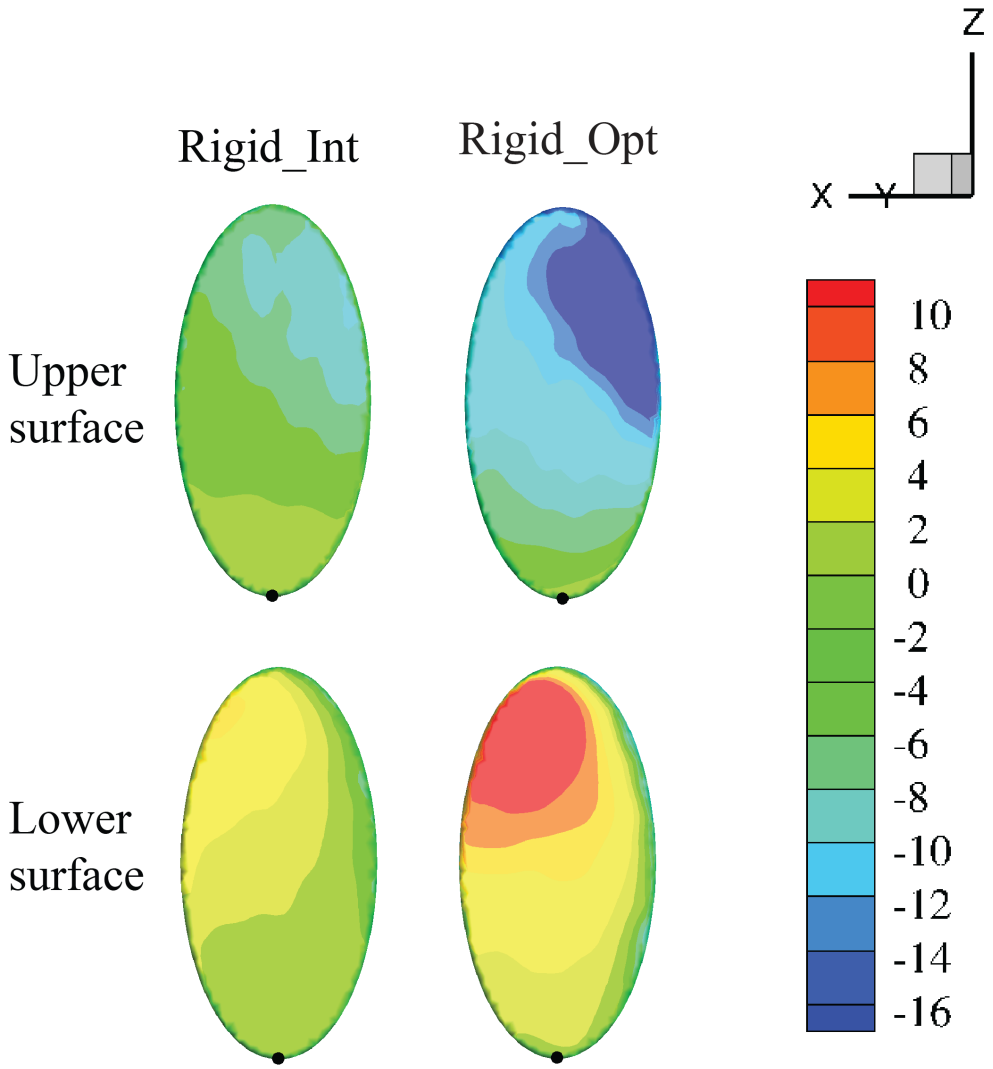

Figure 2.6: *The pressure distribution of the Rigid_Int and Rigid_Opt cases when* $t/T = 0$.

2.6.3 Effects on wake topology

The effects of the optimization on the wake topology are shown in Fig.2.9. To compare the effects on propagation and vortex strength simultaneously, two layers of the Q criterion are presented: $Q = 0.5$ for vortex shell (in gray) and $Q = 5$ for vortex core (colored by streamwise vorticity ω_x). For the initial case, the downstream vortex rings annihilate quickly. In the optimal case, the vortex strength is enhanced, and the shed vortex rings propagate a longer distance without annihilation.

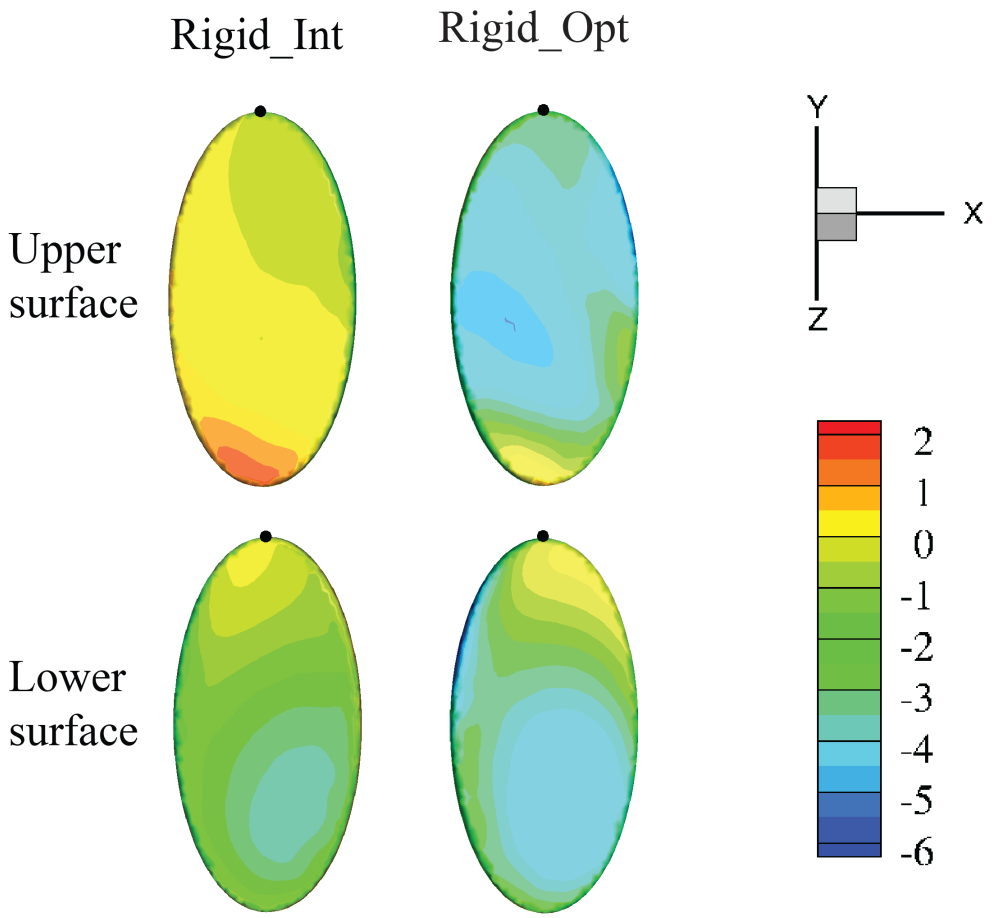

Figure 2.7: *The pressure distribution of the Rigid_Int and Rigid_Opt cases when* $t/T = 0.2$.

2.7 Optimization for efficiency

Sometimes natural flyers pay more attention to energy efficiency rather than to improve thrust endlessly. To explore the efficiency of rigid wings, we set the objective function as $\mathcal{J} = -\eta$, and chose the same control $\phi = (a_x, a_z, \varphi_z)$ and parameter range. As shown in Table 2.4, we set the control of Rigid_Opt case as the initial control of Rigid_Eff case. After two main iterations, the efficiency η is improved from 0.14 to 0.17 but the thrust coefficient is reduced from 2.39 to 1.97. And the optimal control for the efficiency is

$$\phi_{opt} = (45°, 45°, 102.1°) \tag{2.35}$$

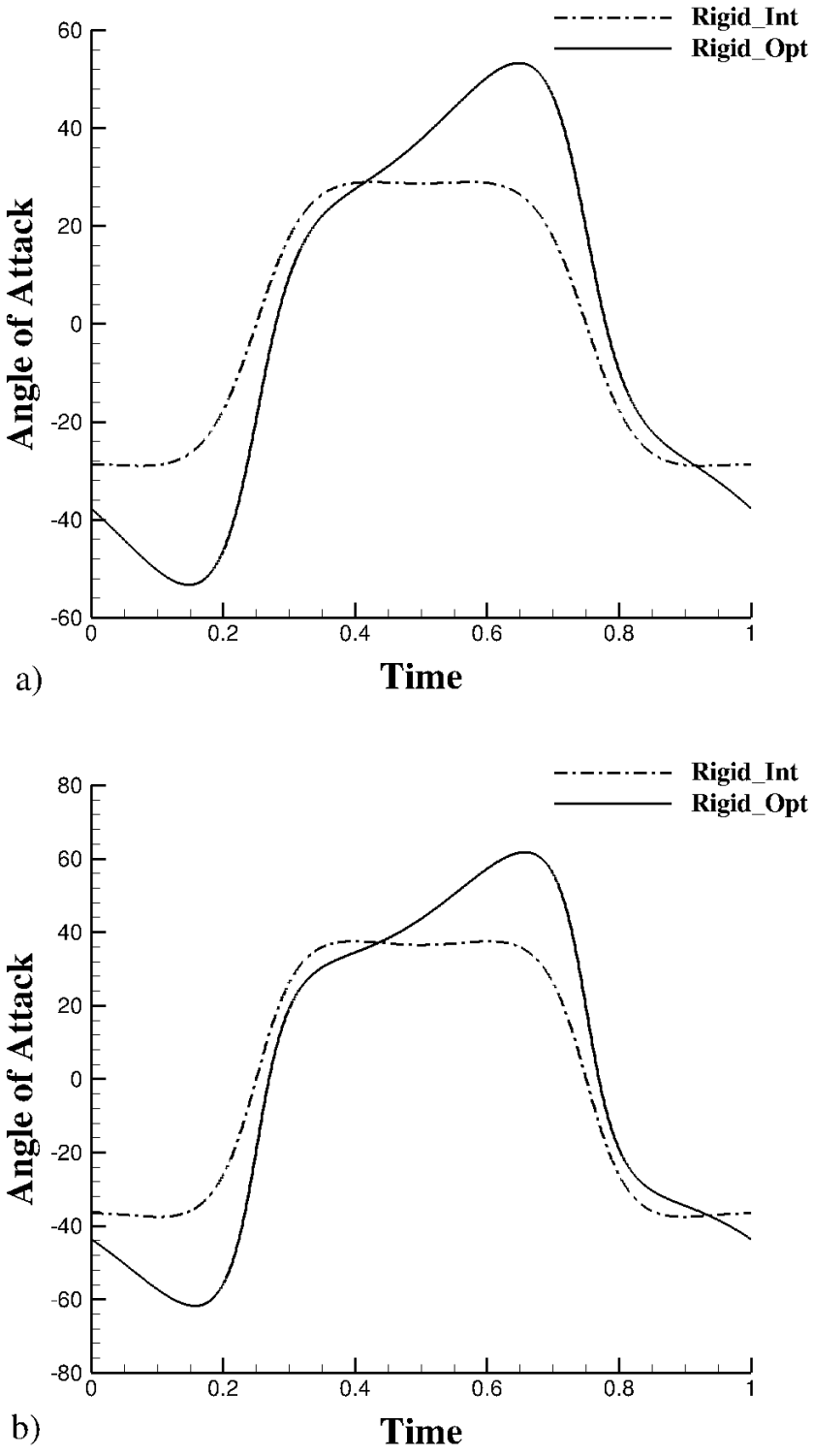

Figure 2.8: *Comparison of the angles of attack of the two cases at a)50% span, and b) 70% span.*

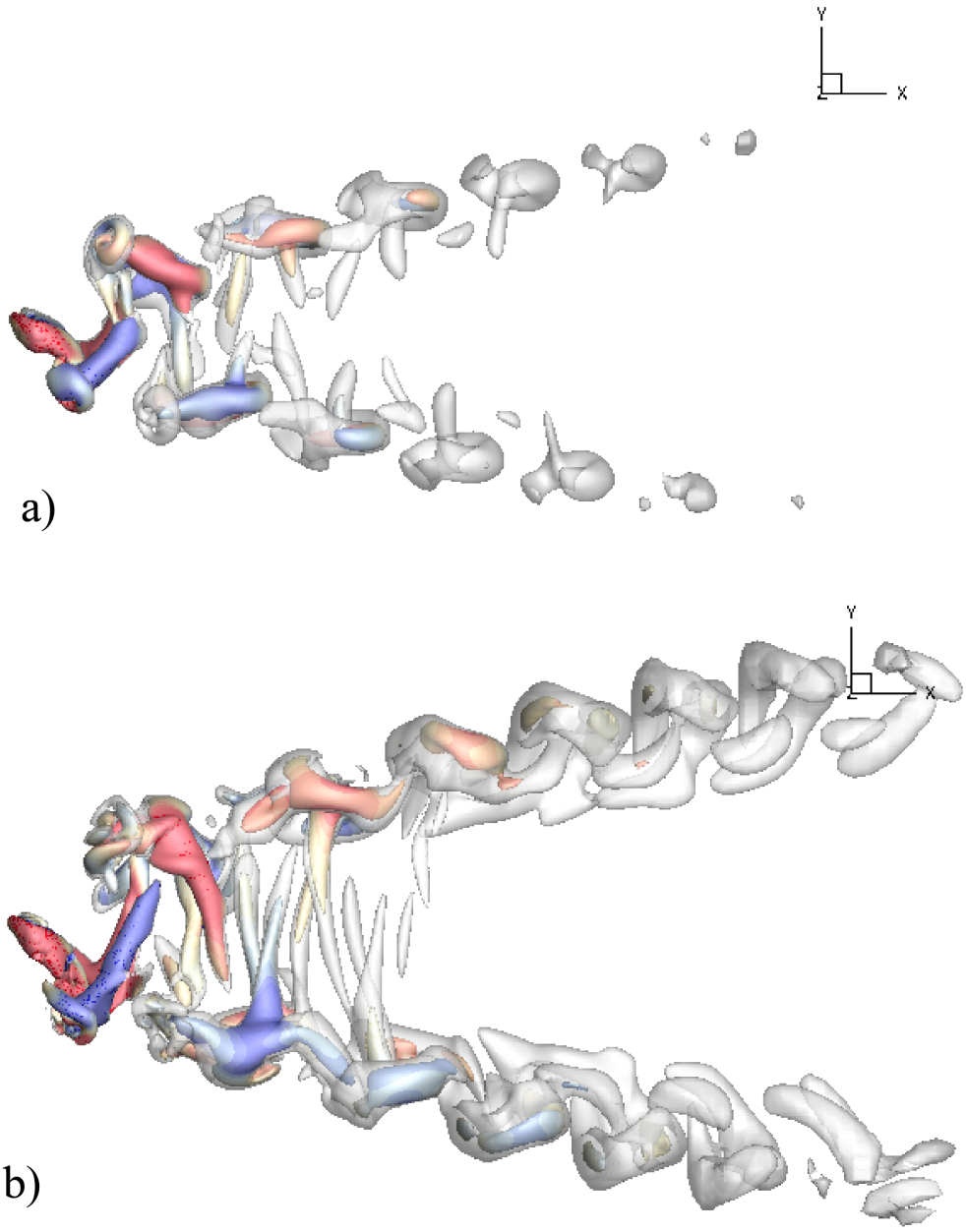

Figure 2.9: *Comparison of the wake topology of the rolling–pitching wing with the a) initial control, b) optimal control at* $t/T = 0$.

As shown in Fig.2.10, both the input power and output power are small in the Rigid_Int case. The magnitude of input power in the Rigid_Eff case is almost half of the magnitude in the Rigid_Opt case. Meanwhile, the magnitude of output power in the Rigid_Eff case is about 82.5% of the magnitude in the Rigid_Opt case. And the peak of the output power in

Table 2.4: *The control parameters, efficiencies, and thrust coefficients of different cases.*

Case Name	a_x, a_z, φ_z	η	C_T	
Rigid_Int	$30°, 30°, 90°$	0.06	0.29	———————————
Rigid_Opt	$45°, 35.9°, 122.6°$	0.14	2.39	Initial control of the optimization for efficiency of rigid wings
Rigid_Eff	$45°, 45°, 102.1°$	0.17	1.97	Optimal control of the optimization for efficiency of rigid wings

the Rigid_Eff case is delayed compared with the Rigid_Opt case.

2.7.1 Effects on pressure distribution

The pressure difference between the upper and lower surfaces of the three cases when $t/T = 0$ is shown in Fig.2.11. Compared with the Rigid_Opt case, the pressure difference in the Rigid_Eff is significantly reduced. It is slightly larger than the pressure difference in the Rigid_Int case.

2.7.2 Effects on effective angle of attack

The effective angles of attack of the initial and optimal cases are compared in Fig.2.12. After optimization, the magnitude of the angle of attack in Rigid_Eff is reduced compared with the Rigid_Opt case.

2.7.3 Effects on wake topology

The wake topology of the Rigid_Opt and Rigid_Eff cases are shown in Fig.2.13. The shell and core of the vortex structures are visualized in the same way as Sec.2.6.3. Though the thrust coefficient in the Rigid_Eff case is 17.6% smaller than the thrust coefficient in the

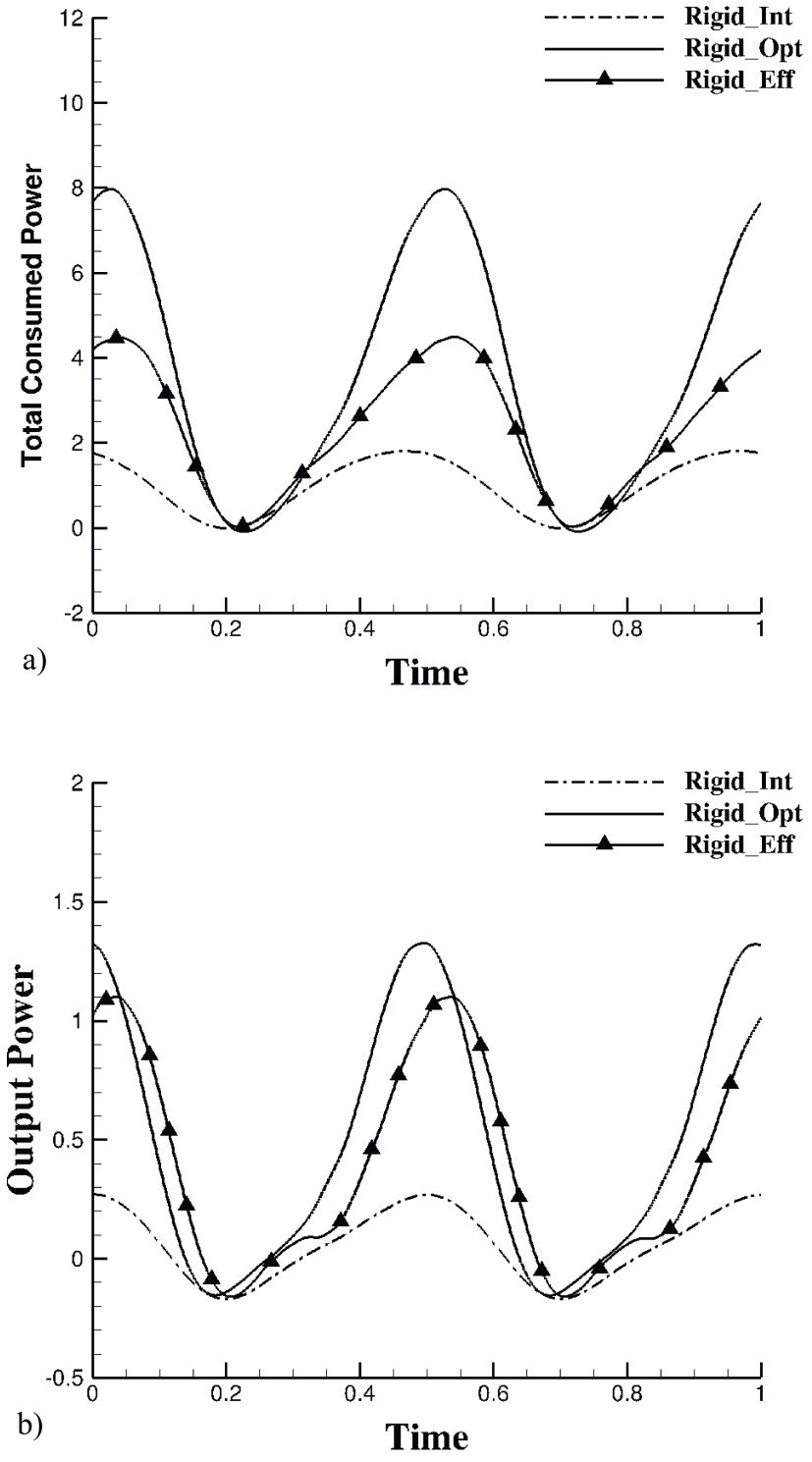

Figure 2.10: *The comparison of the instantaneous history of a) total consumed power P_c, and b) output power P_0 of different cases.*

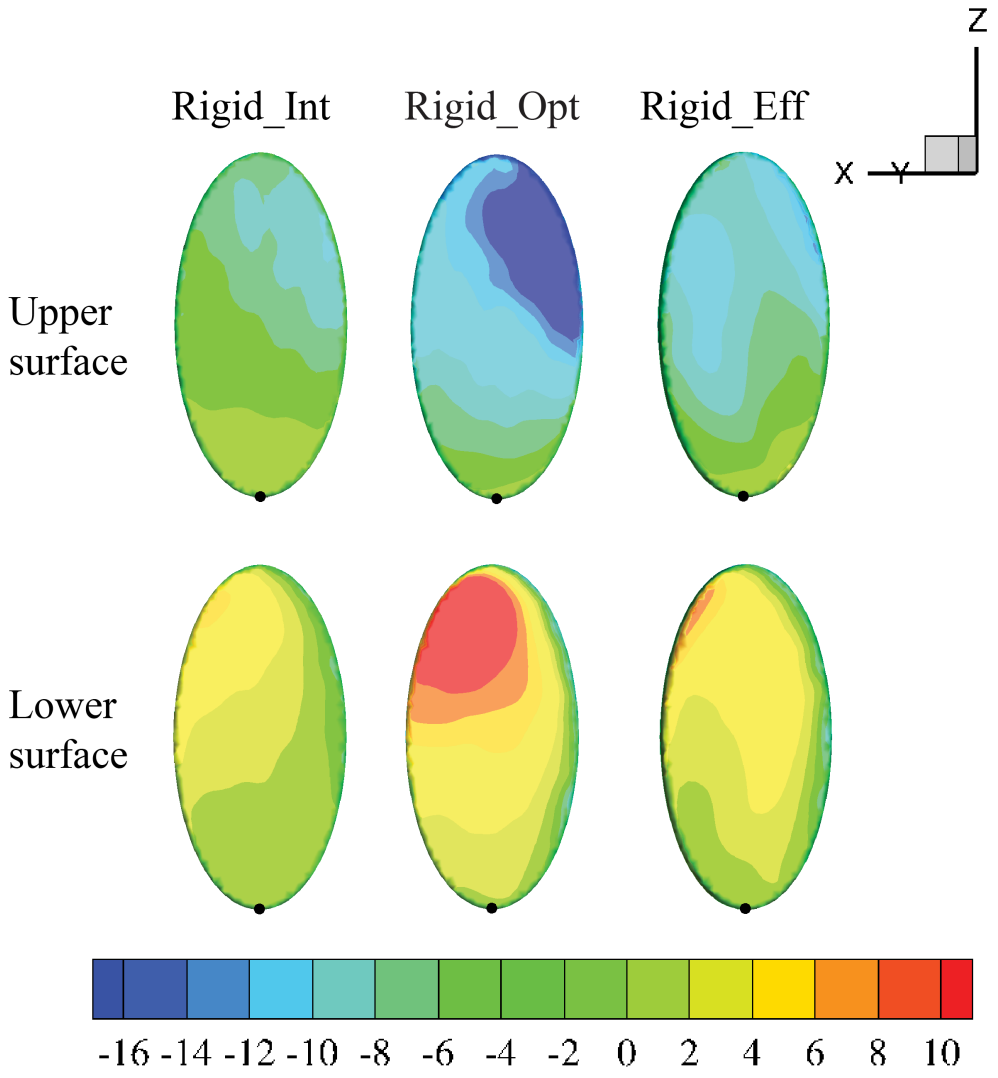

Figure 2.11: *The pressure distribution of three cases when* $t/T = 0$.

Rigid_Opt case, the downstream vortex rings annihilate quickly.

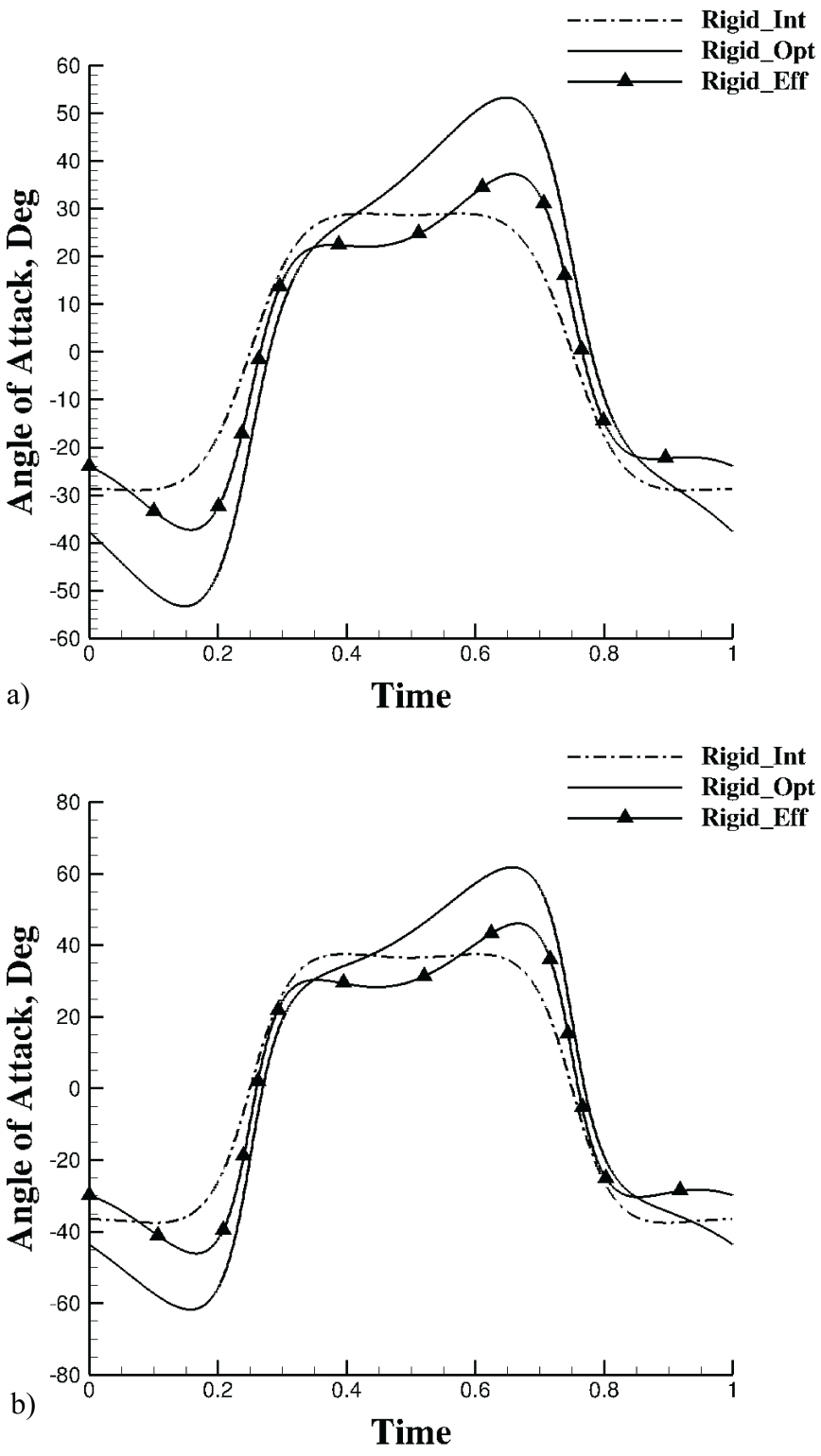

Figure 2.12: *Comparison of a) the angle of attack at 50% span, and b) the angle of attack at 70% span*

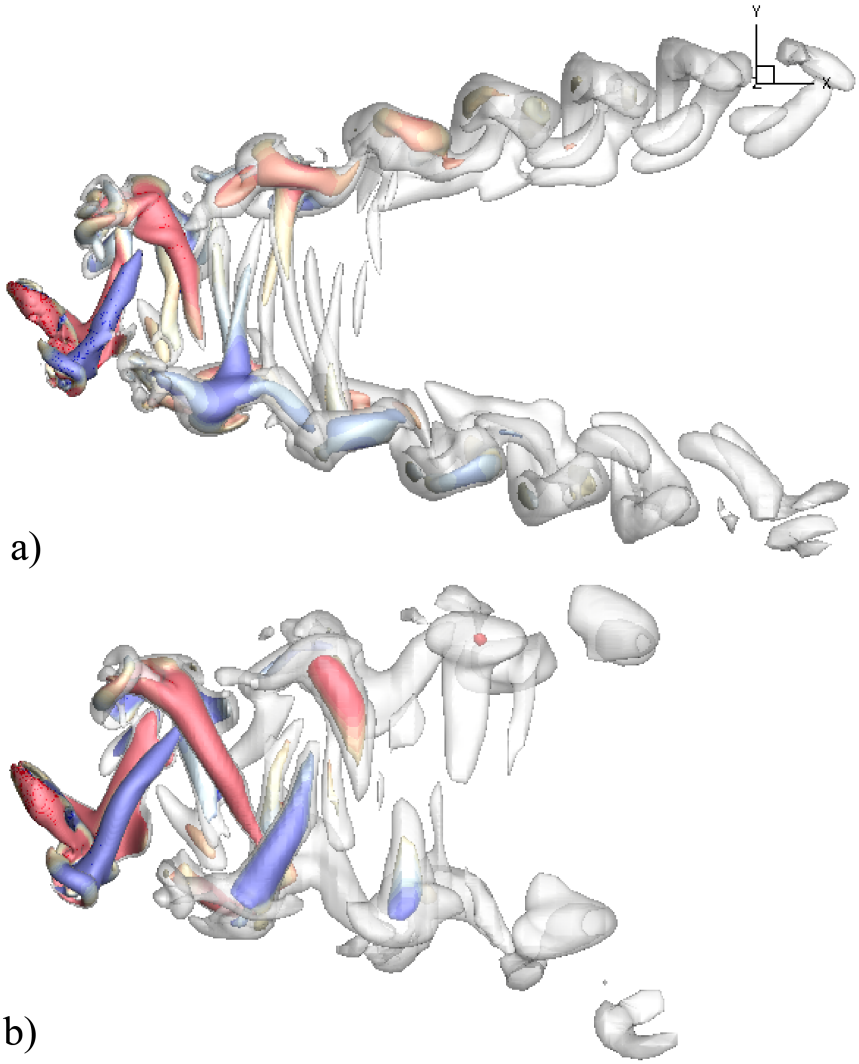

Figure 2.13: *Comparison of the wake topology of a) the Rigid_Opt case and b) the Rigid_Eff case at* $t/T = 0$.

Chapter 3

Optimization of flexible wings for thrust and efficiency

In this chapter, I introduced different types of active-controlled deformation (spanwise bending and twisting) to the rigid wing with optimized motions to explore the potentials in aerodynamic performance (corresponding to thrust and efficiency). I mimicked the spanwise bending by the natural modes of the cantilevered Euler-Bernoulli beam. The effects of wing shape on the thrust are also investigated by using more natural modes. The twisting deformation is modeled by following Manta's twisting pattern.

3.1 Spanwise bending modeling

The modeling logic of the wing's flexibility is shown in Fig.3.1. The wing's root is fixed at the body, which can be regarded as a cantilevered beam. Its deflection characteristics can be described by the Euler-Bernoulli beam theory, which is a linear theory of elasticity.

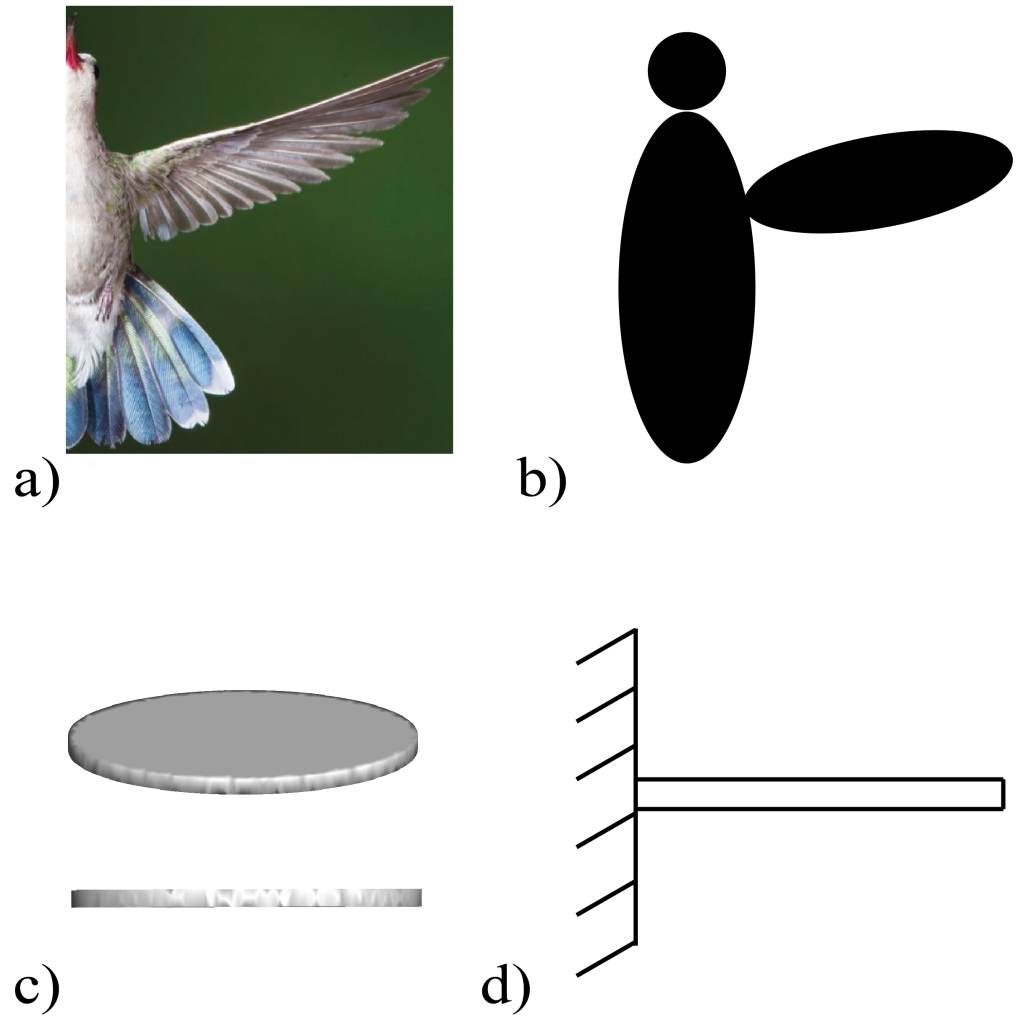

Figure 3.1: *The evolution from a biological wing to a cantilevered Euler-Bernoulli beam: a) the wing of a hummingbird, b) the numerical models of the bird's wing and body in the simulation, c) the wing model is mimicked by an ellipse plate, d) the deformation of a wing can be treated as the deflection of a cantilevered beam.*

3.1.1 Euler-Bernoulli beam solutions

The natural modes of the cantilevered Euler-Bernoulli beam can be used as the basis functions for the spanwise bending,

$$\psi_k(X) = C_k[\cosh \beta_k X - \cos \beta_k X + \frac{\cosh \beta_k X + \cos \beta_k X}{\sinh \beta_k X + \sin \beta_k X}(\sinh \beta_k X - \sin \beta_k X)] \qquad (3.1)$$

where X is the location of the points projecting on the X-axis in the undeformed Lagrangian coordinate, β_k is the kth solution of

$$\cosh(\beta_k L)\cos(\beta_k L) + 1 = 0 \tag{3.2}$$

C_k is the normalized coefficient to satisfy the condition

$$\max|\psi_k(X)| = 1 \tag{3.3}$$

The shapes of the first three natural modes and the corresponding β are shown in Fig.3.2.

3.1.2 Bending control

The deformation of the flexible wings can be defined as

$$\mathbf{s} = \sum_{k=1}^{n} a_k \sin(2\pi f t + \varphi_k)\psi_k(X)\mathbf{I} \tag{3.4}$$

where n is the degrees of freedom for flexibility. For the rigid wing, $n = k = 0$. $\mathbf{I} = (0, 1)$ means that the deformation is implemented in the normal direction of the undeformed surface (or along Y-axis in the undeformed Lagrangian coordinate), as shown in Fig.3.3. For convenience, we use s to take the place of $\mathbf{s}$.

The control for the bending in the optimization is set as

$$\phi_s = (a_1, \varphi_1, \cdots, a_n, \varphi_n) \tag{3.5}$$

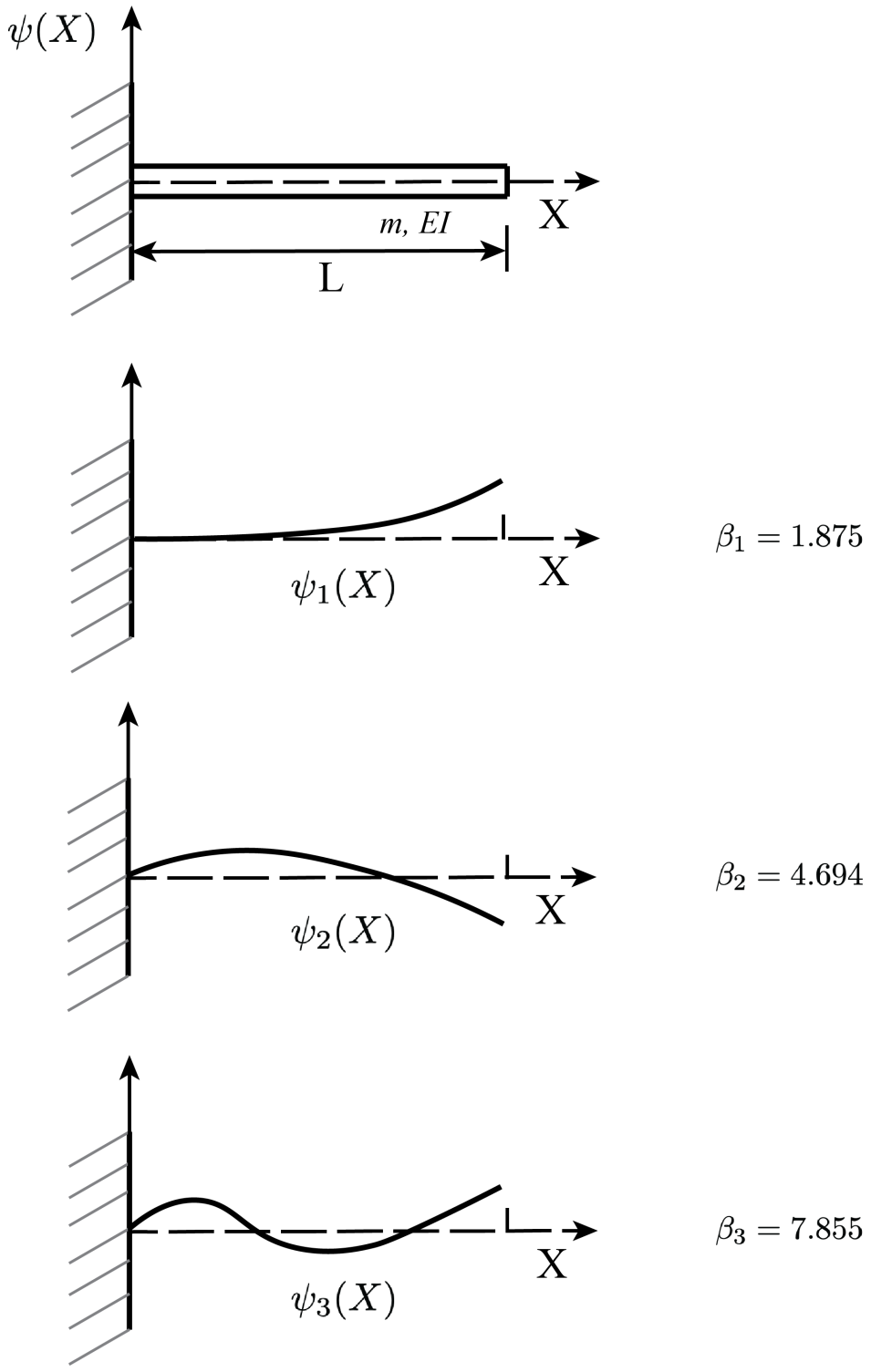

Figure 3.2: *Shapes of the first three natural modes of the cantilever beam.*

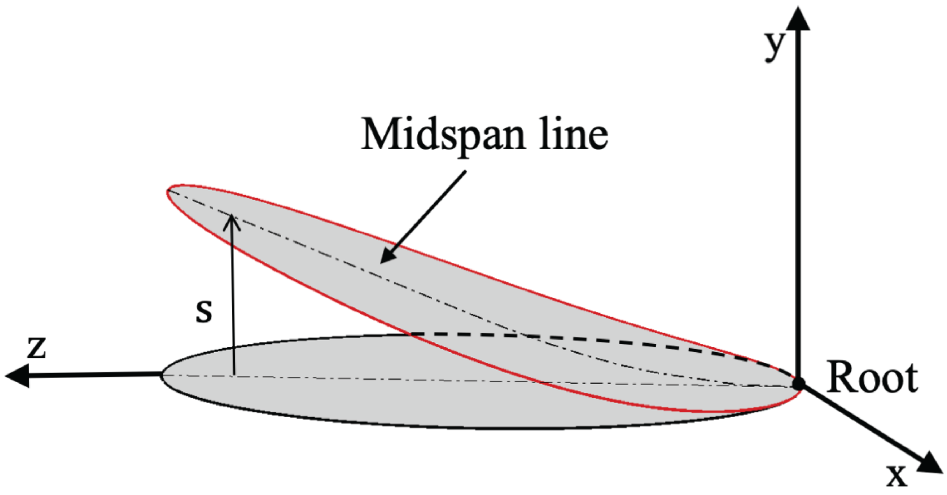

Figure 3.3: *The schematic of the flexible wing with spanwise bending*[1].

with limitation

$$|a_k| \leq 0.3, \quad |\varphi_n| \leq 90^\circ \quad \text{for} \quad k > 0 \tag{3.6}$$

3.1.3 Effective angle of attack

As shown in Fig.3.4, the heave velocity and the effective angle of attack will be affected after introducing the bending to the rigid wing. Since both X and R are used to probe the points in the undeformed Lagrangian frame, I used R to take the place of X for convenience. Then the effective angle of attack α_s for the flexible wing can be written as

$$\begin{aligned} \alpha_s &= \tan^{-1}\left(\frac{\dot{\theta}_x R + \dot{s}(R)}{U_\infty}\right) - \theta_{z'} \\ &= \tan^{-1}\left(\frac{-2\pi f R a_x \cos(2\pi f t) + \dot{s}(R)}{U_\infty}\right) - \theta_{z'} \end{aligned} \tag{3.7}$$

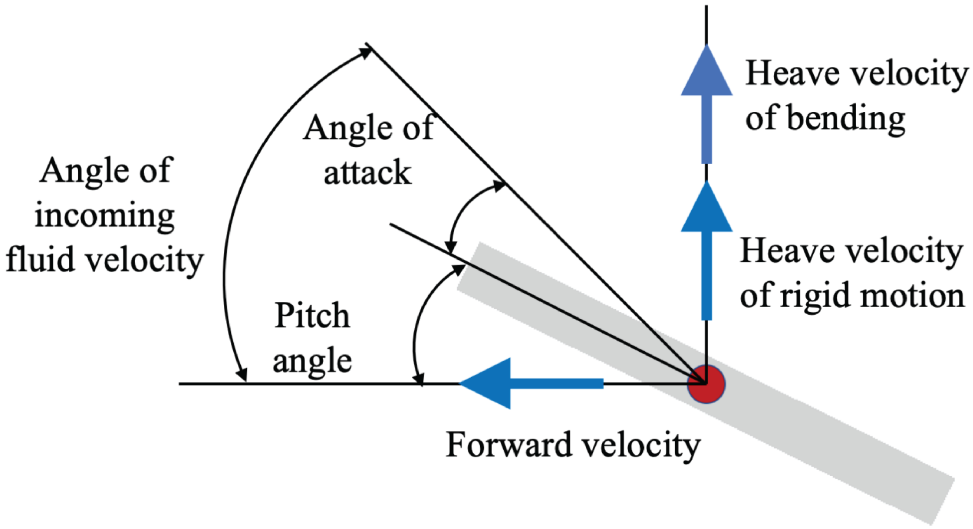

Figure 3.4: *Effective angle of attack for the flexible wing with spanwise bending*[1].

with the change rate of spanwise deformation at R

$$\dot{s}(R) = \sum_{k=1}^{n} a_k 2\pi f \psi_k(R) \cos(2\pi f t + \varphi_k) \tag{3.8}$$

When there is no bending ($s = 0$), $\alpha_s = \alpha_r$.

3.1.4 Effective rolling angle

In the optimization for the thrust of the rigid wing, it is found that the major improvement of thrust is contributed by the increased rolling amplitude[69]. As shown in Fig.3.5, the effective rolling angle θ' is defined by the instantaneous position of wing tip

$$\begin{aligned} \theta' &= \theta_x + \tan^{-1}\frac{s}{R} \\ &= \theta_x + \tan^{-1}\frac{\sum_{k=1}^{n} a_k \sin(2\pi f t + \varphi_k)\psi_k(R)}{R} \end{aligned} \tag{3.9}$$

For the wing tip, $R = 1$. Finally

$$\theta' = \theta_x + \tan^{-1} \sum_{k=1}^{n} a_k \sin(2\pi f t + \varphi_k)\psi_k(1) \tag{3.10}$$

Its amplitude a' can be used to describe the effects of bending on the rolling motion of the wing tip. For the rigid wing, that is $s = 0$, θ' will degenerate back to θ_x and a' is equal to a_x.

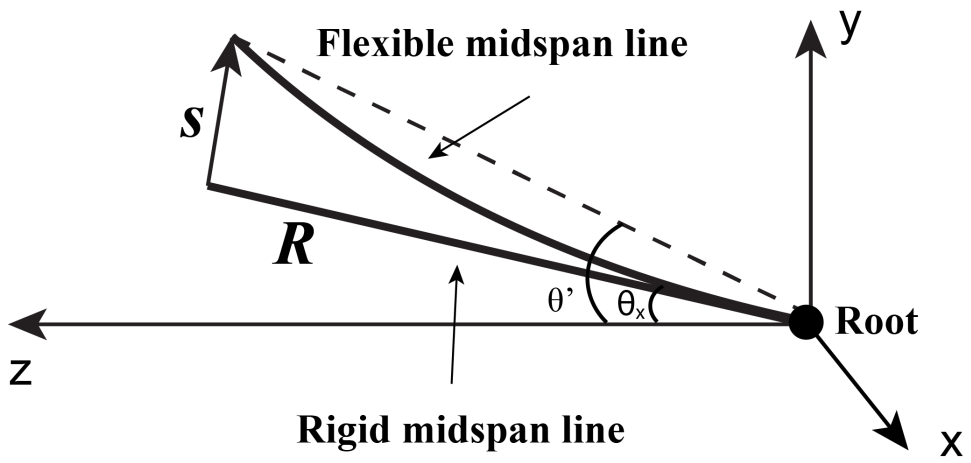

Figure 3.5: *Definition of effective rolling angle of the flexible wing.*

3.2 Optimization for thrust

In the beginning, I just used the first natural mode $\psi_1(X)$ to mimic the bending, which means the control in the optimization for thrust is

$$\phi_s = (a_1, \varphi_1) \tag{3.11}$$

Here we still choose the negative thrust coefficient as the cost function $\mathcal{J} = -C_T$. The thrust coefficient is defined the same as Eq. 2.5. As a supplement, the lift coefficient is defined as

$$C_L = \frac{1}{TD_0}\int_0^T \int_S \boldsymbol{\sigma}_2 \cdot \boldsymbol{n} \mathrm{d}s\mathrm{d}t \tag{3.12}$$

Where $\boldsymbol{\sigma}_2$ represents the stress contributing to the lift force along the y direction. However, the optimization of the lift force is not considered in this dissertation.

To present the effects of optimized deformation on thrust, the optimal control of pitching-rolling motion without deformation (Rigid_Opt) is set as the initial control of optimization for thrust of flexible wings, which can be also named as Flex_Int as shown in Table 3.1. The optimal control of the thrust optimization of flexible wings is named as Flex_Opt. After two main iterations in the adjoint-based optimization, the thrust coefficient is improved from 2.39 to 5.23, as shown in Table 3.1.

Table 3.1: *The control parameters and thrust coefficients in the intial and optimal cases.*

Case Name	a_x, a_z, φ_z	a_1, φ_1	C_T	
Rigid_Opt / Flex_Int	$45°, 35.9°, 122.6°$	0, 0°	2.39	Initial control of the optimization for thrust of flexible wings
Flex_Opt	$45°, 35.9°, 122.6°$	-0.3, 11.3°	5.23	Optimal control of the optimization for thrust of flexible wings

As shown in Fig.3.6 a), the spanwise bending can improve the lift-induced thrust largely at the cost of a slight increase of viscous-induced drag. The effects of the phase delay φ_1 between bending and rolling on the thrust coefficient C_T are studied by a parametric study shown in Fig.3.6 b). It shows that the gradient of thrust coefficient slows down near the

peak.

3.2.1 Effects on effective rolling angle

In the optimization of the rigid wing, it was found that the main improvement in thrust was caused by the increase in the rolling amplitude, and the magnitude of the angle of attack decreased due to the increase in the pitching amplitude[69]. Figure 3.7 shows that after introducing bending, the amplitude of rolling motion of the wing tip increases from 45° to 61.5°.

In Table 3.2, after introducing the spanwise bending, the effective rolling amplitude a' is increased from 45° to 61.5°, and C_T is improved from 2.39 to 5.23. In the Reference 1 case, whose wing is flexible and a' is the same as the Rigid_Opt case, its thrust coefficient is 12.6% smaller than that of the Rigid_Opt case. In the Reference 2 case, whose wing is rigid and a' is the same as the Flex_Opt case, its thrust coefficient is 6.9% larger than that of the Flex_Opt case. In the two comparisons mentioned above, the difference in thrust between the rigid and flexible wings, which have the same a', is caused by the change of the wing shape after the spanwise bending is introduced.

3.2.2 Effects on pressure distribution

The pressure distribution on the wing surfaces of the Rigid_Opt case and the Flex_Opt case is shown in Fig.3.8. Compared with the Rigid_Opt (or Flex_Int) case, in the Flex_Opt case, the high pressure occupies larger areas on the wing surfaces, and the pressure difference is also increased after optimization. The enhanced pressure difference at the wing tip matches

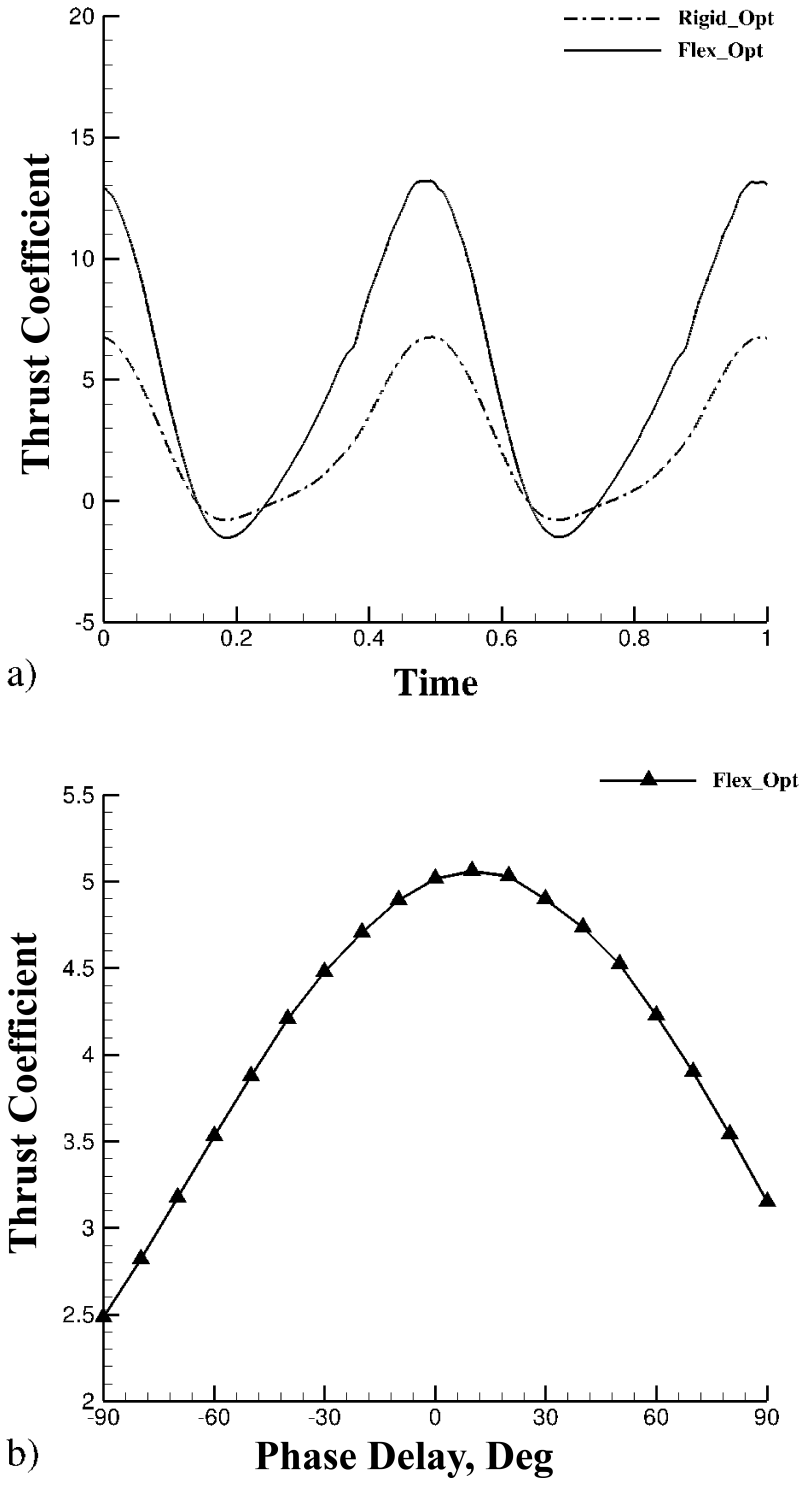

Figure 3.6: *a) The comparison of the instantaneous thrust coefficient history, b) the effects of the phase delay φ_1 on the thrust coefficient in the Flex_Opt case*[1].

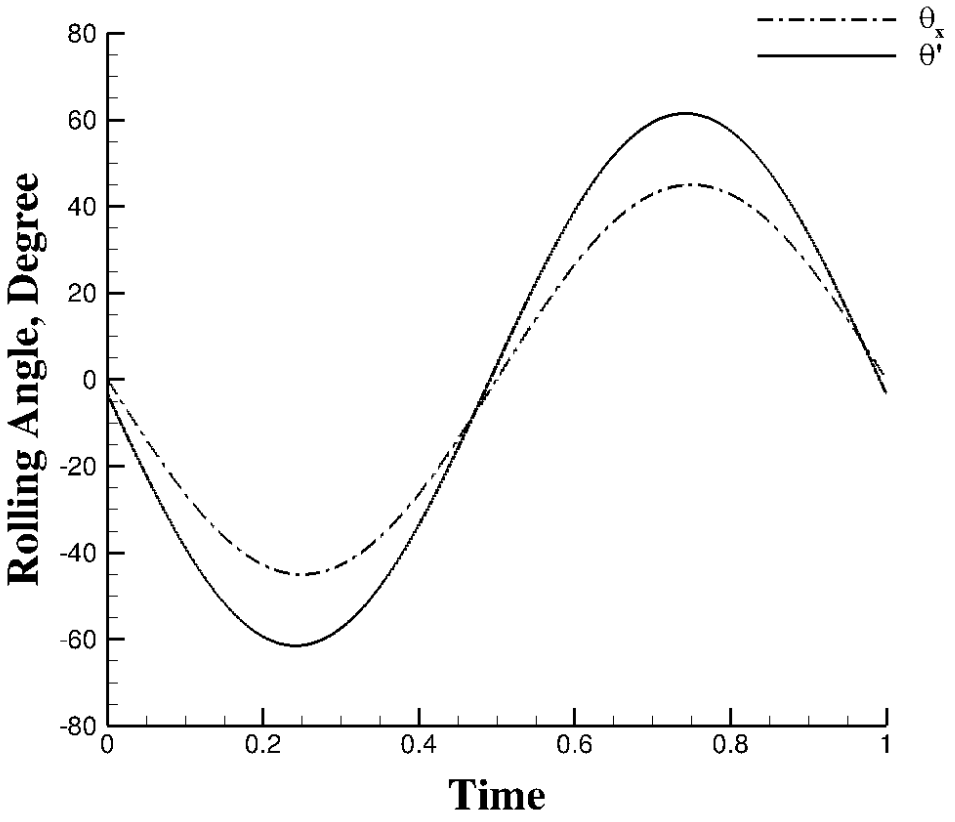

Figure 3.7: *The effective rolling angles in the Rigid_Opt case (dashed line) and in the Flex_Opt case (solid line)*

Table 3.2: *The effective rolling amplitudes and thrust coefficients in different cases.*

Case Name	a_x, a_z, φ_z	a_s, φ_s	a'	C_T	
Rigid_Opt	$45°, 35.9°, 122.6°$	$0.0, 0.0°$	$45°$	2.39	Rigid wing with optimized motion
Reference 1	$28.5°, 35.9°, 122.6°$	$-0.3, 11.3°$	$45°$	2.09	Flexible wing with the same a' as the Rigid_Opt case
Flex_Opt	$45°, 35.9°, 122.6°$	-0.3, $11.3°$	$61.5°$	5.23	Flexible wing with optimized deformation
Reference 2	$61.5°, 35.9°, 122.6°$	0.0, $0.0°$	$61.5°$	5.59	Rigid wing with the same a' as the Flex_Opt case

with the improvement of rolling amplitude.

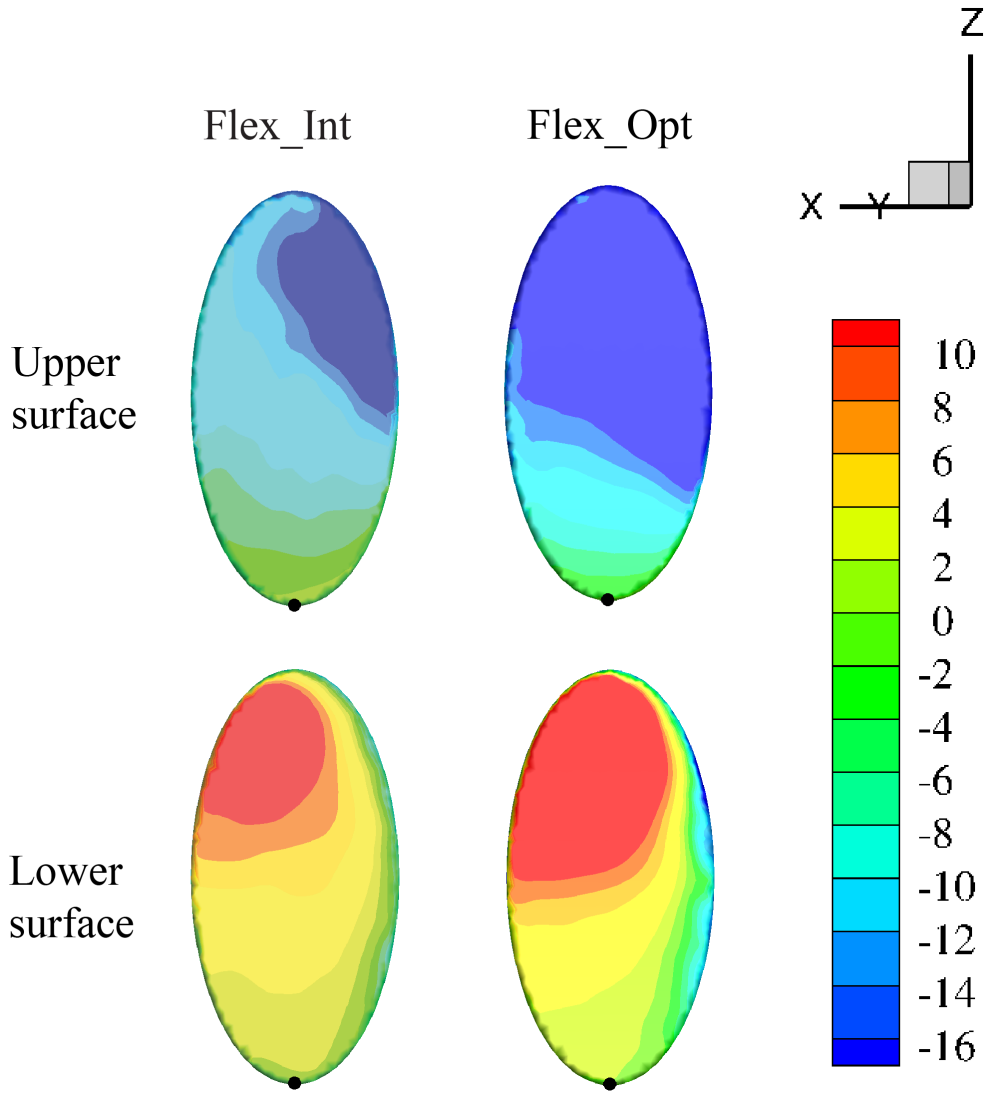

Figure 3.8: *The pressure distribution of the Flex_Int (Rigid_Opt) and Flex_Opt cases when* $t/T = 0$[1].

3.2.3 Effects on effective angle of attack

The effects of introducing the spanwise bending on the effective angle of attack are shown in Fig.3.9. The spanwise bending slightly increased the magnitude of angle of attack.

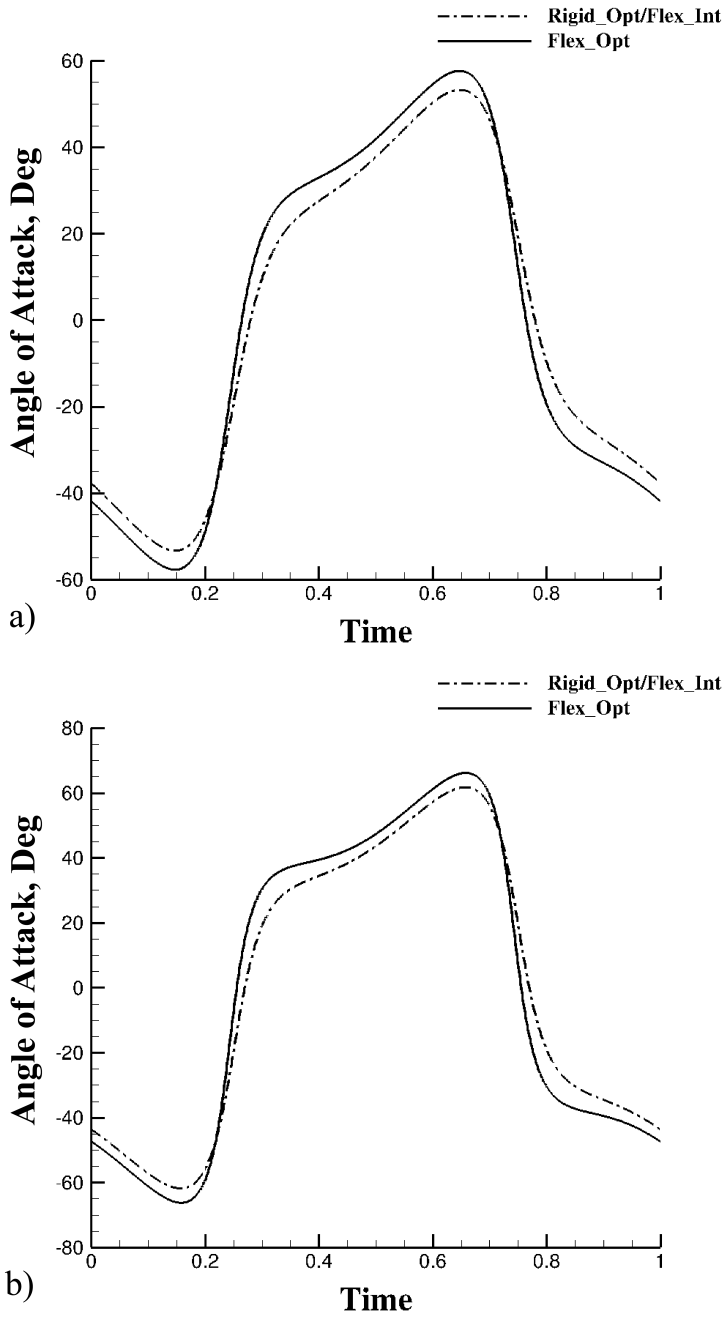

Figure 3.9: *Comparison of a) the angle of attack at 50% span, and b) the angle of attack at 70% span*[1].

3.2.4 Effects on wake topology

The wake topology of the Rigid_Opt (or Flex_Int) case and the Flex_Opt case at $t/T = 0$ is compared in Fig.3.10. The spanwise bending enhances the strength of the vortex street and

reduces the wake deflection.

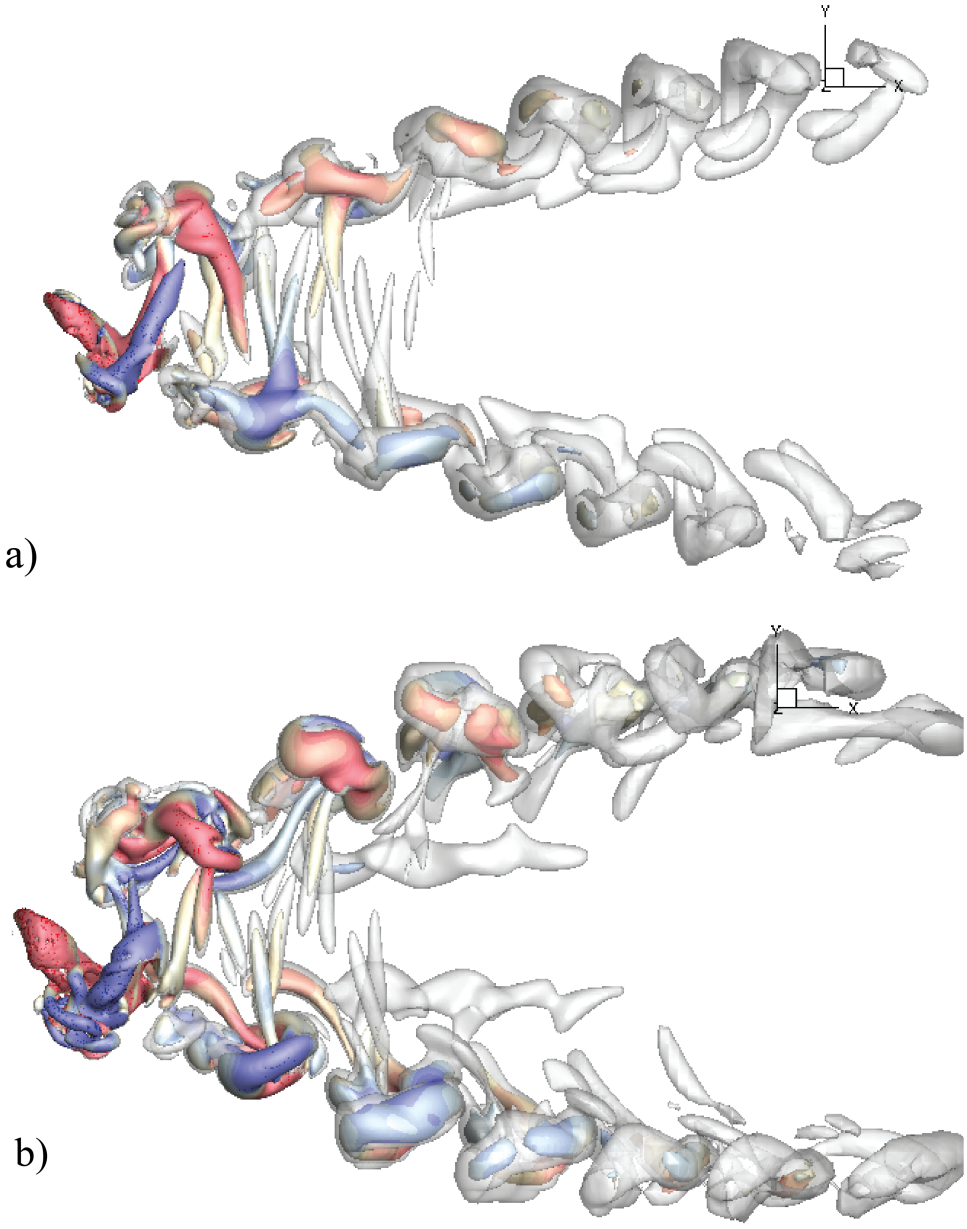

Figure 3.10: *Wake topology of the plate with a) initial control and b) optimal control at* $t/T = 0$. *The isosurface contours are color coded by the streamwise vorticity* ω_x [1].

3.2.5 Effects of wing shape on thrust

The second natural mode is utilized here to extend the design space of the wing shape. To investigate the effects of wing shape on thrust, we introduced the parameter γ in the spanwise deformation s to confirm the instantaneous position of the wing tip would not be changed. In this case, the deformation s can be defined as

$$s = a_1 \sin(2\pi f t + \varphi_1)(\gamma\psi_1 + (1-\gamma)\psi_2) \tag{3.13}$$

when $\gamma = 1$, the deformation is modeled only by ψ_1, and when $\gamma = 0$, the deformation will be modeled only by ψ_2.

From Fig.3.11, when $\gamma < 1$, the thrust is less than the thrust of the Flex_Opt case. The wing shapes changing with γ are shown in Fig.3.12. In Fig.3.13, compared with the Flex_Opt case ($\gamma = 1$), the high pressure occupies larger areas on the wing surfaces, and the pressure difference is also increased in the $\gamma = 1.25$ case.

3.3 Twisting modeling

The twisting is modeled by following Manta's twisting pattern, whose main characteristic is that the front and rear parts of the wings are twisted in opposite directions[84], as shown in Fig.3.14.

The linear twisting is controlled by

$$\chi_{nn} = \frac{nn - 50}{50}\zeta(t) \tag{3.14}$$

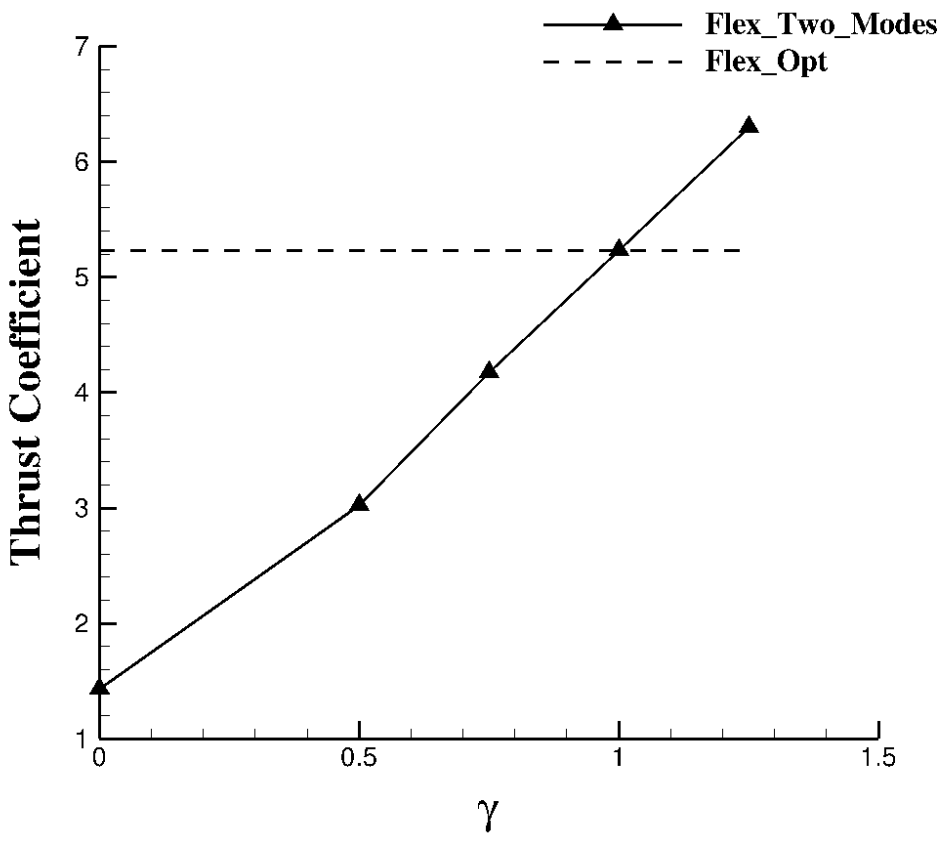

Figure 3.11: *Thrust coefficient changes with different* γ

$$\zeta(t) = a_t \sin(2\pi f t + \varphi_t) \tag{3.15}$$

where *nn* stands for the portion of span length from root and changes from 0 to 100 (0 stands for root and 100 stands for the tip), $\zeta(t)$ is the temporal twisting angle.

3.3.1 Effective angle of attack

As shown in Fig.3.15, the effective angle of attack α_t of the twisting wing is changed directly by introducing the twisting angle.

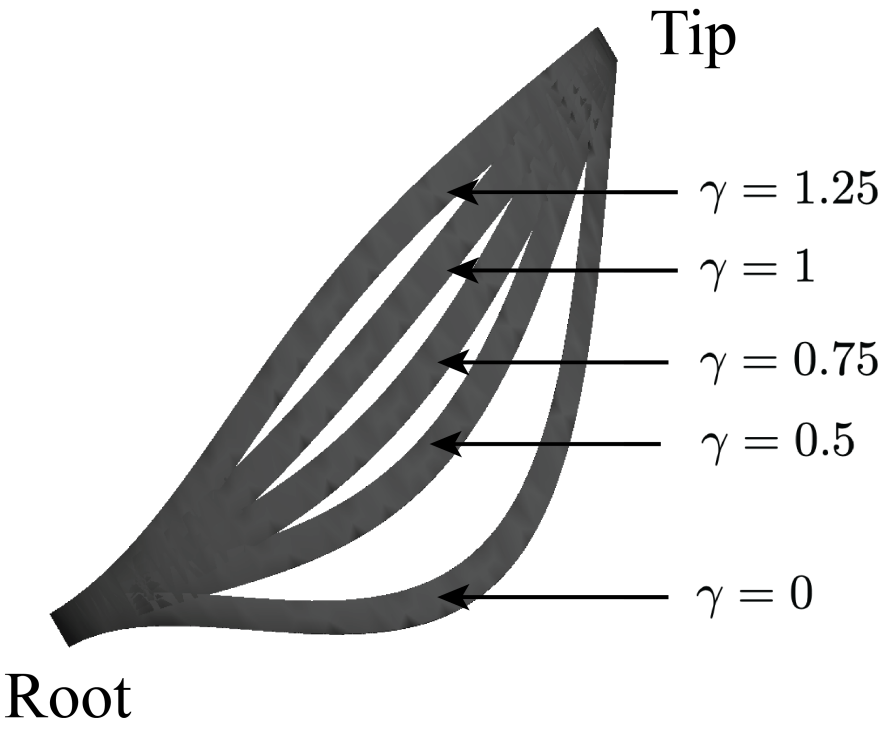

Figure 3.12: *Wing shapes with different γ when $t/T = 0.2$*

The effective angle of attack α_t would be

$$\alpha_t = \tan^{-1}\left(\frac{-2\pi f a_x R\cos(2\pi f t)}{U_\infty}\right) - (\theta_{z'}(t) + \chi_{nn}(t)) \tag{3.16}$$

where $\alpha_t(t)$ stands for the effective angle of attack of the flexible wing with linear twisting only, and R means the span location. In Eq. 3.16, the item of $\theta_{z'}(t) + \chi_{nn}(t)$ is also defined as the effective pitching angle $\theta_{z'}^{'}$.

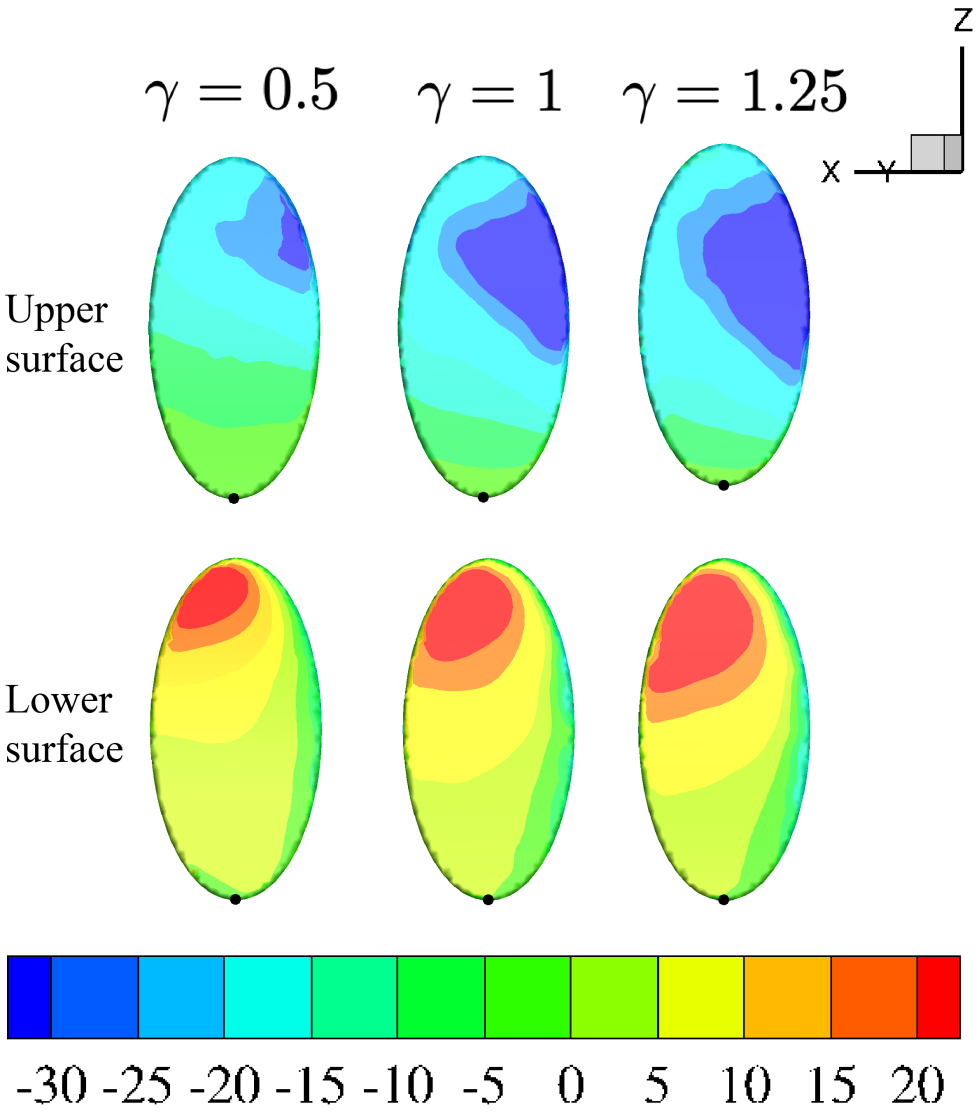

Figure 3.13: *The pressure distribution on surfaces with different* γ.

3.4 Optimization for efficiency

The control in the optimization for efficiency is defined as

$$\phi = (a_t, \varphi_t) \tag{3.17}$$

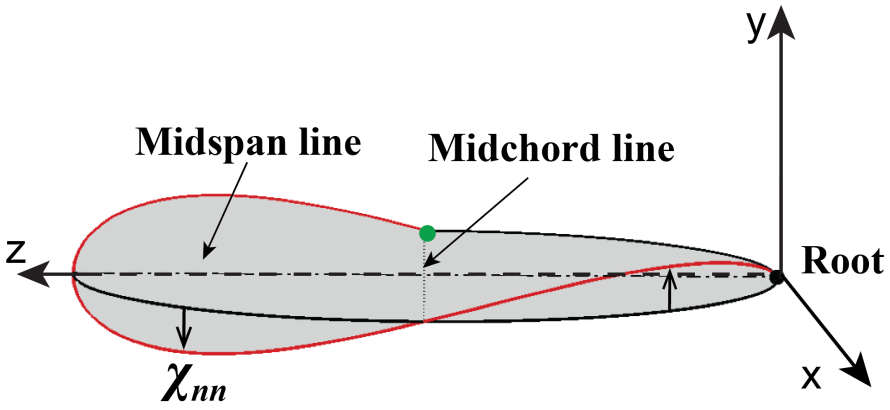

Figure 3.14: *Schematic of the flexible wing with linear twisting*[1].

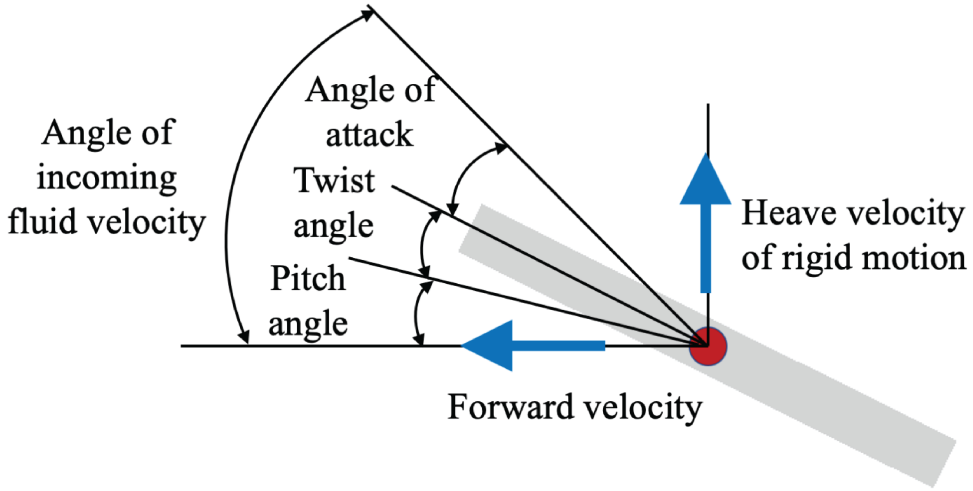

Figure 3.15: *Effective angle of attack for the flexible wing with twisting*[1].

with limitation

$$|a_t| \leq 45^\circ, \quad |\varphi_t| \leq 180^\circ \tag{3.18}$$

The adjoint-based approach is one of the local optimization techniques. Since the efficiency of the Rigid_Opt case is one of the optimal local results, if it is selected as the initial control, the optimization will get stuck in place. Another initial control (Twist_Int) is randomly chosen to avoid this local optimization trap. As shown in Table 3.3, the efficiency

in the Twist_Int case is very close to that in the Rigid_Opt case. After the optimization of the twisting control, the efficiency η is improved from 0.14 to 0.17. The comparison of the three cases indicates that the improvement of aerodynamic performance requires not only the introduction of physical mechanisms but also the coordination of appropriate control parameters.

Table 3.3: *The control parameters and efficiencies in different cases.*

Case Name	a_x, a_z, φ_z	a_t, φ_t	η	
Rigid_Opt	$45°, 35.9°, 122.6°$	$0°$, $0°$	0.13	One of the local optima
Twist_Int	$45°, 35.9°, 122.6°$	$10°$, $-60°$	0.14	Initial control of the optimization for efficiency of flexible wings
Twist_Opt	$45°, 35.9°, 122.6°$	$40°$, $-95.5°$	0.17	Optimal control of the optimization for efficiency of flexible wings

As shown in Fig.3.16 b), in the Twist_Int case, the output power for propulsion P_0 is the same as that of the Rigid_Opt case. However, its input power (or total consumed power) P_c is slightly smaller as shown in Fig.3.16 a), which causes the efficiency of the Twist_Int case is slightly larger than the efficiency of the Rigid_Opt case. After optimization, in the Twist_Opt case, the output power for propulsion P_0 is reduced, but the input power P_c decreases with a larger magnitude, which leads to an improvement of η from 0.14 to 0.17. Compared with the rigid wings, the efficiency η of the flexible wings (twisting only) is improved by reducing the total consumed energy while maintaining similar output energy for propulsion.

The effects of the phase delay between twisting and rolling φ_t on the efficiency η are studied by a parametric study shown in Fig.3.17. In the Twist_Opt case, as the phase delay φ_t is between $-180°$ and $0°$, its twisting pattern is classified in the delayed deformation

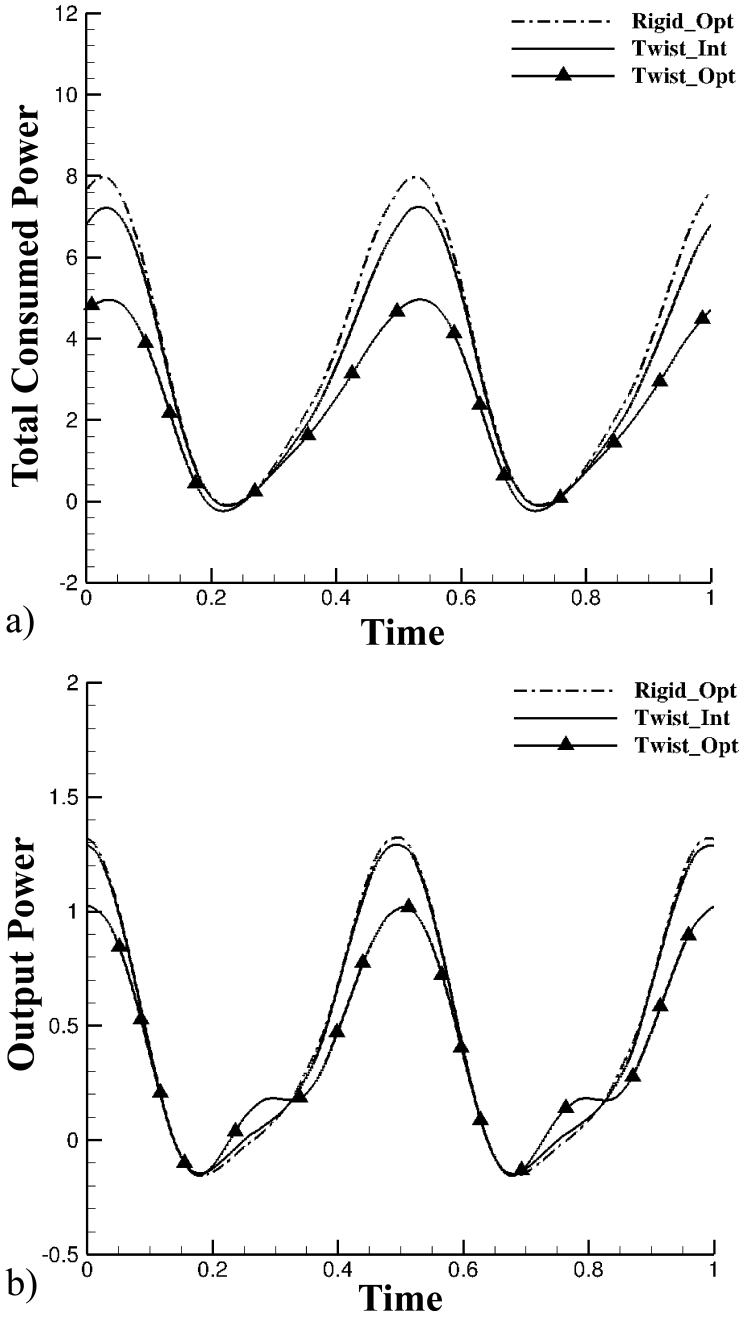

Figure 3.16: *The comparison of the instantaneous history of a) total consumed power P_c, and b) output power P_0 of different cases*[1].

pattern[85]. When φ_t is around 95.5°, the difference between the efficiencies is very small.

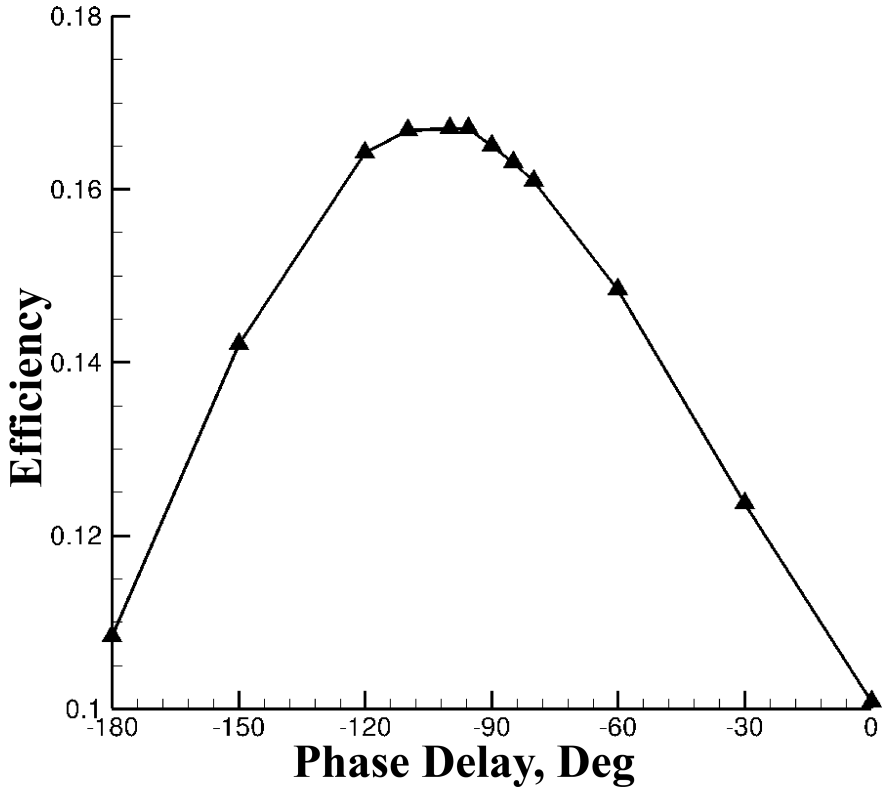

Figure 3.17: *The instantaneous efficiency changes with the phase delay φ_t in the Twist_Opt case*[1].

3.4.1 Effects on pressure distribution

The effects of the delayed pattern twisting are studied in this section. In Fig.3.18, when $t/T = 0$, the wings are on the downstroke. The magnitude and distribution of pressure on the wing's surface in the Rigid_Opt case and the Twist_Int case are very similar, which corresponds to the similar efficiencies of the two cases. However, in the Twist_Opt case, the magnitude of pressure at the wingtip is largely reduced, and the pressure difference is more concentrated on the leading edge. Thus the wing can flap by consuming less energy, as shown in Fig.3.16 a).

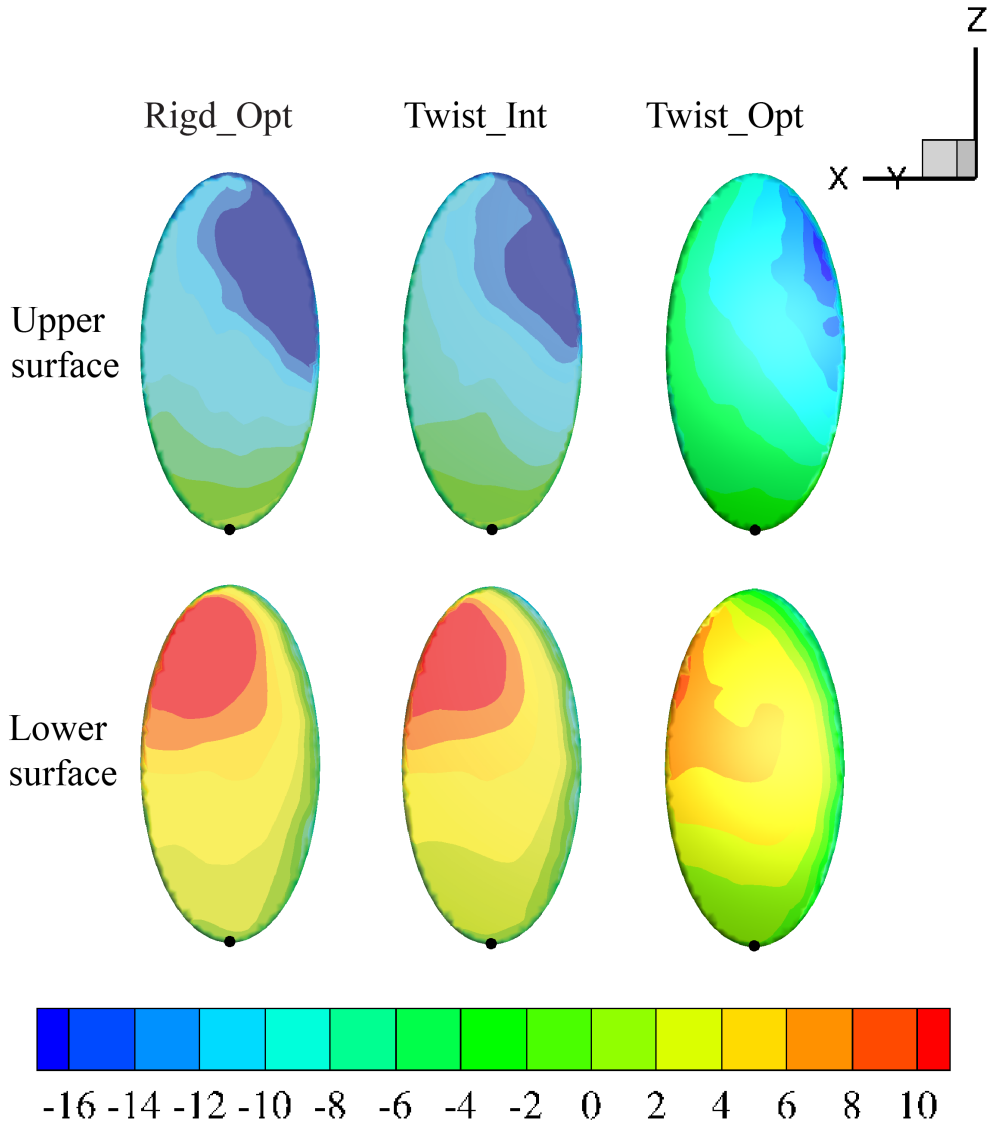

Figure 3.18: *The pressure distribution of the Rigid_Opt, Twist_Int and Twist_Opt cases when* $t/T = 0$[1].

3.4.2 Effects on effective angle of attack

By Eq. (3.16), a larger effective pitching angle $\theta'_{z'}$ will decrease the value of the effective angle of attack α_t. In Fig.3.19, the effective angles of attack of the Rigid_Opt and Twist_Int are very close. However, the magnitude of the angle of attack a_t of the Twist_Opt case is smaller than that of the other two cases, which corresponds to the model in Fig.3.21, the

lower total energy consumption P_0 in Fig.3.16, and larger efficiency η of the Twist_Opt case in Table 3.3.

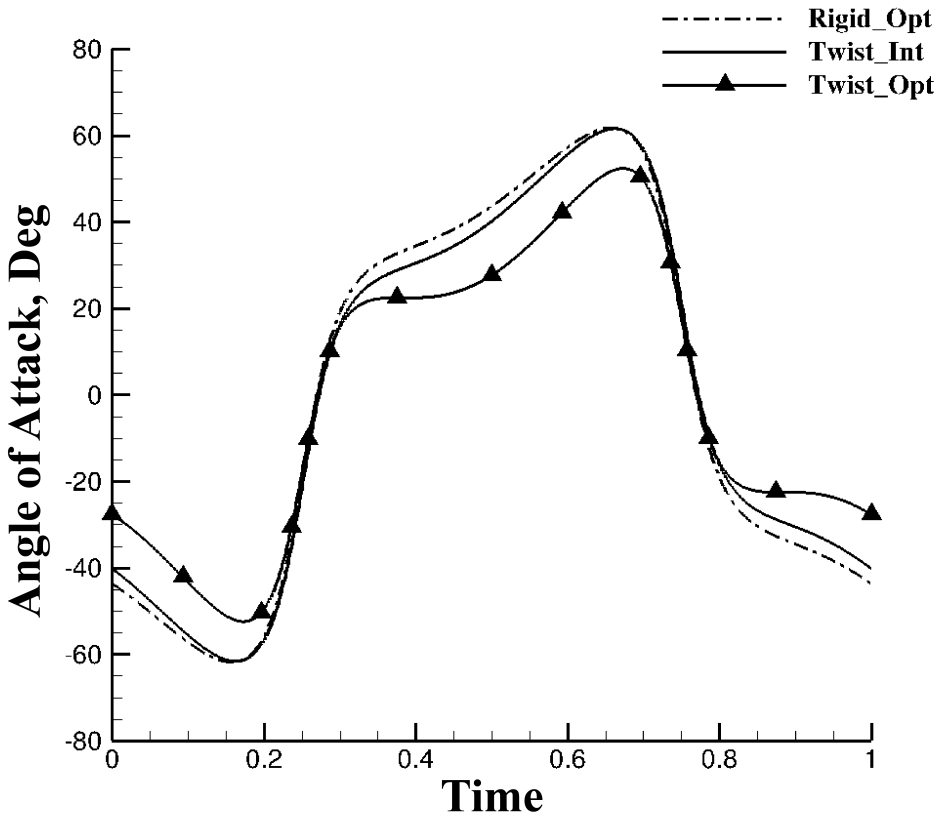

Figure 3.19: *The comparison of the instantaneous angle of attack at 70% span in Rigid_Opt, Twist_Int, and Twist_Opt cases*[1].

The comparison of the instantaneous angle of attack at 70% span of Rigid_Opt, Rigid_Eff, and Twist_Opt cases is shown in Fig.3.20. We didn't compare the angles of attack at 50% span because the twisting angle at this place is 0° by definition. At 70% span, the magnitude of the angle of attack in the Twist_Opt case is in the middle of the magnitudes in the Rigid_Opt and the Rigid_Eff cases. When $t/T = 0, 0.5, 1$, the angle of attack in the Twist_Opt case is almost the same as the angle of attack in the Rigid_Eff case.

The effects of twisting on the effective angle of attack are illustrated in Fig.3.21. After

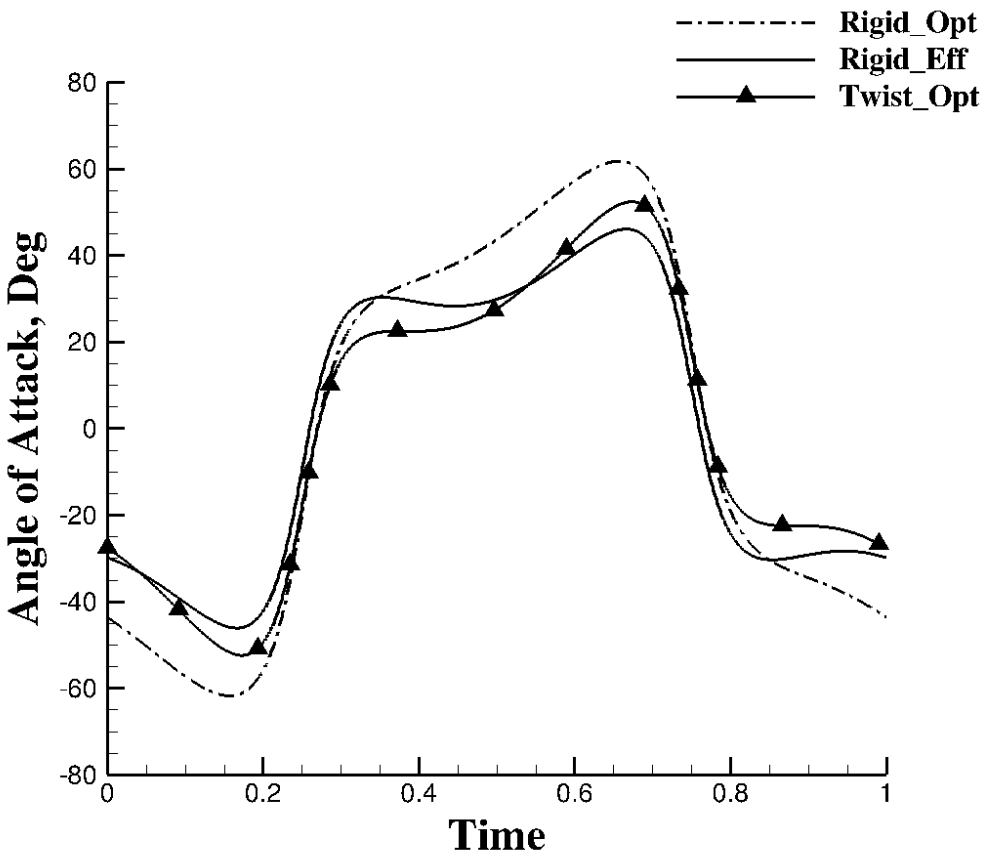

Figure 3.20: *The comparison of the instantaneous angles of attack at 70% span in Rigid_Opt, Rigid_Eff, and Twist_Opt cases.*

introducing the twisting to the rigid wing, the thrust is maintained or slightly reduced with a smaller total force by increasing the effective pitching angle.

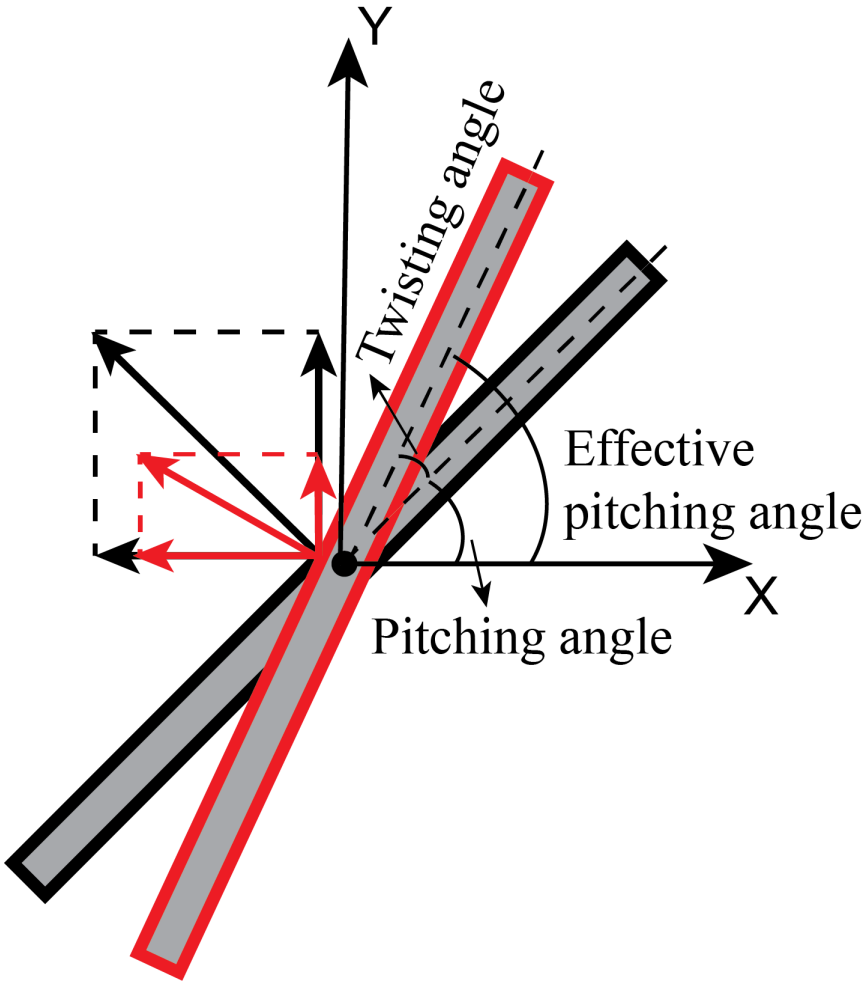

Figure 3.21: *The schematic of the physical model about the effects of twisting on aerodynamic force projection*[1].

Chapter 4

Vorticity transfer in a LEV due to controlled bending

In nature, many flyers and swimmers can routinely deform theirs wings/fins to control the formation and growth of the LEV that forms on the suction side during maneuvering at a high angle of attack to enhance the force generation or efficiency. In this chapter, the effects of the bending on the formation and growth of vortex on a flat plate airfoil, which is accelerated from rest to a Reynolds number of 2400 and held at an angle of attack of 30°, are studied. The bending of the plate is controlled to achieve a bending ratio of 0.65 and a maximum bending angle of 30° along span direction. The numerical results show that the spanwise bending would delay the growth of LEV compared with the non-bending case. At the same time, the circulation from numerical simulation are compared with the experimental and analytic solution.

4.1 Vorticity transfer

The vorticity equation is used to describe the evolution of the vorticity ω of a particle of fluid.

The incompressible Navier-Stokes equations are

$$\frac{\partial \boldsymbol{u}}{\partial t} + \boldsymbol{u} \cdot \nabla \boldsymbol{u} = -\nabla p + \frac{1}{Re} \nabla^2 \boldsymbol{u} \tag{4.1}$$

Then taking the curl of both sides of the Navier-Stokes equations,

$$\nabla \times (\frac{\partial \boldsymbol{u}}{\partial t} + \boldsymbol{u} \cdot \nabla \boldsymbol{u}) = \nabla \times (-\nabla p + \frac{1}{Re} \nabla^2 \boldsymbol{u}) \tag{4.2}$$

The first term on the left side becomes

$$\nabla \times \frac{\partial \boldsymbol{u}}{\partial t} = \frac{\partial}{\partial t} (\nabla \times \boldsymbol{u}) = \frac{\partial \boldsymbol{\omega}}{\partial t} \tag{4.3}$$

The inertial term $\boldsymbol{u} \cdot \nabla \boldsymbol{u}$ can be rewritten as

$$\boldsymbol{u} \cdot \nabla \boldsymbol{u} = \frac{1}{2} \nabla (\boldsymbol{u} \cdot \boldsymbol{u}) - \boldsymbol{u} \times (\nabla \times \boldsymbol{u}) = \nabla (\frac{u^2}{2}) - \boldsymbol{u} \times \boldsymbol{\omega} \tag{4.4}$$

and then the second term on the left side can be rewritten as

$$\begin{aligned} \nabla \times (\boldsymbol{u} \cdot \nabla \boldsymbol{u}) &= \nabla \times \nabla (\frac{u^2}{2}) - \nabla \times (\boldsymbol{u} \times \boldsymbol{\omega}) = \nabla \times (\boldsymbol{\omega} \times \boldsymbol{u}) \\ &= (\boldsymbol{u} \cdot \nabla) \boldsymbol{\omega} - (\boldsymbol{\omega} \cdot \nabla) \boldsymbol{u} + \boldsymbol{\omega} (\nabla \cdot \boldsymbol{u}) + \boldsymbol{u} (\nabla \cdot \boldsymbol{\omega}) \end{aligned} \tag{4.5}$$

Since $\nabla \cdot \boldsymbol{u} = 0$, and $\nabla \cdot (\nabla \times \boldsymbol{u}) = 0$

$$\nabla \times (\boldsymbol{u} \cdot \nabla \boldsymbol{u}) = (\boldsymbol{u} \cdot \nabla)\boldsymbol{\omega} - (\boldsymbol{\omega} \cdot \nabla)\boldsymbol{u} \tag{4.6}$$

At the right side, the pressure term vanishes since $\nabla \times \nabla \cdot scalar = 0$

$$\nabla \times (-\nabla p + \frac{1}{Re}\nabla^2 \boldsymbol{u}) = \frac{1}{Re}\nabla^2 \boldsymbol{\omega} \tag{4.7}$$

Putting everything together, we obtain the vorticity equation

$$\frac{\partial \boldsymbol{\omega}}{\partial t} + (\boldsymbol{u} \cdot \nabla \boldsymbol{\omega}) = (\boldsymbol{\omega} \cdot \nabla)\boldsymbol{u} + \nu \nabla^2 \boldsymbol{\omega} \tag{4.8}$$

where $\boldsymbol{u} = [u, v, w]$ is the velocity field and $\boldsymbol{\omega} = [\omega_x, \omega_y, \omega_z]$ is the vorticity vector.

We focused on the spanwise (ω_z) component of the vorticity transport equation, which is given by the following equation (neglecting the effects of viscous diffusion):

$$\frac{\partial \omega_z}{\partial t} + u\frac{\partial \omega_z}{\partial x} + v\frac{\partial \omega_z}{\partial y} + w\frac{\partial \omega_z}{\partial z} = \omega_x \frac{\partial w}{\partial x} + \omega_y \frac{\partial w}{\partial y} + \omega_z \frac{\partial w}{\partial z} \tag{4.9}$$

where $\frac{\partial \omega_z}{\partial t}$ stands for the temporal rate of change of ω_z; $u\frac{\partial \omega_z}{\partial x}$, $v\frac{\partial \omega_z}{\partial y}$ and $w\frac{\partial \omega_z}{\partial z}$ represent the convection of ω_z in the streamwise (x), wall-normal (y) and spanwise (z) directions, respectively; $\omega_x \frac{\partial w}{\partial x}$, and $\omega_y \frac{\partial w}{\partial y}$ denote the vortex tilting along the streamwise (x), and the wall-normal (y) directions and $\omega_z \frac{\partial w}{\partial z}$ denotes vortex stretching.

4.2 Plate model and kinematics

The experimental prototype, whose chord 5 cm, span 15 cm (aspect ratio 3), and thickness 4 mm, is shown in Fig.4.1 a). This flat plate was 3D printed, and two prebent rods were inserted into the plate through two curved grooves to mimic the desired curvature of the tip as shown in Fig.4.1 b). The bending ratio (BR) is defined as the ratio of the plate's bent length to the total span, and the bending angle is defined as the angle between the horizontal and the tip-tangent. Finally the plate would achieve a bending ratio of 0.65 and a maximum bending angle of 30°, as shown in Fig.4.1 c).

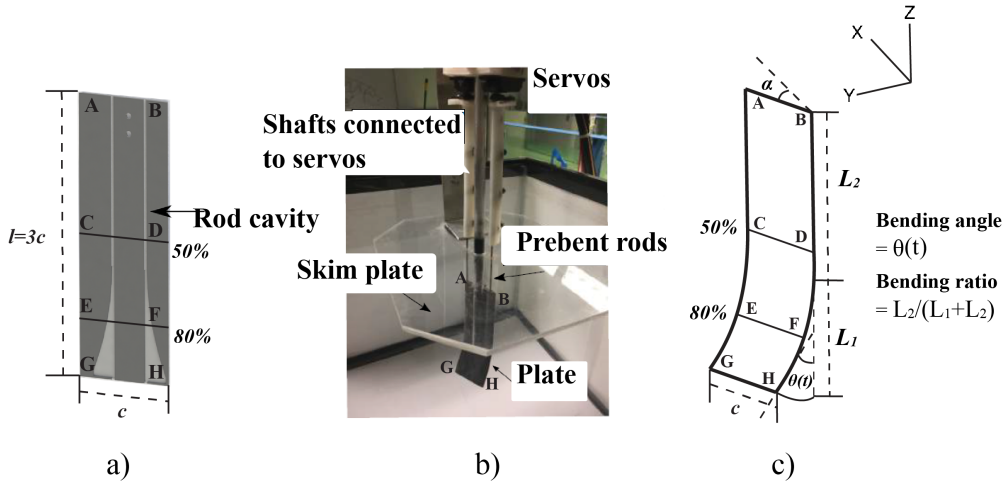

Figure 4.1: *The construction of the morphing plate: a) grooves inside a 3D printed plate for holding prebent rods; b) the plate-rod assembly is connected to servos, which bend the plate along the span; c) the definition of bending angle and bending ratio. The tips are marked by AB and GH; the 50% span and the 80% span are, respectively, marked by CD and EF*[2].

The flat-plate wing was held at a constant angle of attack (α) of 30°. The wing was started from rest with an acceleration of 0.1 m/s^2 and it reached the final towing velocity 0.05 m/s in 0.5 s (t_{ac}). The Reynolds number (Re), based on the chord and this final towing velocity, was 2400. As the wing was accelerated from rest, the wing was bent dynamically for 1 s away from the towing direction. The nondimensional time t^* was calculated by dividing

time (t) with t_{ac}. Hence, bending was completed at $t^* = 2$, while the plate completed acceleration at $t^* = 1$ (Fig. 4.2).

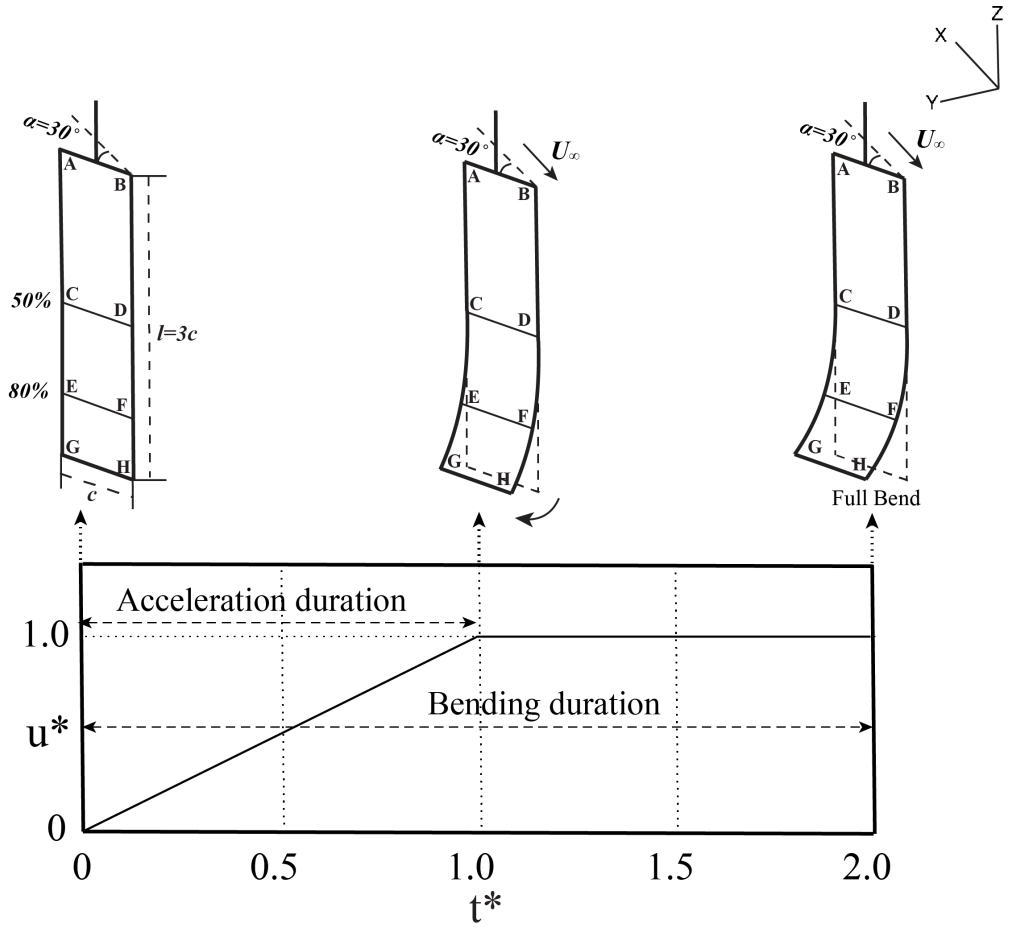

Figure 4.2: *The kinematics of the plate motion. The plate is accelerated for $t^* = 1$ and the bending is completed at $t^* = 2$. u^* is obtained by normalizing u (velocity) by U_∞ (0.05 m/s)[2].*

The chord length (c) and the free stream speed (U_∞) are chosen as the characteristic length and the characteristic speed, respectively. In the simulation, the Reynolds number is defined as $Re = \frac{U_\infty c}{\nu}$ based on the free stream velocity and the chordwise length c. All the non-dimensional values of the experimental parameters used in the simulation are shown in Table 4.1.

Table 4.1: *Non-dimensional parameter space.*

Variable	Dimensional Value	Nondimensional Value
Plate chord (c)	0.05 m	1
Plate span (l)	0.15 m	3
Accelerating time (t_{ac})	0.5 s	0.5
Acceleration(a_1)	0.1 m/s^2	2
Free stream speed (U_∞)	0.05 m/s	1
Angle of attack (α)	30°	
Aspect ratio (AR)		3
Bending ratio (BR)		0.65
Reynolds number (Re)		2400

4.3 Computational configuration

The dimensions of the flat plate in our simulation are shown in Fig.4.3 b) with a chord length of c, a span length of $l = 3c$, and a thickness of $h = 0.08c$. The angle of attack is 30°. The size of the computational domain is $12c \times 4c \times 5c$, and the mesh along the x direction is stretched to improve the computation efficiency in which the length of the uniform part is $5.8c$. A corresponding stretched Cartesian mesh is used for an overall Eulerian description of the combined fluid and the solid domain with a size of $600 \times 400 \times 500$, as shown in Fig.4.3 a). The grid is clustered near the solid region with a minimum size of $\Delta x = \Delta y = \Delta z = 0.01$.

4.4 Grid independence

To verify the effects of grid size on our simulation results, we designed a similar case in which the flat plate is moving with constant velocity U_∞, and the Reynolds number is still $Re = 2400$. Three different grid sizes of $\Delta_1 = 0.02$, $\Delta_2 = 0.01$ and $\Delta_3 = 0.0075$ are tested. In Fig.4.4, we found that $\Delta_1 = 0.02$ is too coarse to capture the right vortex structures, while $\Delta_2 = 0.01$ and $\Delta_3 = 0.0075$ are good enough to present the LEV structures at both

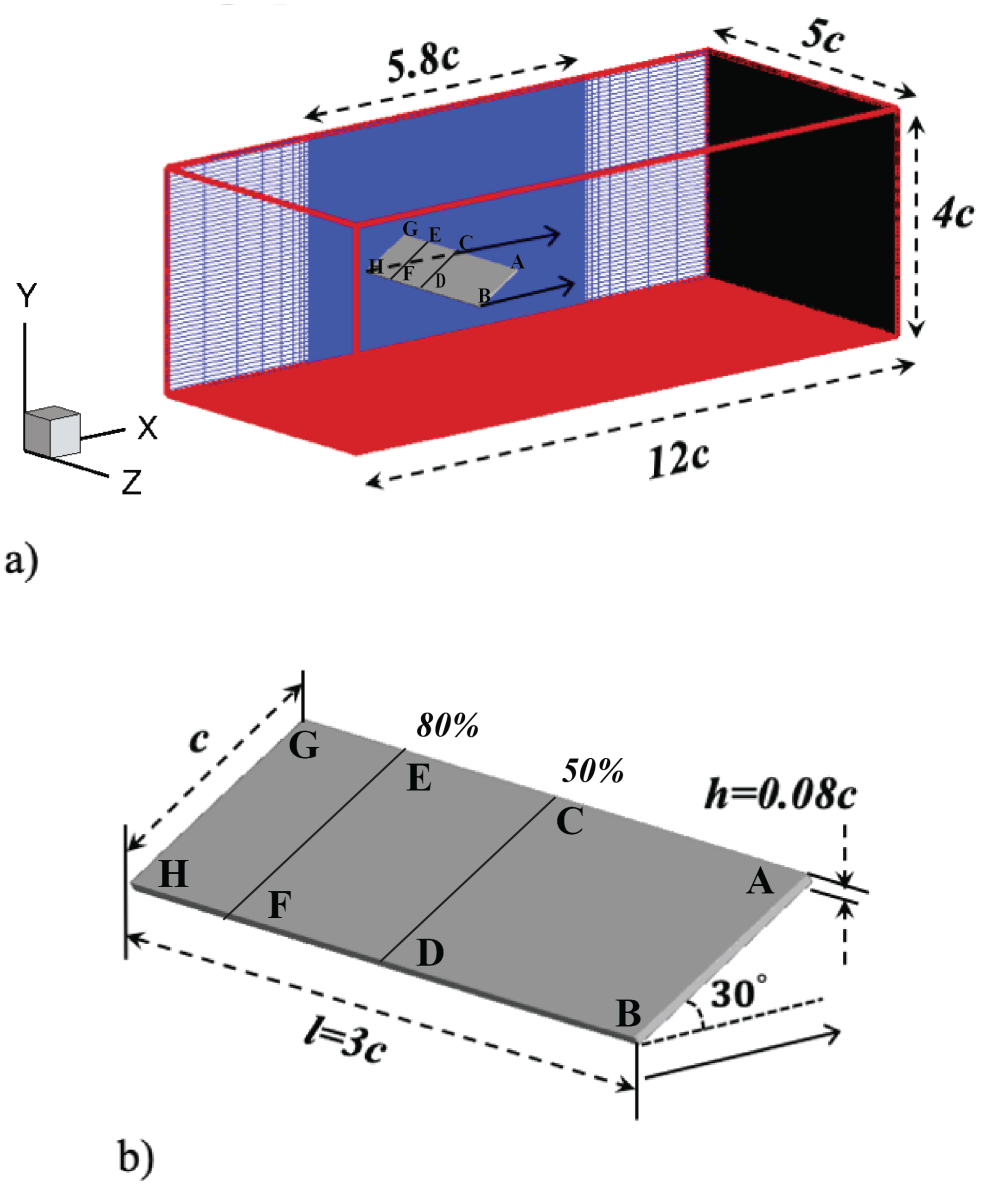

Figure 4.3: *Schematics of a) the computational domain and Cartesian mesh employed in the current simulation. The mesh along the x direction is stretched and the length of the uniform part is 5.8c; b) the dimensions of the plate used in the current study. The solid arrow stands for the moving direction of the plate, which is along the x-axis direction*[2].

50% span and 80% span. Besides the qualitative description, in Fig.4.5, which describes the histories of the aerodynamic forces, both $\Delta_2 = 0.01$ and $\Delta_3 = 0.0075$ get converged. Taking the computational efficiency into consideration, $\Delta_2 = 0.01$ is an appropriate choice.

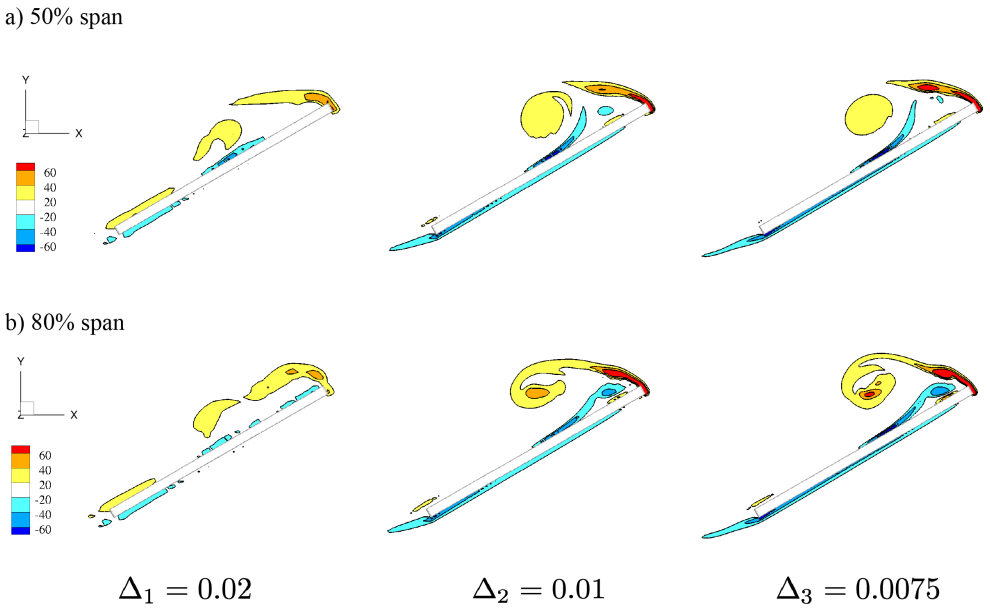

Figure 4.4: *a) The LEV on the midspan (50% span) of the plate with different grid sizes. b) The LEV on 80% span of the plate with different grid sizes.*

4.5 The growth of the LEV during bending

4.5.1 Analytical model

The analytical model was originally developed by Wong et al.[3] to analyze the growth of LEV on a rigid plate. This model is modified by taking the effects of the bending velocity of the leading edge on the effective leading-edge velocity into consideration. The wake vorticity and bound vortex of the flat plate are disregarded, which is suggested by Ford and Babinsky[31].

As illustrated by Fig.4.6, the LEV is represented by a semi-cylindrical region, which gradually grows in size due to the mass flow brought in by the shear layer with fixed thickness d. The outer shear layer velocity $u(d,t)$ is assumed to be the sum of three separate velocity components, namely,

$$u(d,t) = u_b + u_i + u_k \tag{4.10}$$

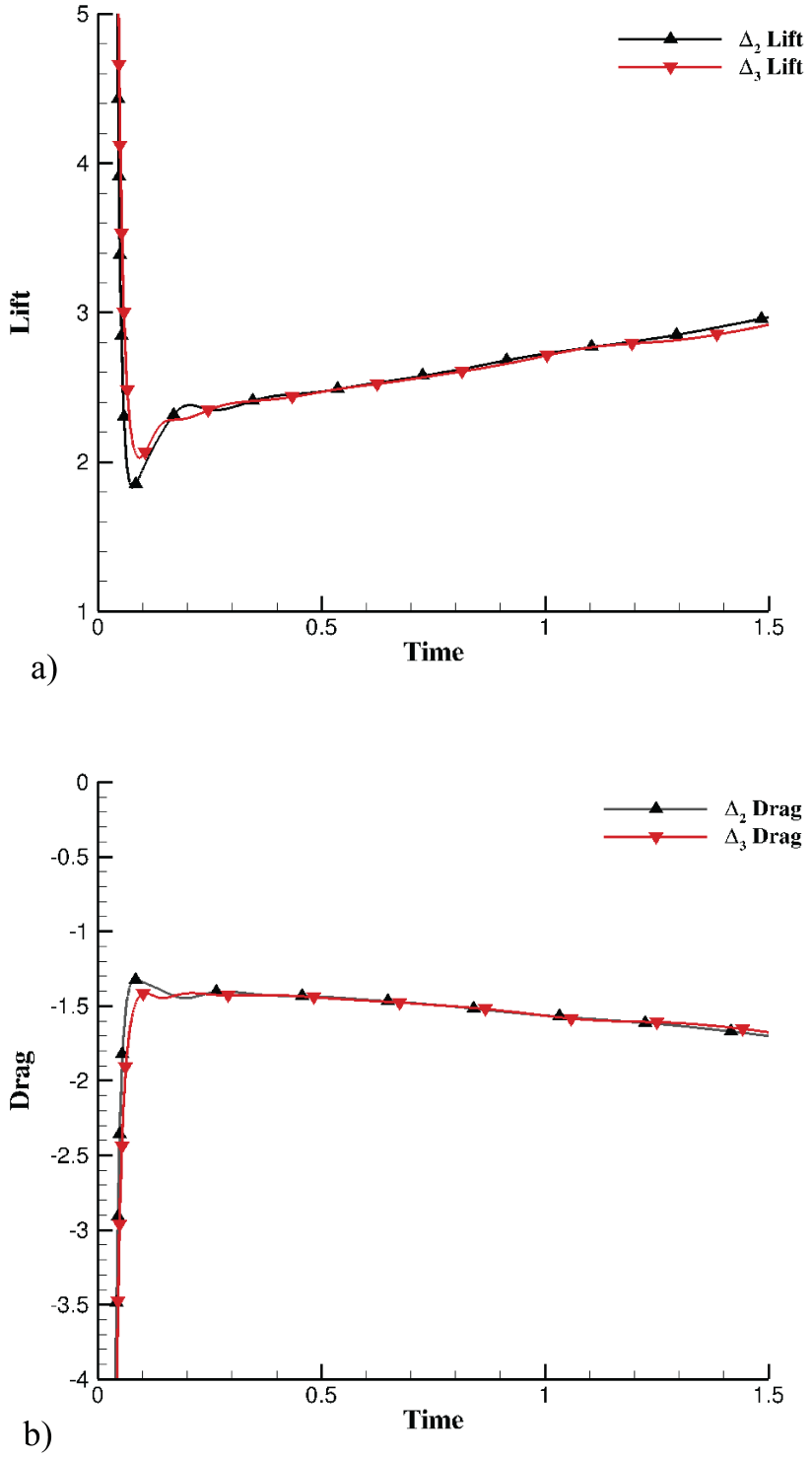

Figure 4.5: *The aerodynamic force histories generated by different grid sizes(black lines: Δ_2; red lines: Δ_3).a) the comparison of the lift, b) the comparison of the drag.*

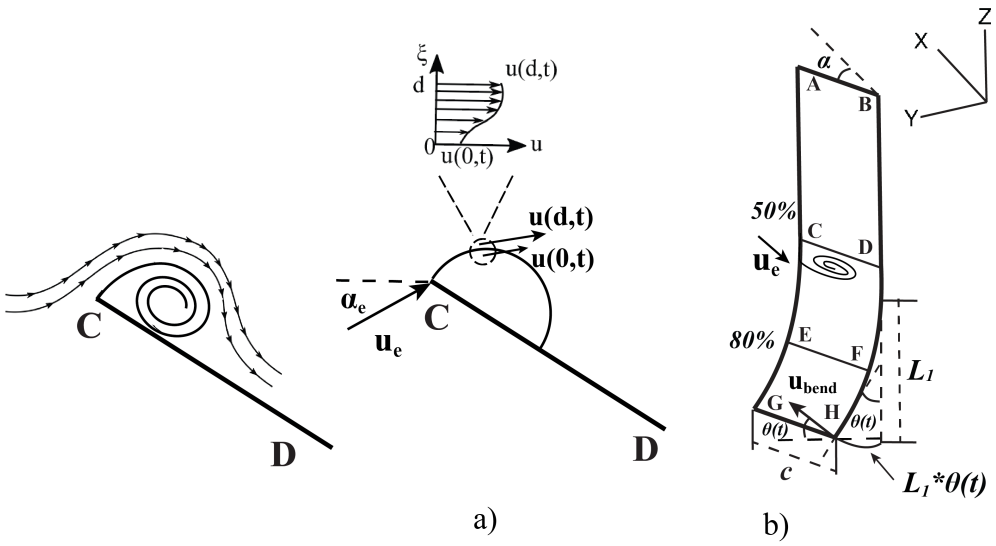

Figure 4.6: *Details of the analytical model: a) The LEV is modeled as a semicylindrical blockage in Wong et al.*[3]*, where vorticity is being supplied by a shear layer; b) the modification implemented in the analytical model in the present work, where the component of the bending velocity was subtracted from the effective velocity on the leading edge*[2]*.*

where u_b is the component of velocity caused by the speeding up of the flow over the semi-circular blockage, u_i is the induced velocity from the vortex itself, and, finally, u_k is the component of the effective leading-edge velocity u_e along the direction of shear layer velocity.

$$u_k = u_e \ sin(\alpha_e); \tag{4.11}$$

To calculate the circulation growth on the part of the wing that is being bent, the component of bending velocity u_{bend} is subtracted from u_k

$$u_{bend} = \frac{L_1 * \theta}{t_{bend}} \tag{4.12}$$

where $\theta = 30°$, $L_1 = 0.35 * \text{span}$, and $t_{bend} = 1$ s in the present case.

The circulation is calculated by

$$\Gamma(t) = \oint u.dl = \pi u(d,t)R(t) \tag{4.13}$$

4.5.2 PIV measure

The flat plate was towed in a fish tank having a length of 1 m and a cross section of 0.45 m × 0.45 m (Fig.4.7). It was fitted with a traverse system (Velmex bi-slide) for towing the models in water. The traversing slide's speed and acceleration were tracked by an ultrasonic motion sensor (PASCO PS-2103A3)[2].

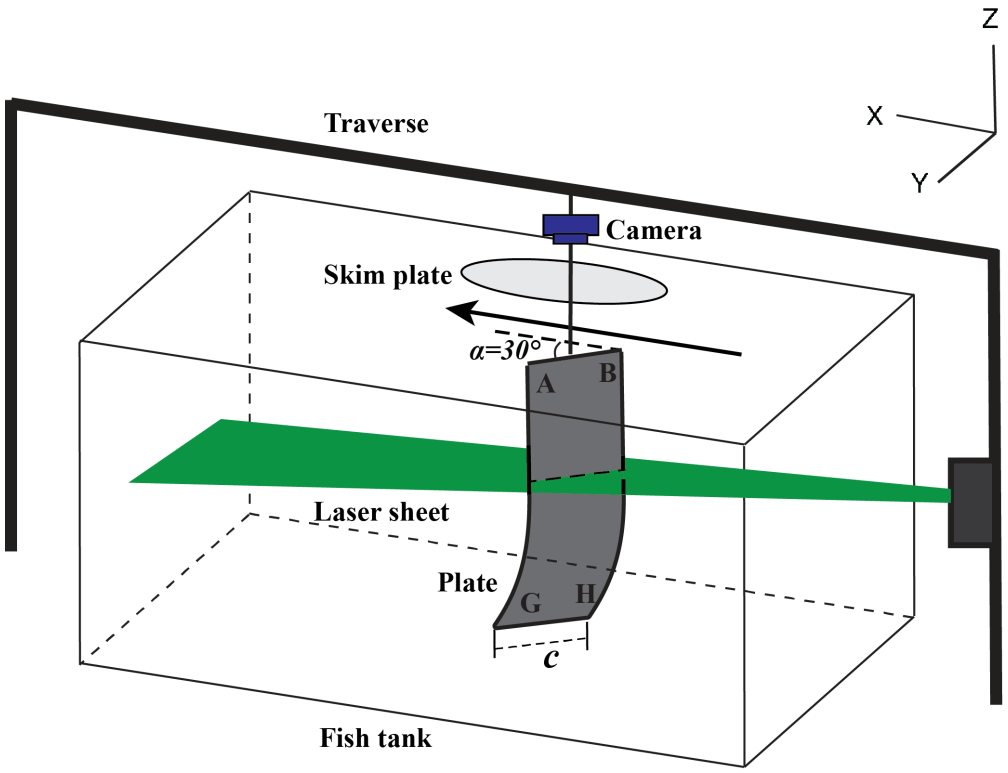

Figure 4.7: *Experimental setup: a 1-m-long towing tank facility equipped with Velmex traverse. The camera travels along with the plate; A skim plate is used to prevent the formation of surface waves during towing. PIV measurements were conducted at 50% and 80% span of the plate (CD and EF in Fig.4.1)[2].*

The growth of the LEV at the plate's midspan location, during the acceleration phase, is shown in Fig.4.8 for both the no-bending and bending cases. These plots show the contours of normalized vorticity —obtained from the PIV experiments —representing the cross section of the LEV at the 50% span of the plate. The cutoff vorticity was selected such that the contours excluded the plate boundary layer, and these cutoffs were maintained the same for the bending and no-bending cases. It is evident that the LEV was not fully developed at the instant the acceleration was completed (denoted by a $t^* = 1$). In the flat (no-bending) case, the LEV continued to grow up to $t^* = 1.9$. The growth of the LEV at the midspan location was very similar when the plate was subjected to dynamic bending in addition to being accelerated from rest. These contour plots show that the bending action did not influence the growth of the LEV substantially at the midspan.

However, quite dissimilar growth of the LEV was observed when I compared the contour plots of normalized vorticity obtained at 80% span from the PIV experiments. Figure 4.9 shows that the development of the LEV was significantly delayed when the plate was bent away from the flow dynamically. It is to be noted that this span location was situated in the flexing part of the plate.

4.5.3 Numerical simulation

Figure 4.10 shows the simulation results presenting the LEV development at the 50% span. At the 50% span, the vortex shapes of the LEV are almost the same for the flat and bending cases at each moment. Hence, DNS also showed that the bending action did not influence the flow in the midspan region of the plate. In the mid-span position, where the effects of

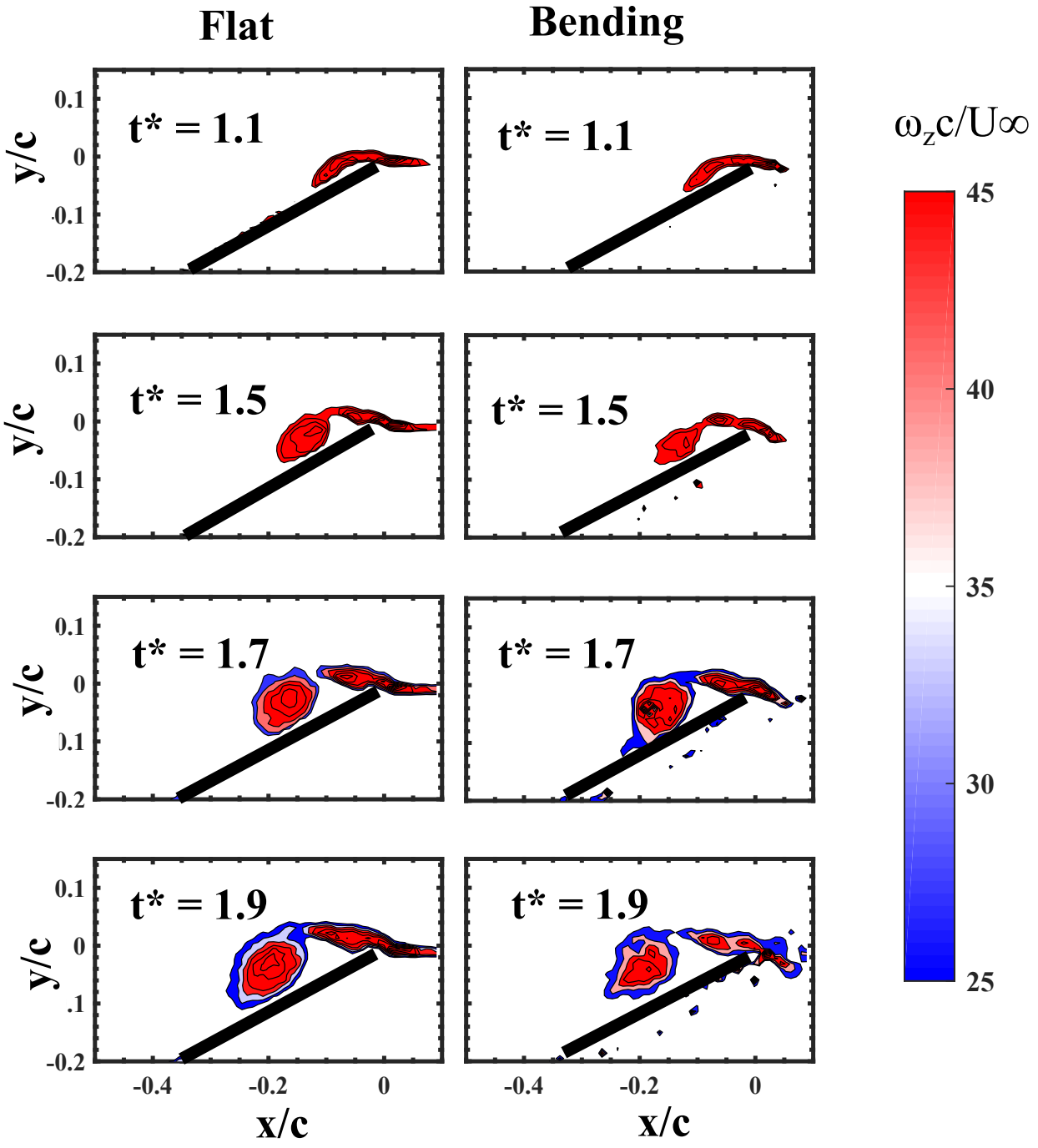

Figure 4.8: *The development of the LEV on the midspan CD (50% span) of the plate from PIV measurements: when no bending was applied (left column) and when bending was applied (right column). The contour plots are created from normalized spanwise vorticity. The cutoffs were selected at each t^* to exclude the boundary layer*[2].

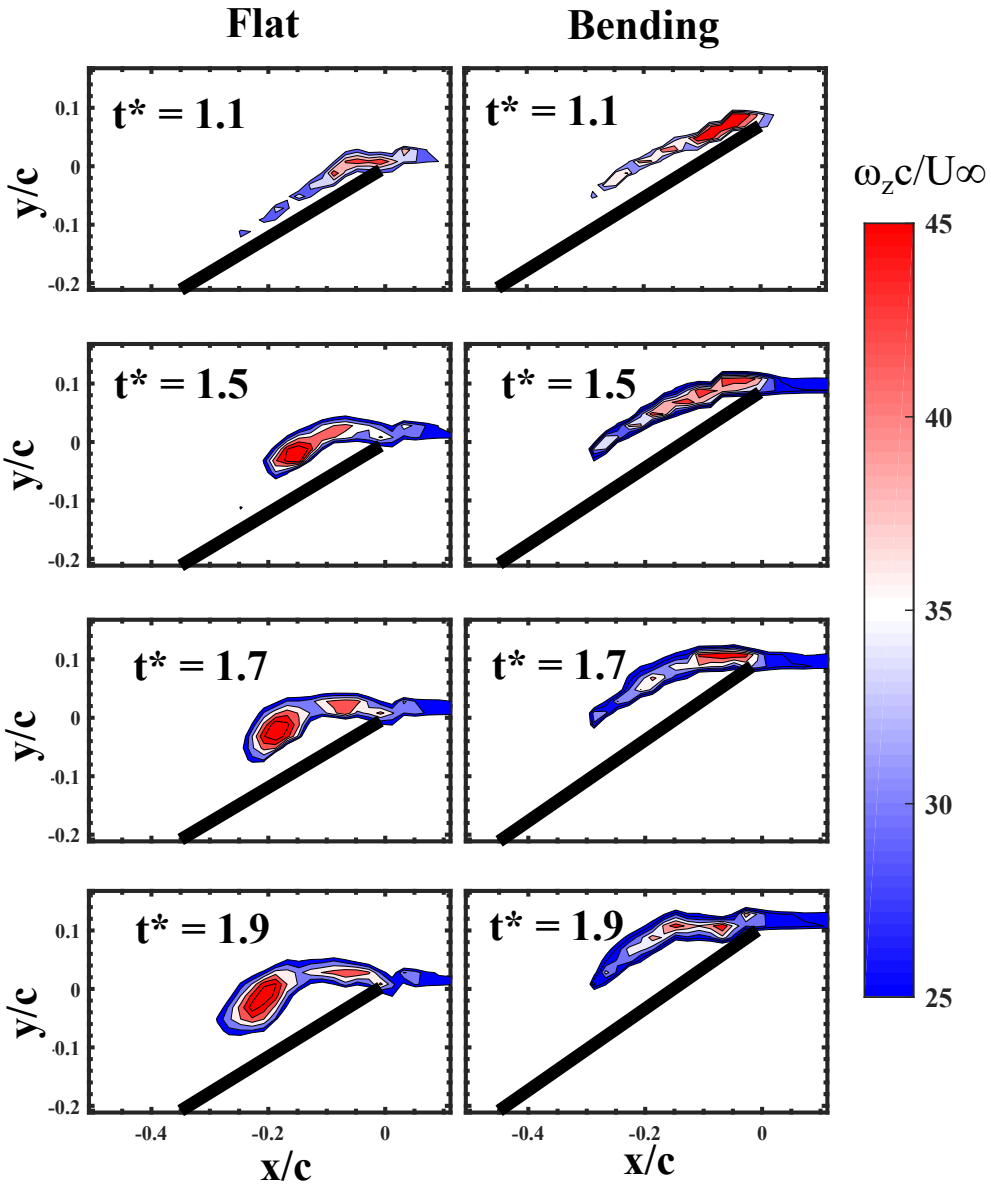

Figure 4.9: *The development of the LEV on EF (80% span) of the plate from PIV measurements: when no bending was applied (left column) and when bending was applied (right column). The contour plots are created from normalized spanwise vorticity. When the plate was dynamically bent, the growth of the LEV at 80% span was delayed[2].*

the vorticity convection are negligible, as shown in Figure 4.13, the vortex shapes of the LEV should be similar, even the same. The details about the vorticity convection will be discussed in the next section.

Figure 4.11 shows the growth of the LEV at the 80% span of the two cases obtained from

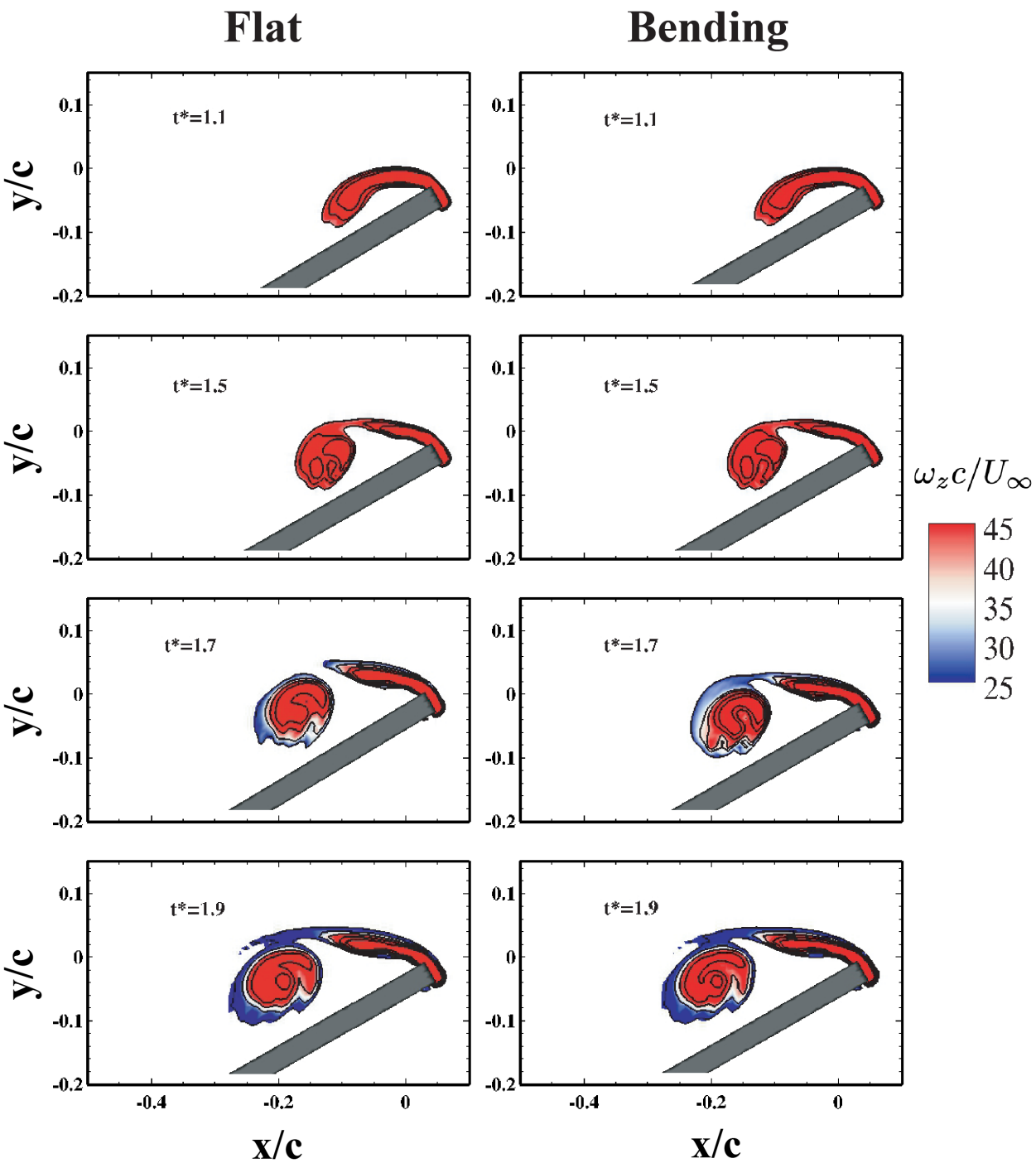

Figure 4.10: *The LEV development on CD (50% span) of the plate from DNS: (left column) when no bending was applied; (right column) when bending was applied*[2].

DNS. Compared to the flat case, the LEV development in the bending case is significantly delayed, especially at $t^* = 1.5$ and 1.7. We note some differences between the DNS results

and the experimental results at the 80% span at $t^* = 1.9$. We ascribe this difference to three-dimensional effects near the tip where the LEV is strongly affected by the tip vortices.

4.5.4 Comparison of LEV circulation

Here, we compared the variation of the non-dimensional circulation of the LEV with t^*, obtained from the analytical model, the experiments, and the direct numerical simulations. At the midspan location, the circulation growth from the analytical model is calculated based on Eqs. (4.13), since this part of the span did not experience any bending. For the bent part, we computed the circulation by adding Eqs. (4.12). For the experimental and numerical data, the circulation inside the LEV was calculated by integrating the vorticity values inside the outermost contours. The vorticity levels were chosen such that they exclude the boundary layer on the plate. Our aim was to characterize the circulation growth only in the LEV. Hence we did not calculate the circulation growth over the whole plate.

Figure 4.12 shows the result of this comparison. We note that the circulation results of the bending and no-bending cases at 50% span matched well between the analytical, experimental, and DNS results. This again corroborates the fact that spanwise bending did not influence the flow at the midspan of the plate. However, the circulation growth computed from simulation and experiment at 80% span for the no-bending case did not match the analytical model. This illustrates that the original analytical model without updating bending velocity does not account for any three-dimensional flow.

When the plate was being bent, we incorporated the bending velocity and updated the

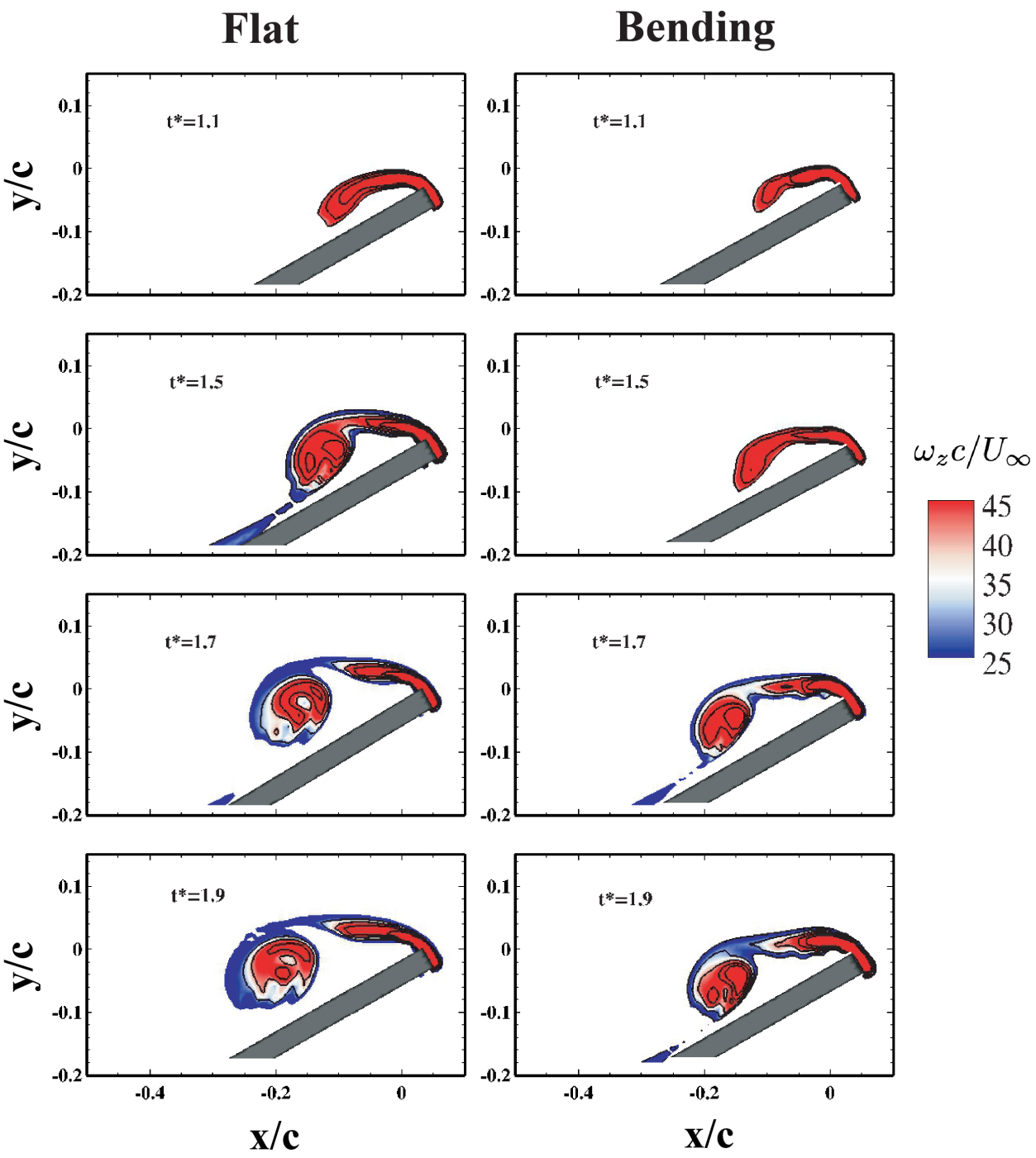

Figure 4.11: *The LEV development on EF (80% span) of the plate from DNS: when no bending was applied (left column) and when bending was applied (right column)*[2].

shear layer velocity to the analytical model. Since our plate is finite span, we expect that the circulation at 80% span of the plate will not be similar to that of the midspan. The circulation

growth in the bent part matched well between the analytical model, the experiments, and the direct numerical simulations. However, we made no attempt to modify the analytical model to account for this finite-span effect, as our focus was the bending part.

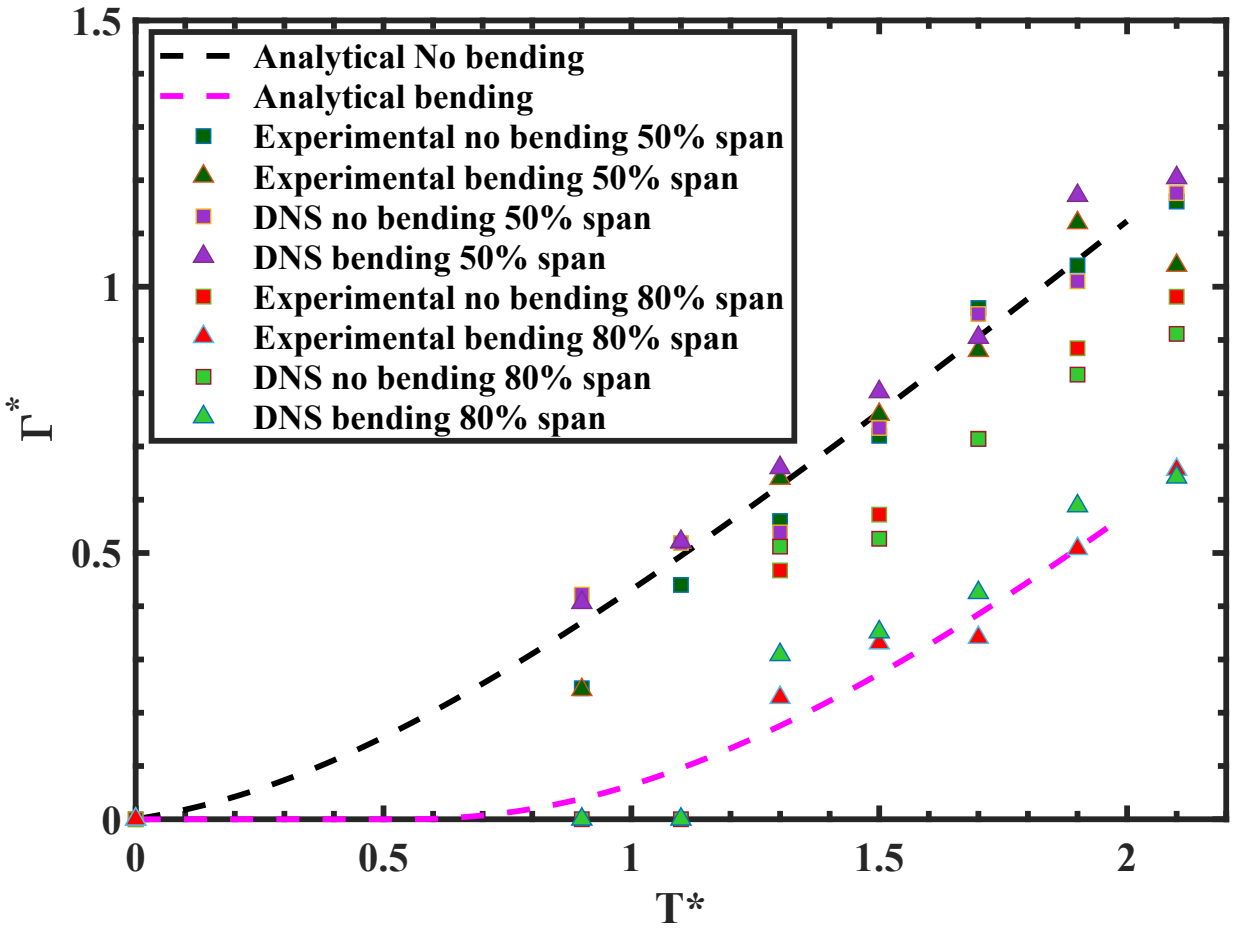

Figure 4.12: *Comparison of the temporal growth of LEV circulation computed from the analytical model, PIV experiment, and DNS study*[2].

When we develop the analytical model, we did not attempt to develop a complicated three-dimensional model, which considers the spanwise vorticity convection. Developing such a model would require detailed treatment of the finite wing effect. A major aspect of the finite wing effect is the consideration of the downwash caused by the tip vortex. The downwash has a significant impact on the development of LEVs near the tip. It would

decrease the effective angle of attack and thus reduce the lift. However, our present analytical model does not make any such attempt to model the downwash, which means the effects on local effective angle of attack are not reflected.

4.6 Effect of bending on the convection of vorticity

This section discusses how the profile bending modifies the vorticity convection inside the LEV by using the DNS data. The comparison of the spanwise vorticity convection flux through the LEV cores of the flat and bending cases in a global view is shown in Fig.4.13 a). At the right tips in the two cases, where the plates are not deformed, the two cases' vorticity convection flux is almost the same: the positive flux (red) and the negative flux (blue) are mixed in a chaotic state. For the flat case, the spanwise distribution of the vorticity convection flux is symmetric about the mid-chord line (50% span). However, for the bending case, the positive vorticity convection flux occupies the entire bent part and plays a dominant role, as shown in Fig.4.13 b). The positive vorticity convection is the primary mechanism that delays the growth of the LEV in the deformed area. In the middle of the plate, the effects of the vorticity convection are negligible for both the flat and the bending cases, which explains the similarity of vorticity contours at 50% span.

The spanwise distribution of vorticity convection changing with time t^* is shown in Fig.4.14. The vorticity convection gets enhanced with time for both cases. For the flat case, the spanwise vorticity convection mostly occurs near the tips and is always mixed. For the bending case, there is always a long and narrow strip of the positive value along the bent part of the plate. These findings conclusively prove that the bending alters the distribution

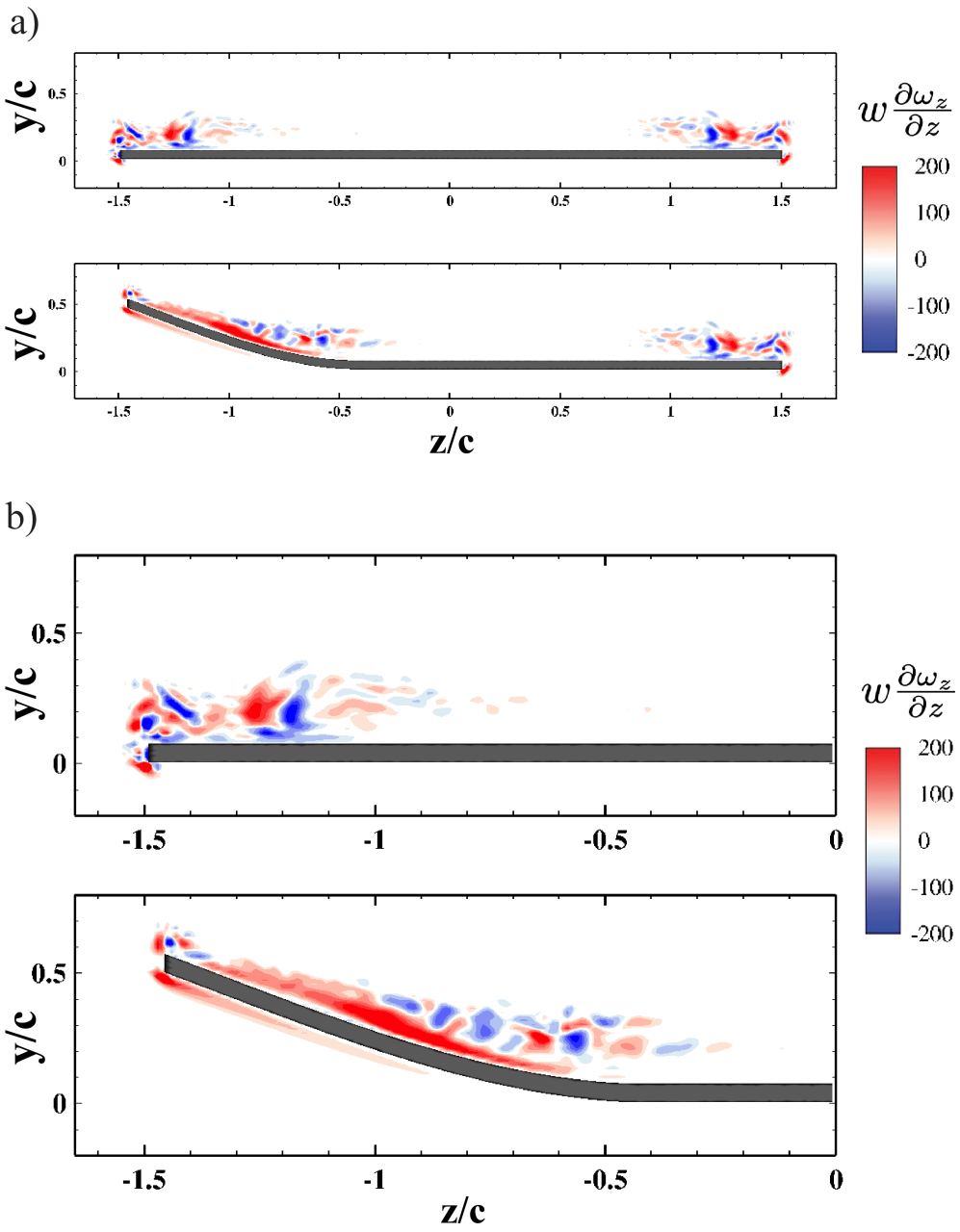

Figure 4.13: *The comparison of the spanwise vorticity convection flux through the LEV cores of the flat and bending cases in a) a global view and b) a zoomed view when* $t^* = 1.9$[2].

of the vorticity convection flux along the span.

Figure 4.15 shows the spatial correlation of the LEV (solid black lines), the secondary vortex (dashed black lines), and the vorticity convection flux (colored lines) at 80% spanwise position when $t^* = 1.5$ and 1.9. For the flat case, when $t^* = 1.5$, the positive vorticity convec-

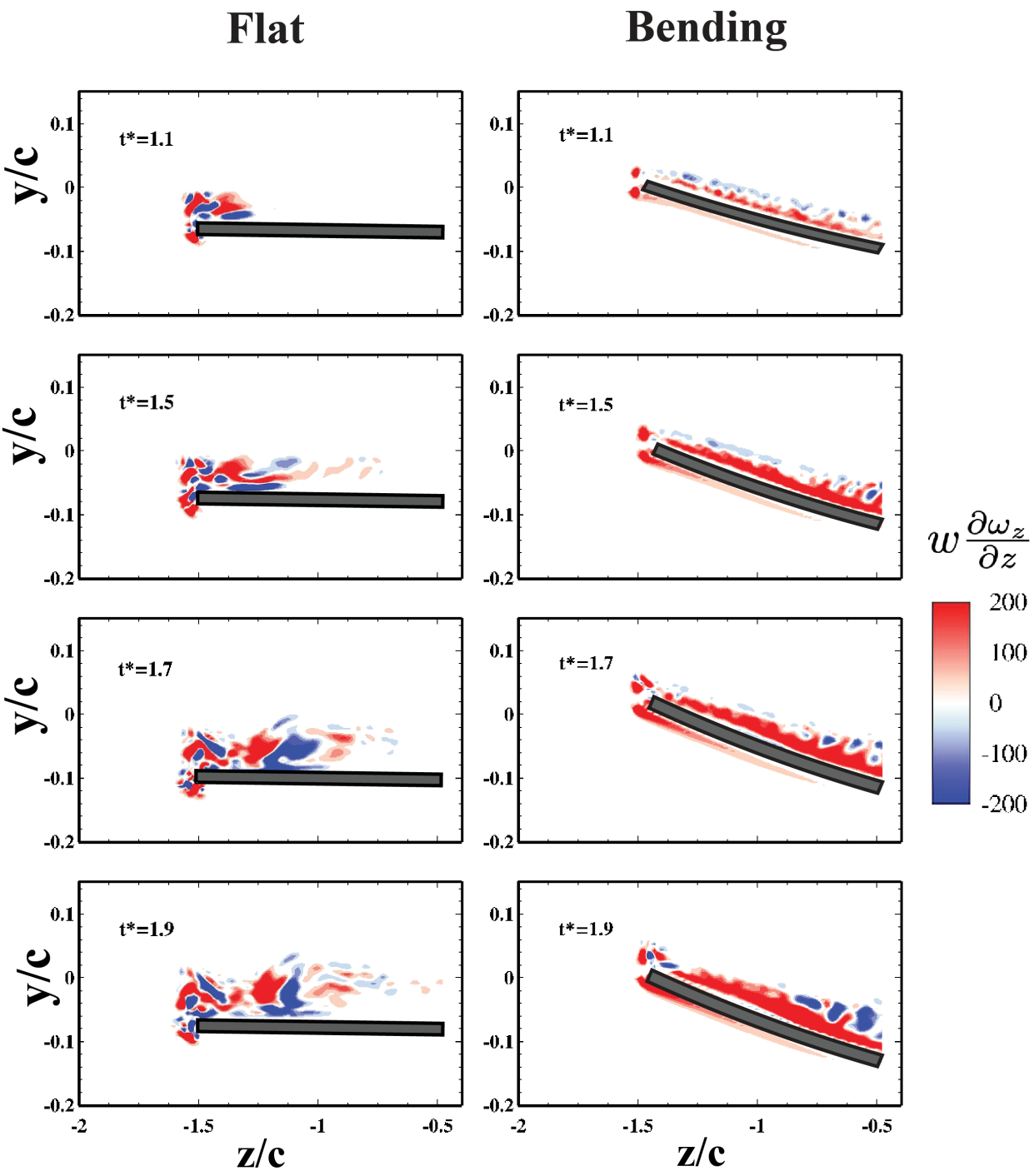

Figure 4.14: *The comparison of the spanwise vorticity convection flux of the flat (left) and bending (right) cases at different moments in a zoomed view from DNS*[2].

tion flux occupies the upper part of the LEV. Meanwhile, the negative vorticity convection flux dominates the secondary vortex and the boundary between vortices. When $t^* = 1.9$, the

secondary vortex rolls up and erodes the connection between the LEV and the leading-edge shear layer, which prompts the LEV to be unstable. For the bending case, when $t^* = 1.5$, the positive vorticity convection dominates the area of the secondary vortex, the boundary between the LEV and the secondary vortex, and part of the LEV. When $t^* = 1.9$, the positive vorticity convection becomes dominating at the secondary vortex, the boundary, and most of the LEV core. Compared with the flat case, the bending suppresses the development of the secondary vortex and delays the growth of the LEV.

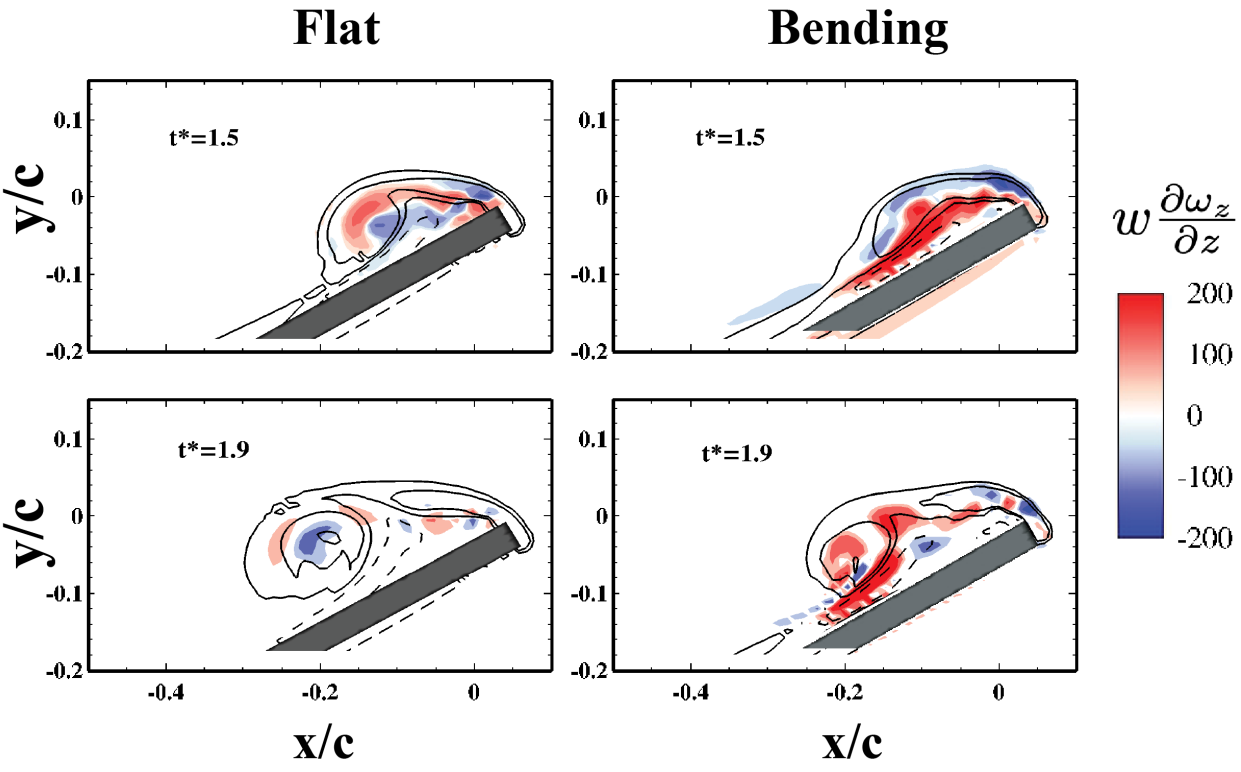

Figure 4.15: *The vorticity contours and the vorticity convection flux at EF (80% span) when $t^* = 1.5$ (top) and $t^* = 1.9$ (bottom). The solid lines and dashed lines represent the LEV and the secondary vortex, respectively. The vorticity convection flux is colored*[2].

4.7 Discussion

The above results show that the bending delays the development of the LEV on a plate whose tip is bending away from the direction of the flow. However, we argue that the main mechanism at play here is the varying shear layer velocity along the leading edge in the bending case. This variation is an outcome of the relative velocity between the plate leading edge and the incoming flow. As the plate's tip moves away from the incoming flow, the shear layer velocity along the leading edge reduces compared to the flat case. Due to this, lesser vorticity is supplied into the LEV and, as a result, its growth gets delayed. This very fact was utilized in the analytical model presented here.

Chapter 5

Conclusions

The adjoint-based approach with the implementation of non-cylindrical calculus for moving boundary problems was developed and validated in the optimization for propulsion of rigid wings. After optimization, the thrust coefficient is improved from 0.29 to 2.39. The increased rolling amplitude a_x and the adjustment of the phase delay φ_z contributed most to the improvement of thrust. And a larger rolling amplitude results in a larger pressure difference between the upper and lower surfaces. The optimal control enhanced the strength of the vortex street and promoted the shed vortex rings to propagate a longer distance.

The modified adjoint-based method is also applied to optimize the active-controlled flexibility (bending and twisting) and explore the aerodynamic potential of flexible wings in terms of thrust and efficiency. The spanwise bending is mimicked by the first natural mode of the Euler-Bernoulli beam. The optimization in spanwise bending on top of a flapping wing in the motion optimized for a rigid wing shows that the bending may double the thrust power at the price of a small reduction of efficiency. The concept of effective rolling angle, which is defined by the instantaneous position of the wing tip, reveals that the spanwise

bending can enhance the amplitude of wing tip motion to improve the thrust in a further step. The effects of wing shape on the thrust are also investigated by adding the second natural mode in the simulation of bending. By modifying the curve of wing shape without changing the motion of the wing tip, the thrust continues to be enhanced.

On the other hand, the optimization of twisting can help the flexible wings maintain a large thrust with a much lower total energy consumption. The efficiency is improved from 0.14 to 0.17. After introducing the twisting, the magnitude of pressure at the wingtip is largely reduced, and the pressure difference is more concentrated on the leading edge. This improvement is explained by the physical model that the effective angle of attack is decreased by the delayed linear twisting. This conclusion is also validated by the optimization for the efficiency of the rigid wing, in which the pitching amplitude is improved to the upper limitation, and the effective angle of attack is reduced. The two cases have the same effective angles of attack and similar pressure distribution on surfaces when $t/T = 0$. These adjoint-based optimizations provide us a unique opportunity to understand the flexibility mechanism with active deformation and optimal guidance to the industrial design.

At last, the effects of bending on the growth of the LEV on a flat plate, which was accelerated from rest to a Reynolds number of 2400, are investigated. As the plate accelerated, a part of its span was bent away from the flow. The numerical simulation showed that the action of bending delays the growth of the LEV, which matches the experimental and analytic results. The DNS results also showed that bending modifies the vorticity convection flux along the plate's bent part, resulting from varying shear layer velocity along the leading edge. The bending action creates a relative velocity between the plate and the incoming flow, which changes the shear layer velocity. Since the formation of the LEV on an accelerating

plate depends on the vorticity-containing mass brought in by the leading-edge shear layer, a reduced shear layer velocity will delay the growth of the LEV. The DNS results also showed that bending reduces the secondary vorticity that plays a crucial role in the pinch-off of the LEV.

Bibliography

[1] Kun Jia and Mingjun Wei. Optimization of flexible flapping wings for thrust and efficiency. In *AIAA AVIATION 2021 Forum*, page 2020, 2021.

[2] Kun Jia, Tyler Scofield, Mingjun Wei, and Samik Bhattacharya. Vorticity transfer in a leading-edge vortex due to controlled spanwise bending. *Physical Review Fluids*, 6(2): 024703, 2021.

[3] Jaime G Wong, Jochen Kriegseis, and David E Rival. An investigation into vortex growth and stabilization for two-dimensional plunging and flapping plates with varying sweep. *Journal of Fluids and Structures*, 43:231–243, 2013.

[4] Thomas A Ward, M Rezadad, Christopher J Fearday, and Rubentheren Viyapuri. A review of biomimetic air vehicle research: 1984-2014. *International Journal of Micro Air Vehicles*, 7(3):375–394, 2015.

[5] AIR FORCE. Broad agency announcement. 1993.

[6] Zaeem Khan, Kyle Steelman, and Sunil Agrawal. Development of insect thorax based flapping mechanism. In *2009 IEEE International Conference on Robotics and Automation*, pages 3651–3656. IEEE, 2009.

[7] Walter Birnbaum. Das ebene problem des schlagenden flügels. *ZAMM-Journal of Applied Mathematics and Mechanics/Zeitschrift für Angewandte Mathematik und Mechanik*, 4(4):277–292, 1924.

[8] Torkel Weis-Fogh. Energetics of hovering flight in hummingbirds and in drosophila. *Journal of Experimental Biology*, 56(1):79–104, 1972.

[9] Fritz-Olaf Lehmann and Simon Pick. The aerodynamic benefit of wing–wing interaction depends on stroke trajectory in flapping insect wings. *Journal of experimental biology*, 210(8):1362–1377, 2007.

[10] Michael H Dickinson, Fritz-Olaf Lehmann, and Sanjay P Sane. Wing rotation and the aerodynamic basis of insect flight. *Science*, 284(5422):1954–1960, 1999.

[11] Wei Shyy, Hikaru Aono, Satish Kumar Chimakurthi, Pat Trizila, C-K Kang, Carlos ES Cesnik, and Hao Liu. Recent progress in flapping wing aerodynamics and aeroelasticity. *Progress in Aerospace Sciences*, 46(7):284–327, 2010.

[12] Charles P Ellington, Coen Van Den Berg, Alexander P Willmott, and Adrian LR Thomas. Leading-edge vortices in insect flight. *Nature*, 384(6610):626–630, 1996.

[13] James M Birch and Michael H Dickinson. The influence of wing–wake interactions on the production of aerodynamic forces in flapping flight. *Journal of experimental biology*, 206(13):2257–2272, 2003.

[14] Charles Porter Ellington. The aerodynamics of hovering insect flight. ii. morphological parameters. *Philosophical Transactions of the Royal Society of London. B, Biological Sciences*, 305(1122):17–40, 1984.

[15] Z Jane Wang. Two dimensional mechanism for insect hovering. *Physical review letters*, 85(10):2216, 2000.

[16] Sanjay P Sane and Michael H Dickinson. The control of flight force by a flapping wing: lift and drag production. *Journal of experimental biology*, 204(15):2607–2626, 2001.

[17] SA Ansari, R Żbikowski, and K Knowles. Non-linear unsteady aerodynamic model for insect-like flapping wings in the hover. part 1: methodology and analysis. *Proceedings of the Institution of Mechanical Engineers, Part G: Journal of Aerospace Engineering*, 220(2):61–83, 2006.

[18] Salman A Ansari, R Żbikowski, and Kevin Knowles. Non-linear unsteady aerodynamic model for insect-like flapping wings in the hover. part 2: implementation and validation. *Proceedings of the Institution of Mechanical Engineers, Part G: Journal of Aerospace Engineering*, 220(3):169–186, 2006.

[19] C-K Kang, Hikaru Aono, Carlos ES Cesnik, and Wei Shyy. Effects of flexibility on the aerodynamic performance of flapping wings. *Journal of fluid mechanics*, 689:32–74, 2011.

[20] Wei Shyy, Hikaru Aono, Chang-kwon Kang, and Hao Liu. *An introduction to flapping wing aerodynamics*, volume 37. Cambridge University Press, 2013.

[21] Robin J Wootton. Support and deformability in insect wings. *Journal of Zoology*, 193 (4):447–468, 1981.

[22] SA Combes and TL Daniel. Flexural stiffness in insect wings ii. spatial distribution and dynamic wing bending. *Journal of Experimental Biology*, 206(17):2989–2997, 2003.

[23] Stacey A Combes and Thomas L Daniel. Into thin air: contributions of aerodynamic and inertial-elastic forces to wing bending in the hawkmoth manduca sexta. *Journal of Experimental Biology*, 206(17):2999–3006, 2003.

[24] Sam Heathcote, Z Wang, and Ismet Gursul. Effect of spanwise flexibility on flapping wing propulsion. *Journal of Fluids and Structures*, 24(2):183–199, 2008.

[25] John Young, Simon M Walker, Richard J Bomphrey, Graham K Taylor, and Adrian LR Thomas. Details of insect wing design and deformation enhance aerodynamic function and flight efficiency. *Science*, 325(5947):1549–1552, 2009.

[26] Gang Du and Mao Sun. Effects of wing deformation on aerodynamic forces in hovering hoverflies. *Journal of Experimental Biology*, 213(13):2273–2283, 2010.

[27] Wei Shyy, Chang-kwon Kang, Pakpong Chirarattananon, Sridhar Ravi, and Hao Liu. Aerodynamics, sensing and control of insect-scale flapping-wing flight. *Proceedings of the*

Royal Society A: Mathematical, Physical and Engineering Sciences, 472(2186):20150712, 2016.

[28] Fang-Bao Tian, John Young, and Joseph CS Lai. Improving power-extraction efficiency of a flapping plate: From passive deformation to active control. *Journal of Fluids and Structures*, 51:384–392, 2014.

[29] João Silva, Jean Sumaili, Ricardo J Bessa, Luís Seca, Manuel A Matos, Vladimiro Miranda, Mathieu Caujolle, Belen Goncer, and Maria Sebastian-Viana. Estimating the active and reactive power flexibility area at the tso-dso interface. *IEEE Transactions on Power Systems*, 33(5):4741–4750, 2018.

[30] Pengfei Liu and Neil Bose. Propulsive performance from oscillating propulsors with spanwise flexibility. *Proceedings of the Royal Society of London. Series A: Mathematical, Physical and Engineering Sciences*, 453(1963):1763–1770, 1997.

[31] CW Pitt Ford and Holger Babinsky. Lift and the leading-edge vortex. *Journal of Fluid Mechanics*, 720:280–313, 2013.

[32] T Maxworthy. The formation and maintenance of a leading-edge vortex during the forward motion of an animal wing. *Journal of Fluid Mechanics*, 587:471–475, 2007.

[33] Jeff D Eldredge and Anya R Jones. Leading-edge vortices: mechanics and modeling. *Annual Review of Fluid Mechanics*, 51:75–104, 2019.

[34] John O Dabiri. Optimal vortex formation as a unifying principle in biological propulsion. *Annual Review of Fluid Mechanics*, 41:17–33, 2009.

[35] David E Rival, Jochen Kriegseis, Pascal Schaub, Alexander Widmann, and Cameron Tropea. Characteristic length scales for vortex detachment on plunging profiles with varying leading-edge geometry. *Experiments in fluids*, 55(1):1660, 2014.

[36] Charles P Ellington, Coen Van Den Berg, Alexander P Willmott, and Adrian LR Thomas. Leading-edge vortices in insect flight. *Nature*, 384(6610):626, 1996.

[37] Jaime G Wong and David E Rival. Determining the relative stability of leading-edge vortices on nominally two-dimensional flapping profiles. *Journal of Fluid Mechanics*, 766:611–625, 2015.

[38] Jaime G Wong and David E Rival. Determining the relative stability of leading-edge vortices on nominally two-dimensional flapping profiles. *Journal of Fluid Mechanics*, 766:611–625, 2015.

[39] Jaime G Wong and David E Rival. Rapid manoeuvring with spanwise-flexible wings. *Journal of Fluids and Structures*, 75:1–8, 2017.

[40] Daochun Li, Shiwei Zhao, Andrea Da Ronch, Jinwu Xiang, Jernej Drofelnik, Yongchao Li, Lu Zhang, Yining Wu, Markus Kintscher, Hans Peter Monner, et al. A review of modelling and analysis of morphing wings. *Progress in Aerospace Sciences*, 100:46–62, 2018.

[41] Markus Kintscher, Johannes Kirn, Stefan Storm, and Fabian Peter. Assessment of the saristu enhanced adaptive droop nose. In *Smart Intelligent Aircraft Structures (SARISTU)*, pages 113–140. Springer, 2016.

[42] Hans Monner, Markus Kintscher, Thomas Lorkowski, and Stefan Storm. Design of a smart droop nose as leading edge high lift system for transportation aircrafts. In *50th AIAA/ASME/ASCE/AHS/ASC Structures, Structural Dynamics, and Materials Conference 17th AIAA/ASME/AHS Adaptive Structures Conference 11th AIAA No*, page 2128, 2009.

[43] Hans Peter Monner. Realization of an optimized wing camber by using formvariable flap structures. *Aerospace Science and Technology*, 5(7):445–455, 2001.

[44] Samuel Courchesne, Andrei Popov, and Ruxandra Botez. New aeroelastic studies for a morphing wing. In *48th AIAA Aerospace Sciences Meeting including The New Horizons Forum and Aerospace Exposition*, page 56, 2010.

[45] Andrei V Popov, Lucian T Grigorie, Ruxandra Botez, Mahmood Mamou, and Youssef Mébarki. Real time morphing wing optimization validation using wind-tunnel tests. *Journal of Aircraft*, 47(4):1346–1355, 2010.

[46] RM Ajaj, MI Friswell, M Bourchak, and W Harasani. Span morphing using the gnatspar wing. *Aerospace Science and Technology*, 53:38–46, 2016.

[47] A Tarabi, S Ghasemloo, and Mahmoud Mani. Experimental investigation of a variable-span morphing wing model for an unmanned aerial vehicle. *Journal of the Brazilian Society of Mechanical Sciences and Engineering*, 38(7):1833–1841, 2016.

[48] Roelof Vos, Zafer Gürdal, and Mostafa Abdalla. Mechanism for warp-controlled twist of a morphing wing. *Journal of Aircraft*, 47(2):450–457, 2010.

[49] Hugo Rodrigue, Seunghyun Cho, Min-Woo Han, Binayak Bhandari, Jae-Eul Shim, and Sung-Hoon Ahn. Effect of twist morphing wing segment on aerodynamic performance of uav. *Journal of Mechanical Science and Technology*, 30(1):229–236, 2016.

[50] Wolfram Raither, Matthias Heymanns, Andrea Bergamini, and Paolo Ermanni. Morphing wing structure with controllable twist based on adaptive bending–twist coupling. *Smart materials and structures*, 22(6):065017, 2013.

[51] Lucas Laursen. Robot fliers in commando competition. *Nature News: Nature Publishing Group*, 2008.

[52] Lai Bin Xu, Shu Xing Yang, and Bo Mo. Pitching dynamic response of variable sweep wing aircraft. In *Applied Mechanics and Materials*, volume 197, pages 159–163. Trans Tech Publ, 2012.

[53] D Lentink, UK Müller, EJ Stamhuis, R De Kat, W Van Gestel, LLM Veldhuis, Per Henningsson, Anders Hedenström, John J Videler, and Johan L Van Leeuwen. How swifts control their glide performance with morphing wings. *Nature*, 446(7139):1082–1085, 2007.

[54] Nan Ma, Xiaodong Zhou, Guangping He, and Jingjun Yu. Design and analysis of a bat-like active morphing wing mechanism. In *ASME 2016 International Design Engineering Technical Conferences and Computers and Information in Engineering Conference*. American Society of Mechanical Engineers Digital Collection, 2016.

[55] Josh Mills and Rafic Ajaj. Flight dynamics and control using folding wingtips: an experimental study. *Aerospace*, 4(2):19, 2017.

[56] Ivan Wang and Earl H Dowell. Structural dynamics model of multisegmented folding wings: theory and experiment. *Journal of aircraft*, 48(6):2149–2160, 2011.

[57] Martin Jones and Nail K Yamaleev. Adjoint-based shape and kinematics optimization of flapping wing propulsive efficiency. In *43rd AIAA fluid dynamics conference*, page 2472, 2013.

[58] Ali Rıza Yildiz, Necmettin Kaya, Ferruh Ozturk, and Orhan Alankus. Optimal design of vehicle components using topology design and optimisation. *International journal of vehicle design*, 34(4):387–398, 2004.

[59] S Vasista and L Tong. Topology optimisation via the moving iso-surface threshold method: implementation and application. *The Aeronautical Journal*, 118(1201):315–342, 2014.

[60] Zhoujie Lyu and Joaquim RRA Martins. Aerodynamic shape optimization of an adaptive morphing trailing-edge wing. *Journal of Aircraft*, 52(6):1951–1970, 2015.

[61] S Sleesongsom, S Bureerat, and K Tai. Aircraft morphing wing design by using partial topology optimization. *Structural and Multidisciplinary Optimization*, 48(6):1109–1128, 2013.

[62] Ismail H Tuncer and Mustafa Kaya. Optimization of flapping airfoils for maximum thrust and propulsive efficiency. *AIAA journal*, 43(11):2329–2336, 2005.

[63] Bret K Stanford and Philip S Beran. Analytical sensitivity analysis of an unsteady vortex-lattice method for flapping-wing optimization. *Journal of Aircraft*, 47(2):647–662, 2010.

[64] Min Xu and Mingjun Wei. Using adjoint-based optimization to study kinematics and deformation of flapping wings. *Journal of Fluid Mechanics*, 799:56–99, 2016.

[65] Fazil O Sonmez. Shape optimization of 2d structures using simulated annealing. *Computer methods in applied mechanics and engineering*, 196(35-36):3279–3299, 2007.

[66] Kai Zhao and James P Schmiedeler. Using rigid-body mechanism topologies to design shape-changing compliant mechanisms. *Journal of Mechanisms and Robotics*, 8(1), 2016.

[67] Mingjun Wei. *Jet noise control by adjoint-based optimization*. University of Illinois at Urbana-Champaign, 2004.

[68] Min Xu and Mingjun Wei. Using adjoint-based approach to study flapping wings. In *51st AIAA Aerospace Sciences Meeting including the New Horizons Forum and Aerospace Exposition*, page 839, 2013.

[69] Min Xu, Mingjun Wei, Chengyu Li, and Haibo Dong. Adjoint-based optimization for thrust performance of three-dimensional pitching–rolling plate. *AIAA Journal*, pages 1–12, 2018.

[70] Charles S Peskin. Numerical analysis of blood flow in the heart. *Journal of computational physics*, 25(3):220–252, 1977.

[71] Tao Yang, Mingjun Wei, and Hong Zhao. Numerical study of flexible flapping wing propulsion. *AIAA journal*, 48(12):2909–2915, 2010.

[72] Mingjun Wei and Min Xu. A continuous adjoint-based approach for the optimization of wing flapping. In *32nd AIAA Applied Aerodynamics Conference*, page 2048, 2014.

[73] Min Xu, Mingjun Wei, Chengyu Li, and Haibo Dong. Adjoint-based optimization of flapping plates hinged with a trailing-edge flap. *Theoretical and Applied Mechanics Letters*, 5(1):1–4, 2015.

[74] Tao Yang, Mingjun Wei, Kun Jia, and James Chen. A monolithic algorithm for the flow simulation of flexible flapping wings. *International Journal of Micro Air Vehicles*, 11:1756829319846127, 2019.

[75] Miguel Cerrolaza, Sandra Shefelbine, and Diego Garzón-Alvarado. *Numerical methods and advanced simulation in biomechanics and biological processes*. Academic Press, 2017.

[76] Jiyuan Tu, Guan Heng Yeoh, and Chaoqun Liu. *Computational fluid dynamics: a practical approach*. Butterworth-Heinemann, 2018.

[77] Michael JD Powell. A direct search optimization method that models the objective and constraint functions by linear interpolation. In *Advances in optimization and numerical analysis*, pages 51–67. Springer, 1994.

[78] Jung Hee Seo and Rajat Mittal. A sharp-interface immersed boundary method with improved mass conservation and reduced spurious pressure oscillations. *Journal of computational physics*, 230(19):7347–7363, 2011.

[79] Siva Nadarajah and Antony Jameson. A comparison of the continuous and discrete adjoint approach to automatic aerodynamic optimization. In *38th Aerospace Sciences Meeting and Exhibit*, page 667, 2000.

[80] Bartosz Protas and Wenyuan Liao. Adjoint-based optimization of pdes in moving domains. *Journal of Computational Physics*, 227(4):2707–2723, 2008.

[81] Jianming Yang and Elias Balaras. An embedded-boundary formulation for large-eddy simulation of turbulent flows interacting with moving boundaries. *Journal of Computational Physics*, 215(1):12–40, 2006.

[82] Min Xu, Mingjun Wei, Tao Yang, and Thomas Burton. Nonlinear structural response in flexible flapping wings with different density ratio. In *49th AIAA Aerospace Sciences Meeting including the New Horizons Forum and Aerospace Exposition*, page 376, 2011.

[83] George V Lauder, Peter Madden, Ian Hunter, James Tangorra, Naomi Davidson, Laura Proctor, Rajat Mittal, Haibo Dong, and Meliha Bozkurttas. Design and performance of a fish fin-like propulsor for auvs. In *Proceedings of 14th International Symposium on Unmanned Untethered Submersible Technology, Durham, NH*, 2005.

[84] Yunpeng Tu, Junshi Wang, Haizhou Hu, and Haibo Dong. Twist morphing effect on propulsive performance of bio-inspired pitching-rolling plates. In *AIAA Scitech 2020 Forum*, page 2019, 2020.

[85] Bruno A Roccia, Sergio Preidikman, Marcos L Verstraete, and Dean T Mook. Influence of spanwise twisting and bending on lift generation in mav-like flapping wings. *Journal of Aerospace Engineering*, 30(1):04016079, 2017.

Appendix A

The process of calculating the circulation by the analytic model

For purposes of review, the completed process of calculating the circulation by the analytic model is listed here. In the original model, the LEV, represented by a semi-cylindrical region, gradually grows in size due to the mass flow brought in by the shear layer. This shear layer is assumed to be of a fixed thickness d. The outer shear layer velocity $u(d,t)$ is assumed to be the sum of three separate velocity components, namely,

$$u(d,t) = u_b + u_i + u_k \tag{A.1}$$

where u_b is the component of velocity caused by the speeding up of the flow over the semi-circular blockage, u_i is the induced velocity from the vortex itself, and, finally, u_k is the component of the effective leading-edge velocity u_e along the direction of shear layer velocity. The three velocities are computed as

$$u_b = U_\infty\Big(1 + \frac{R^2(t)}{r^2}\Big)sin(\alpha_e); \tag{A.2}$$

$$u_i = \frac{\Gamma(t)}{2\pi r}; \tag{A.3}$$

$$u_k = u_e \ sin(\alpha_e); \tag{A.4}$$

Here, $R(t)$ is the radius of the semi-cylindrical blockage and r is the distance of the outer shear layer from the center of the semi-circle, i.e., $r = R(t) + d$. α_e is the effective angle of attack and $\Gamma(t)$ is the circulation of the LEV. In this formulation, we disregard wake vorticity and the bound vortex of the flat plate itself.

Next, we calculate the mass flow rate into the LEV brought in by the shear layer as

$$\dot{m}(t) = \rho \int_0^{t_1} \Big(\frac{u(0,t) + u(d,t)}{2} \Big) dt \tag{A.5}$$

followed by the calculation of the radius of the vortex as,

$$R(t) = 2\sqrt{\frac{2}{\pi}\frac{\dot{m}(t)}{\rho}} \tag{A.6}$$

The final step is to calculate the circulation as

$$\Gamma(t) = \oint u.dl = \pi u(d,t) R(t) \tag{A.7}$$

To calculate $\Gamma(t)$, we start with an initial $\dot{m}$ at $t = 0$ using Eq. (A.1), where $R(t)$ is assumed to be zero at the first time step. After calculating $\dot{m}$ at $t = 0$, we update $R(t)$ in subsequent time steps using Eq. (A.6) and calculate circulation $\Gamma(t)$, using Eq. (A.7). Equations (A.1) to (A.7) have been taken from Wong et al.[3].

To calculate the circulation growth on the part of the wing that is being bent, at every time step, we modify u_k by subtracting the component of the bending velocity u_{bend} from u_k. Here, we assume a constant bending velocity, given by

$$u_{bend} = \frac{L_1 * \theta}{t_{bend}} \tag{A.8}$$

where $\theta = 30°$, $L_1 = 0.35 * \text{span}$, and $t_{bend} = 1$ s in the present case. Then, at every time

step, we subtract the horizontal component of u_{bend} and write

$$u'_e(t) = u_e(t) - u_{bend} * \cos(\theta(t)) \tag{A.9}$$

Finally, we use this u'_e in Eq. (A.4) to calculate u_k.